TECHNISCHE
UNIVERSITÄT
DARMSTADT

A Contribution on the Transferability of Data-Driven Models for Bearing Fault Diagnosis

vom Fachbereich Maschinenbau
an der Technischen Universität Darmstadt

zur Erlangung des akademischen Grades eines
Doktor-Ingenieurs (Dr.-Ing.)
genehmigte

DISSERTATION

vorgelegt von

Christoph Bienefeld, M.Sc.
aus Erbach (Odenwald)

Erstgutachter: Prof. Dr.-Ing. Eckhard Kirchner
Zweitgutachter: Prof. Dr.-Ing. Uwe Klingauf
Tag der Einreichung: 6. März 2024
Tag der mündlichen Prüfung: 7. Mai 2024

Darmstadt 2024
D17

A Contribution on the Transferability of Data-Driven Models for Bearing Fault Diagnosis

Genehmigte Dissertation von Christoph Bienefeld, M.Sc. aus Erbach (Odenwald)

Erstgutachter: Prof. Dr.-Ing. Eckhard Kirchner
Zweitgutachter: Prof. Dr.-Ing. Uwe Klingauf

Tag der Einreichung: 06.03.2024
Tag der mündlichen Prüfung: 07.05.2024

Technische Universität Darmstadt
Darmstadt 2024 - D17

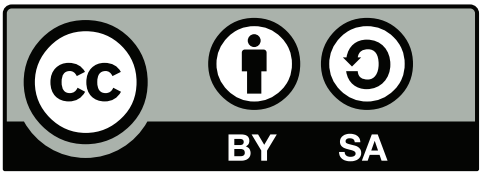

Erklärung

Hiermit erkläre ich, dass ich die vorliegende Arbeit, abgesehen von den in ihr ausdrücklich genannten Hilfen, selbständig verfasst habe. Die "Grundsätze zur Sicherung guter wissenschaftlicher Praxis an der Technischen Universität Darmstadt" und die "Leitlinien zum Umgang mit digitalen Forschungsdaten an der TU Darmstadt" wurden in den jeweils aktuellen Versionen bei der Verfassung der Dissertation beachtet.

Pforzheim, den 6. März 2024

Christoph Bienefeld

Preface

The present thesis was created during my work as a PhD student at Bosch Research in Renningen, in cooperation with the Institute for Product Development and Machine Elements (pmd) at the Technical University of Darmstadt. Even though it is hardly possible to name all the people who supported me on my scientific journey over the past three years, I would nevertheless like to thank a few of them by name.
First of all, I want to take the opportunity to thank my supervising Professor and head of the pmd department, Prof. Dr.-Ing. Eckhard Kirchner, for the scientific guidance of my work. As an external PhD student, I am very happy to have been closely involved in your university department. In addition, I would like to thank Prof. Dr.-Ing. Uwe Klingauf for his interest in my work and for kindly taking on the role of second reviewer. With your expertise and valuable feedback on my research, both of you have helped to sharpen the contents of this thesis.
A big thank you goes to the Robert Bosch GmbH, which enabled my work by financing it. In particular, I want to thank my department head Dr. Martin Giersbeck and my group manager Dr. Alexander Elter for the trust they placed in my work. Furthermore, the many idea-generating discussions together with my two supervisors, Dr. Andreas Vogt and Dr. Marian Kacmar, were essential for shaping this thesis. I am very grateful for your valuable support and the creative freedom you have given me. Additionally, on behalf of the great cooperation with a lot of additional colleagues at Bosch, I would like to express my gratitude to Mr. Jürgen Vdovak, who had a key part in setting up the test bench used and enabling the experimental runs.
I very much enjoyed my time as a PhD student, not least because of the inspiring work with great colleagues both at Bosch and at TU Darmstadt. On behalf of the great PhD community at Bosch, I want to thank Mr. Christian Frie. The solidarity and the occasional moments of amusement have been essential in also getting through the more challenging periods. Likewise, I want to thank the research colleagues at the pmd. The comprehensive feedback from the eTribosystems group and the detailed discussions with Mr. Yanik Koch surely contributed to the quality of this work.
Last but not least, my biggest gratitude goes to my friends and family. In particular, I am deeply grateful for the loving support of my parents Helma and Berthold. The past three years have been challenging and formative for me, both professionally and personally. I truly appreciate the development that this journey has allowed me to achieve and I know that all of this is only possible thanks to your support.

Pforzheim, March 2024

Christoph Bienefeld

Contents

List of Figures

List of Tables

"Rationality is not about knowing facts,
it's about knowing which facts are relevant."

Grant Sanderson

Kurzfassung

In der Automobilindustrie schreitet die Elektrifizierung der Antriebsstränge stetig voran. Zudem steigen vor dem Hintergrund zunehmend automatisierter Fahrfunktionen die Anforderungen an die Sicherheit vor unvorhergesehenen Ausfällen der Fahrzeug-Teilsysteme. Da ein signifikanter Anteil der Ausfälle elektrischer Antriebsmaschinen auf Wälzlagerschäden zurückzuführen ist, sind sowohl die Verhinderung derer Entstehung als auch die frühzeitige Erkennung bereits vorhandener Wälzlagerschäden wichtiger Bestandteil aktueller Forschung. Ein vielversprechender Ansatz, den steigenden Anforderungen zur Ausfallsicherheit gerecht zu werden, ist die Implementierung einer datengestützten Schadensdiagnose. Die Grundlage einer solchen Schadensdiagnose ist die Umsetzung einer Zustandsüberwachung basierend auf mindestens einer geeigneten Messgröße. Besonders verbreitet für die Zustandsüberwachung elektrischer Maschinen ist die Messung von Vibrationen, wozu Beschleunigungssensoren an der Struktur der Maschinen angebracht werden können. Basierend auf den erhobenen Daten ermöglicht die Anwendung von Maschinellem Lernen (ML) eine automatisierte Diagnose von Schäden.
Um Diagnosemodelle auf Basis des überwachten Lernens zu erstellen, werden Trainingsdaten benötigt, welche die zu erkennenden Schäden umfassend repräsentieren müssen. Die Erhebung solcher Daten kann mit erheblichem Aufwand verbunden sein, weshalb datengetriebene Ansätze nach derzeitigem Stand der Forschung nur für einen begrenzten Anteil der Anwendungsfälle wirtschaftlich rentabel sind. Die Rentabilität ließe sich deutlich erhöhen, wenn die mit den Daten eines Maschinentyps trainierten Modelle auf andere Maschinentypen übertragen werden könnten. Hinderlich für diese Übertragbarkeit sind die veränderten Eigenschaften der Sensorsignale beim Wechsel auf einen anderen Maschinentyp. Aus dieser Motivation heraus wird in der vorliegenden Arbeit der Gedanke untersucht, dass die strukturdynamischen Eigenschaften der Maschinen einen entscheidenden Einfluss auf die gemessenen Vibrationen haben können.
Um diesen Einfluss von Unterschieden in der Strukturdynamik auf die Genauigkeit der vibrationsbasierten, datengestützten Schadensdiagnose zu untersuchen, wird zunächst ein Versuchsdatensatz erhoben. Dazu werden künstlich geschädigte Wälzlager in einer elektrischen Maschine verbaut und die Vibrationen in Form der Schwingbeschleunigungen an mehreren Sensorpositionen erfasst. Auf der Grundlage dieses Datensatzes werden verschiedene ML-Algorithmen und Methoden zur Merkmalsgenerierung untersucht, um die Vorhersagegenauigkeit der Diagnosemodelle zu optimieren. Mit den resultierenden Konfigurationen wird die Übertragbarkeit der vibrationsbasierten Schadensdiagnosemodelle auf unterschiedliche Sensorpositionen evaluiert, was die Übertragbarkeit auf ein anderes strukturdynamisches Verhalten repräsentiert. Darauf aufbauend werden in dieser Arbeit zwei neuartige Ansätze vorgestellt, die beide darauf abzielen, die zuvor bewertete Übertragbarkeit der Modelle durch die Einbindung von Domänenwissen aus

der Strukturdynamik zu verbessern. Die mit den neuen Ansätzen erreichten Vorhersagegenauigkeiten zeigen erhebliche Verbesserungen in Bezug auf die Übertragbarkeit. Dementsprechend demonstriert diese Arbeit neuartige Methoden zur Verbesserung der Übertragbarkeit datengetriebener Schadensdiagnosemodelle zwischen verschiedenen Systemen im Hinblick auf sich unterscheidende strukturdynamische Eigenschaften.

Abstract

In the automotive industry, the electrification of powertrains is steadily advancing. Additionally, in the context of increasingly automated driving functions, the requirements for safety against unforeseen failures of the vehicle subsystems are growing. Since a significant proportion of failures of electric machines are caused by rolling bearing faults, both their prevention and the early detection of emerging rolling bearing faults are important aspects of current research. A promising approach to meet the increasing safety requirements is the implementation of data-driven fault diagnosis. The foundation of such fault diagnosis is the application of condition monitoring based on at least one suitable measurement quantity. A particularly common variable for monitoring the condition of electric machines is vibration, which can be measured by mounting accelerometers at the structure of the machine. Based on the acquired data, Machine Learning (ML) methods enable fault diagnosis in an automated manner.
To build models based on supervised learning, training data is required, which has to comprehensively represent the faults to be detected. Collecting this data involves considerable effort, which is why data-driven approaches at the current state of research are only commercially viable for a limited proportion of applications. The profitability would be significantly increased if the models trained using data from one machine type could be transferred to other machine types. Obstacles to this transferability are the changed properties of the sensor signals when switching to a different machine type. Given this motivation, the present thesis examines the idea that the structural dynamic properties, which can vary between different machine types, can have a decisive influence on the measured vibrations.
To investigate the influence of differences in structural dynamics on the accuracy of the vibration-based, data-driven fault diagnosis, an experimental data set is acquired. For this purpose, artificially damaged rolling bearings are installed in an electric machine. During the experiments, the vibration acceleration is measured simultaneously at several sensor positions. Based on the acquired data set, various ML algorithms and feature generation methods are investigated to optimize the prediction accuracy of the fault diagnosis models. Using the resulting configurations, the transferability of the vibration-based fault diagnosis models to different sensor positions is evaluated, which represents the transfer to a different structural dynamic behavior. Based on this, two novel approaches are introduced in the present work, both of which aim to improve the previously assessed transferability of the models by incorporating domain knowledge from structural dynamics. The prediction accuracies achieved with these novel approaches show major improvements in terms of transferability. Accordingly, this work demonstrates novel methods to improve the transferability of data-driven fault diagnosis models between different systems with respect to varying structural dynamic properties.

1. Introduction

Automated monitoring of technical systems is becoming increasingly important due to the growing demand for condition-based maintenance. Compared to conventional maintenance strategies, the condition-based maintenance approach offers advantages in terms of increased system reliability, improved sustainability and overall more economical maintenance [1]. Moreover, automated condition monitoring is becoming increasingly accessible thanks to the widespread availability of modern technologies in the context of Big Data, Artificial Intelligence (AI) and the Internet of Things (IoT). These technologies are redefining how data from different sources can be collected, analyzed, and leveraged to gain valuable insights into the condition of technical systems [2, pp.108-110].
Historically, the discipline of Prognostics and Health Management (PHM) initially focused on safety-critical systems (e.g. aviation) or systems with restricted accessibility for maintenance work (e.g. wind turbines). Nowadays, there is an increasing demand to equip various technical systems with condition monitoring in order to enable modern maintenance strategies. In particular, industries such as energy, manufacturing and transportation are increasingly using condition monitoring technology to optimize their operation [3, pp.5-7].

1.1. Motivation

In the automotive industry, two major trends are currently emerging: The electrification of vehicles and the automation of driving functions. The future of highly and fully automatet driving (SAE level 4 and 5 according to [4]) is leading to an increasing number of fleet vehicles without private owners being responsible for maintenance. Especially concerning fully automated driving and the advent of commercial fleets of Robo-Taxis [5], there is a need to fulfill high requirements for the safety and reliability of the vehicle subsystems [6]. Important approaches to achieve this are the design of redundancy-based, fail-operational systems, or the implementation of intelligent systems to enable predictive diagnosis and control strategies [7]. In electric vehicles, electric machines (e-machines) are one of the main subsystems whose unexpected failures pose a safety risk for vehicle occupants and other road users. Therefore, reliable methods for monitoring the condition of these e-machines and enabling automated fault diagnosis are demanded [8]. Previous studies have shown that, depending on the specific mechanical design and its application, a significant proportion of e-machine failures can be attributed to bearing failures [9]. Within today's e-machines, rolling bearings in particular are commonly used to support the rotor with low friction. Harsh operating conditions such as high loads, extreme temperatures, lubricant contamination or electrical current passage can lead to

fatigue, wear, corrosion, electrical erosion or other modes of bearing failure. These can ultimately result in the failure of the entire drive system and potentially cause accidents or costly repairs. Therefore, early detection of emerging bearing faults is crucial to ensure the safe and reliable operation of electric vehicles [10].
Although there are established standards and guidelines for the design and maintenance of bearings according to their rating life [11], these ratings are based on statistical distributions of fatigue life. They are thus limited in accounting for different types of failure modes or unexpected events [12, p.21]. The current practice for condition monitoring of rotating machinery is often based on measuring vibrations, using acceleration as the primary measurement signal. Vibration analysis has proven effective in detecting specific types of faults at an early stage [13, pp.47-52].
To enable automated monitoring and fault diagnosis of technical systems, the emergence of Machine Learning (ML) methods has opened up new opportunities. ML algorithms can learn from historical data and identify patterns or anomalies that may indicate potential faults or deviations from normal behavior. Based on the acquisition of health-indicative measurement data, a large number of technical systems can be monitored automatically using ML algorithms without the need for human experts to continuously analyze the data [14, pp.4-5]. However, challenges arise regarding the transferability of data-driven ML models from one technical system to another. For vibration- and ML-based fault diagnosis models, the current state of research requires additional health-indicative data to be collected for each system to train the algorithm, which is time-consuming, resource-intensive, and costly. Even the most modern data-driven approaches using Deep Transfer Learning cannot entirely eliminate this need for additional data [14, p.163]. Therefore, it is necessary to develop methods that can be used to generate transferable fault diagnosis models, allowing for cost-effective model deployments across different technical systems.

1.2. Aim of Research

The overarching goal of this research is to advance the generation of transferable, data-driven fault diagnosis models. In particular, the application of rolling bearing fault diagnosis for vehicle e-machines is examined. Therefore, the aim is to develop methods for effectively using vibration measurement data and ML techniques combined with domain knowledge, to create models that can be transferred to different systems without the need for retraining. By achieving this, significant time, resources, and costs associated with the development of new data-driven fault diagnosis models for each new system would be saved.
The present work follows a systematic step-by-step approach to accomplish this aim. Initially, multiple methods for processing vibration signals are investigated, focusing on their effectiveness in generating relevant features for ML-based fault diagnosis. This involves investigations on a variety of mathematical feature formulations. The performance of several feature sets is evaluated using a comprehensive data set of vibration signals acquired from an e-machine test bench. A fault diagnosis model, considered

to be generated according to the current state of research, is then evaluated concerning its transferability within defined boundaries. Based upon this, a key aspect of the present work focuses on developing extended methodological approaches to improve the transferability of ML-based fault diagnosis models by incorporating domain knowledge. These newly proposed approaches are used to generate models based on the e-machine test bench data. Finally, the new approaches are evaluated regarding their models' transferability in comparison to the original baseline approach.
Overall, the present work aims to contribute to the development of transferable fault diagnosis models, specifically focusing on vibration-based fault diagnosis of rolling bearings in the exemplary application of automotive e-machines. To achieve this, the subsequent chapters are structured in the following way: First, chapter 2 outlines the fundamental state of research with a focus on condition monitoring of rolling bearings and data-driven approaches. Building upon this, research gap and research questions are derived in chapter 3. Additionally, the further thesis outline is presented in more detail there. Subsequently, chapter 4 introduces the fundamental methods necessary for the further course of this work. Chapters 5 to 9 focus on the data generation and processing as well as model generation, evaluation and discussion with the aim of answering the formulated Research Questions. Finally, a conclusion is drawn in chapter 10.

2. State of Research

This chapter provides fundamentals on the current state of research for condition monitoring of rolling bearings, focusing on vibration-based and data-driven techniques. Firstly, section 2.1 presents the distinction between different maintenance strategies, motivating the need for condition monitoring. Secondly, section 2.2 introduces into several techniques for condition monitoring of rolling bearings in e-machines. Thirdly, section 2.3 provides an overview on the typical failure modes of rolling bearings as well as their kinematics. Additionally, publicly availiable data sets for bearing fault diagnosis are listed. Fourthly, section 2.4 addresses fundamentals on data-driven approaches for fault diagnosis. Finally, section 2.5 presents approaches from the state-of-research to enhance transferability of data-driven models.

2.1. Maintenance Strategies

The need for reliable condition monitoring and fault diagnosis results from modern maintenance strategies within the discipline of PHM. To explain this need, the present section first presents the common maintenance strategies. Subsequently, the demand for methods that enable automated fault diagnosis is derived.
According to DIN EN 13306, the definition of maintenance comprises the "combination of all technical, administrative and managerial actions during the life cycle of an item intended to retain it in, or restore it to, a state in which it can perform the required function" [15, p.8]. By implementing appropriate maintenance activities, the lifespan of a component can be extended or the time until repair can be prolonged. Effective maintenance can therefore reduce the frequency of necessary maintenance activities and their negative consequences such as downtime, ultimately leading to a reduction in associated costs [16]. There are various categorizations of maintenance strategies. To distinguish between them, the present work refers to the definitions from DIN EN 13306. Accordingly, the main types of maintenance strategies and their interrelationships are illustrated in figure 2.1.

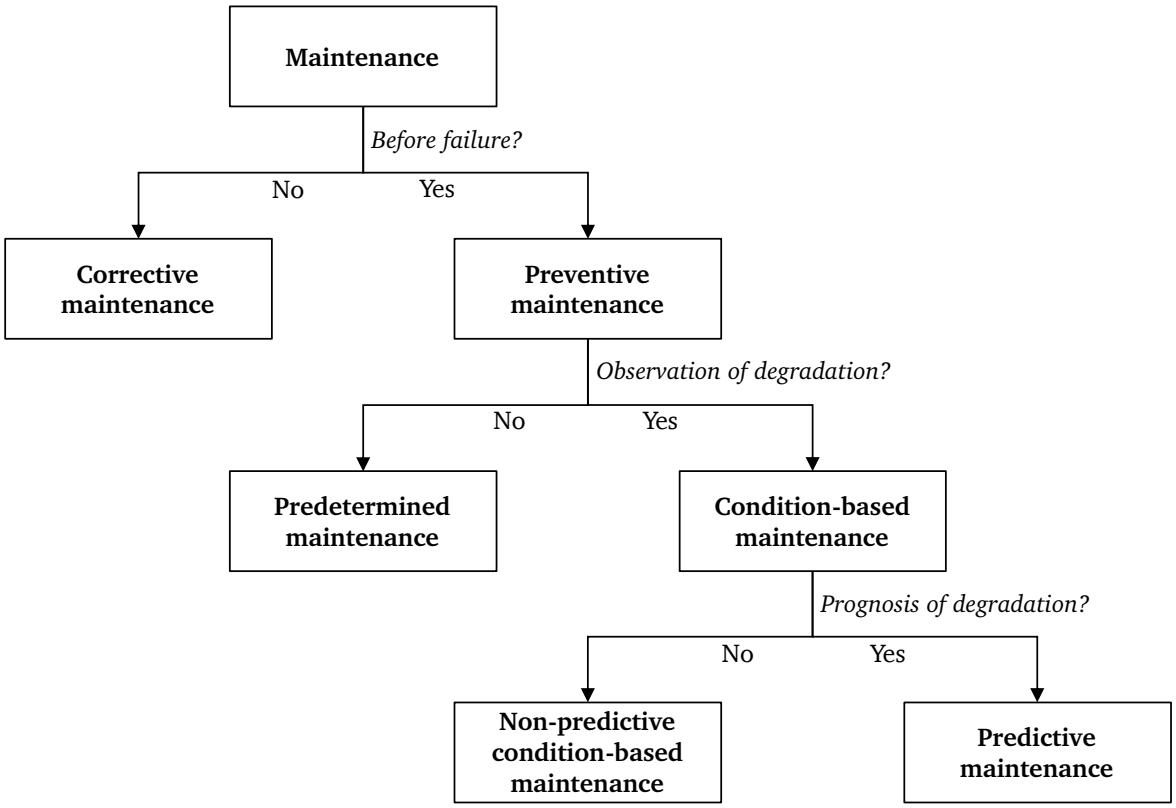

Figure 2.1.: Differentiation of maintenance types; according to [15, p.58].

At the upper distinction level, maintenance can be divided into corrective and preventive maintenance. Here, corrective maintenance is a strategy where maintenance actions are only taken after a component fails or reaches a damage threshold. While initially cost-effective, this strategy leads to high downtime and costs when a failure occurs. Therefore, it is not suitable for critical components and should only be used with redundant systems or readily available resources [17, pp.27-28].
In contrast to corrective maintenance, all strategies belonging to the preventive maintenance branch are intended to intervene before a failure occurs. In particular, predetermined maintenance involves repairing or replacing components at set intervals, regardless of their condition. This strategy reduces the risk of equipment failure and allows for planned maintenance actions. However, it can lead to premature component replacement and thus to insufficient sustainability and increased costs. Implementing this strategy is challenging due to varying failure behaviors and expected lifespans of different components [18, p.2].
In comparison to both of the previously outlined strategies, the use of a non-predictive, condition-based maintenance strategy achieves short downtimes by adjusting maintenance intervals based on the observation of degradation. This requires condition monitoring to enable quick detection of deviations from normal behavior. According to the definition in DIN EN 13306, condition monitoring describes activities "performed either manually or automatically, intended to measure at predetermined intervals the char-

acteristics and parameters of the physical actual state of an item" [15, p.41]. Within a condition monitoring system, fault diagnosis, which includes "actions taken for fault recognition, fault localization and identification of causes" [15, p.43], allows for cost-effective repair measures and reduced risk of complete systeme failure.
An even more sophisticated version of condition-based maintenance is the predictive maintenance strategy. This strategy aims to detect potential hidden faults and prevent their progression by anticipating future changes in component conditions [15, p.35]. The additional prognosis of the degradation and a Remaining Useful Life (RUL) estimation enable precise planning of maintenance activities. This can in theory provide most sustainable and cost-effective maintenance [17, pp.30-34].
Both types of condition-based maintenance are based on condition monitoring. Accordingly, the effectiveness of these strategies is highly dependent on the reliability and accuracy of condition monitoring and fault predictions. This includes fault diagnosis and, for predictive maintenance, the additional prognosis of future degradation. Thus, there is a need for mature monitoring systems. According to Zonta et al. [19], the approaches for implementing fault predictions can be categorized in the following way:

- Physical model-based: Fault predictions rely on mathematical modeling of the underlying physical mechanisms for fault development.
- Knowledge-based: This is sometimes referred to as a hybrid strategy combining physics-based and data-driven modeling and includes approaches to reduce the complexity of physical models.
- Data-driven: Models are based on statistics or ML algorithms to recognize patterns of fault development based on existing data.

In recent research, data-driven approaches are very commonly implemented to enable fault predictions. Therefore, further information on this topic is presented in section 2.4.

2.2. Condition Monitoring of Rolling Bearings in E-Machines

Rolling bearings are used in a wide variety of technical systems. For the present work, the focus is placed on e-machine applications. For e-machines, the literature data on the proportion of failures caused by bearings varies. For example, Bonnett and Yung [9] state that bearing faults are responsible for at least 51 % of the total failures of induction motors for the petroleum and chemical industries. Another comprehensive study concludes a value of 41 % of the failures being related to bearings, however, including several types of bearings such as sleeve and ball bearings [20]. Thus, the exact proportion of rolling bearing failures depends on the application and the specific design of the e-machine. Nevertheless, it is apparent that bearing faults have a significant impact on the reliability of e-machines.

In the course of implementing condition-based maintenance, it is necessary to monitor the components that are critical to failure. Various methods are available for this purpose, using different types of sensor data. Figure 2.2 shows some of the common monitoring approaches and a qualitative ranking of corresponding preventing times before breakdown of the component.

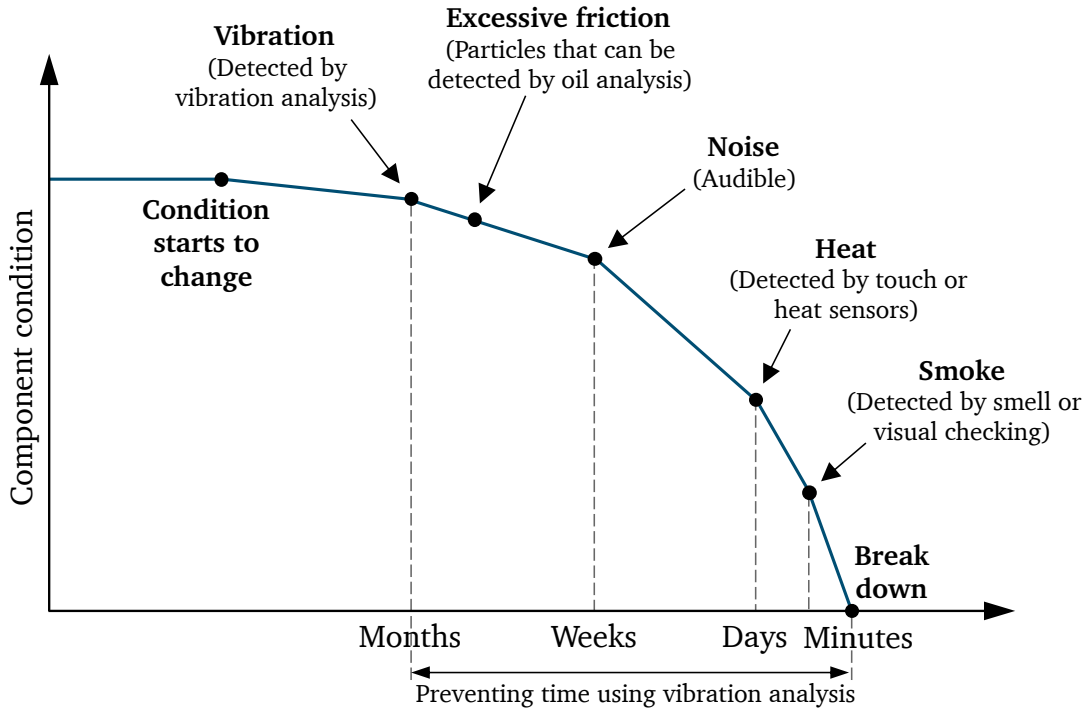

Figure 2.2.: Typical development of a mechanical failure; according to [21].

Furthermore, according to Nandi and Ahmed [3, pp.7-10], the condition of rotating machinery is commonly monitored using the condition monitoring techniques listed below:

- Vibration Monitoring
- Acoustic Emission
- Motor Current Monitoring
- Oil Analysis and Lubrication Monitoring
- Thermography
- Visual Inspection
- Performance Monitoring
- Trend Monitoring

Depending on the machine and its application, a combination of multiple monitoring techniques can be reasonable in order to reach desired prematurity and accuracy of the monitoring system [22]. In the following, the first four of the techniques mentioned above are discussed briefly due to their more common use.
Vibration analysis is the most widely used method for monitoring of rotating components. Changes in the condition, which lead to altered force excitations and consequently to altered vibrations of the systems' mechanical structure, can be detected promptly after the first changes occur [21]. Depending on the operating conditions of the machine and the frequency range to be analyzed, different sensor types and measured variables can be used. The magnitude of the vibration can be quantified in terms of displacements, velocities or accelerations [23]. Most widely, piezoelectric accelerometers are used, which follow the piezoelectric principle. These accelerometers typically can operate in a wide frequency range of up to tens of kHz [3, p.27]. The forces acting on the sensor due to the vibrational movements of the surface cause displacements of electrical charges within the piezoceramic. These charge displacements are measured in terms of voltage signals. A more inexpensive alternative to piezoelectric sensors can be provided by micro-electromechanical systems (MEMS), which are specifically designed to measure acceleration. These MEMS accelerometers are mainly produced lithographically from silicon and its compounds, and can be thought of as microscopically small mass-spring-damper systems. Inside the sensor, narrow silicon patterns form capacitors. When an acceleration is present, the deflection of the microscopical structure causes a change in capacitance, which can be measured [24].
Faults which are characterized by amplitude changes in very high frequency ranges are difficult to detect using vibration analysis. This is where the analysis of Acoustic Emission (AE) offers advantages. The AE technique enables the detection of elastic stress waves inside the material that originate from strain energy which is released during material deformation or crack initiation [25]. By analysing frequencies in the range of around 100 kHz up to 1 MHz, initial events of fault formation can be recognized [26].
As an additional technique for condition monitoring of e-machines and their components, current monitoring is a common choice. Main advantage of this technique is that no additional sensors have to be added to the machine. Instead, readily available measurement quantities in terms of motor current or voltage signals can be utilized [27]. This enables economic benefits in comparison to other monitoring techniques [3, p.8].
Another method of condition monitoring is to analyze the lubricating oil. Oil lubrication is generally designed to be a closed system. Within this system, metal particles that detach from the components are removed from the oil using filters. The number, size and type of particles can be analyzed to draw conclusions about the condition of the components from which the particles originate. Furthermore, parameters such as oil viscosity can be measured in order to determine the lubricant's condition. Oil monitoring can be implemented in a continious way using online systems. However, it is mostly executed offline by regularly taking samples [28]. As rolling bearings inside e-machines are usually lubricated by grease, the oil-based analysis is not feasible there.
In addition to the established techniques described above, within recent research, an additional fault diagnosis technique has been developed which utilizes the measurement of

the bearings' electric impedance [29]. This impedance-based fault diagnosis is expected to provide particularly early preventing times. However, its predictive performance is still to be evaluated in comparison to the more established techniques like vibration monitoring [30].

2.3. Bearing Fault Diagnosis using Vibration Data

From the different techniques for condition monitoring of rolling bearings, presented in the previous section 2.2, the further course of this work focuses on vibration-based fault diagnosis. To introduce the fundamental state of research on this topic, next, a general overview of rolling bearing failure modes is provided in section 2.3.1. Furthermore, the bearing kinematics and fundamental frequencies are presented and visualized in section 2.3.2. Additionally, section 2.3.3 gives an overview on publicly available, scientific data sets which are commonly used for research on bearing fault diagnosis.

2.3.1. Failure Modes of Rolling Bearings

According to DIN EN 13306, a failure mode describes the "manner in which the inability of an item to perform a required function occurs" [15, p.26]. In accordance with ISO 15243, table 2.1 provides an overview of different failure modes occuring in rolling bearings.

Table 2.1.: Overview on rolling bearing failure modes; according to [31, p.3].

Main group	Sub-group
Rolling contact fatigue	Subsurface initiated fatigue Surface initiated fatigue
Wear	Abrasive wear Adhesive wear
Corrosion	Moisture corrosion Frictional corrosion
Electrical erosion	Excessive current erosion Current leakage erosion
Plastic deformation	Overload deformation Indentations from particles
Cracking and fracture	Forced fracture Fatigue fracture Thermal cracking

Starting at the top of table 2.1, rolling contact fatigue is a phenomenon caused by cyclic load of the material [32]. For rolling bearings, these repeated stresses are caused by the

rolling elements passing the raceways. On the one hand, for subsurface initiated fatigue, microcracks begin to develop below the surface. With continued cyclic load, these cracks can propagate to the surface and cause spalling. On the other hand, surface initiated fatigue can be caused by improper lubrication, leading to plastic deformation of the surface asperities and the formation of microcracks [31, pp.3-5].
Wear can be subdivided into abrasive and adhesive wear. In general, it results in the occurence of detached small particles and shape changes of the tribologically stressed surface [33, pp.9-11]. While abrasive wear occurs when a hard surface or particle removes material from a softer counterface, adhesive wear leads to transfer of material by smearing, caused by high contact pressures and temperatures [31, pp.6-8].
Corrosion can be caused by moisture or aggressive media like water or acids and can result in dark discolouration and spalling of material. Additionally, frictional corrosion can occur under certain load conditions, leading to oxidation of the surfaces [31, pp.9-10].
Electrical currents passing through a contact can lead to electrical erosion. This failure mode is particularly relevant for todays rolling bearing applications inside inverter-fed e-machines. According to ISO 15243 [31, pp.12-14], electrical erosion can manifest itself in the form of excessive current erosion or current leakage erosion. Accordingly, the failure can occur in the range from microscopic craters up to dominant, macroscopic fluting on the bearing components. Additionally, the passage of electrical currents can cause lubricant degradation, and lead to the formation of so-called white etching cracks within the material [34].
Plastic deformation takes place as soon as the material's yield strength is exceeded. For example, this can be caused by improper handling, leading to static overload of the bearing. Furthermore, severe damages can occur in terms of cracks or fracture, if the tensile strength of a material is exceeded [31, pp.14-19].
The failure modes mentioned above may initially be caused by design, manufacturing, assembly, operation or maintenance. Within real applications, different failure modes can appear simultaneously or build upon each other. The possible overlap of multiple failure modes can make it difficult to differentiate between them and to analyze their cause [35, pp.1043-1068].
Tribological contacts and the associated modes of possible failures are inherent in many components such as bearings or gearboxes. However, measures can be implemented to reduce the occurrence of failures. For example, reducing the surface pressure by design or improving the kinematics can help to reduce material stress. Furthermore, changes to the tribological system can contribute to the prevention of failures by selecting suitable materials, surface finishes and lubricants [36, pp.206-208].

2.3.2. Bearing Kinematics and Fundamental Frequencies

The bearing kinematic yields fundamental rollover frequencies, which are of great importance for bearing fault diagnosis [37]. If a fault-based surface irregularity exists at one of the raceways or at a rolling element, according to its location, vibrations are excited at so-called fundamental frequencies. These frequencies describe the rate at which a fault passes through the contact areas [13, p.47]. The exact values of the fundamental

frequencies are dependend on the bearing's geometry and its contact angle. Figure 2.3 visualizes the contact angle ϕ and the bearing's pitch diameter d_P as well as its ball diameter d_B.

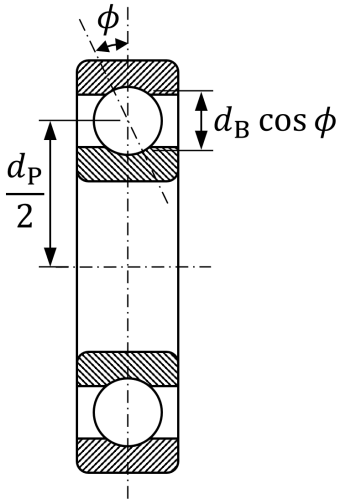

Figure 2.3.: Cross-sectional view of a ball bearing; according to [38, p.169].

On the one hand, the fundamental frequencies depend on the geometrics, including the number of balls (rolling elements) N_B. On the other hand, they depend on the inner ring rotational frequency f_i and the outer ring rotational frequency f_o. Assuming pure rolling within the bearings contacts, the fundamental bearing frequencies can be calculated according to the following formulas [38, pp.167-173]:

- Ball pass frequency, inner race ($BPFI$):

$$BPFI = \left| \frac{N_\mathrm{B}}{2} \left(f_\mathrm{i} - f_\mathrm{o}\right) \left(1 + \frac{d_\mathrm{B} \cos \phi}{d_\mathrm{P}}\right) \right| \tag{2.1}$$

- Ball pass frequency, outer race ($BPFO$):

$$BPFO = \left| \frac{N_\mathrm{B}}{2} \left(f_\mathrm{i} - f_\mathrm{o}\right) \left(1 - \frac{d_\mathrm{B} \cos \phi}{d_\mathrm{P}}\right) \right| \tag{2.2}$$

- Fundamental train (cage) frequency (FTF):

$$FTF = \frac{1}{2} \left[f_\mathrm{i} \left(1 - \frac{d_\mathrm{B} \cos \phi}{d_\mathrm{P}}\right) + f_\mathrm{o} \left(1 + \frac{d_\mathrm{B} \cos \phi}{d_\mathrm{P}}\right) \right] \tag{2.3}$$

- Ball (roller) spin frequency (BSF):

$$BSF = \left| \frac{d_\mathrm{P}}{2 d_\mathrm{B}} \left(f_\mathrm{i} - f_\mathrm{o}\right) \left(1 - \frac{d_\mathrm{B}^2 \cos^2 \phi}{d_\mathrm{P}^2}\right) \right| \tag{2.4}$$

For most use cases, especially in e-machines, the inner ring rotates and the outer ring is fixed. For this case, equations (2.1) to (2.4) can be simplified by setting $f_o = 0$.
Looking at the ball spin frequency BSF for fault diagnosis, the even harmonics are of particular importance, since a ball fault may be in contact on the inner ring and the outer ring for every rotation of the rolling element [39].
To understand vibration-based fault diagnosis, the difference between the fault-induced force excitation and the resulting vibration response at the location of the vibration sensor must be emphasized. For a single, fault-based surface irregularity, and assuming idealized bearing kinematics, the force excitation happens at the rate of the fundamental frequencies outlined in equations (2.1) to (2.4). However, the vibration response results as a combination of the fundamental excitation frequencies and system-dependent, high-frequency resonances. More precisely, the observed vibration corresponds to a modulation of the system's structural resonances with the respective fundamental excitation frequency [13, pp.47-49].
To demodulate this signal in order to extract the fundamental excitation frequencies, a technique called envelope analysis is commonly used, for example, by applying the Hilbert Transform (HT) [39]. Further information on the mathematical foundations of the HT is presented in section 4.3.4. To visualize the vibration behavior of different faults, figure 2.4 shows some idealized vibration patterns and their corresponding envelope signals for single outer race, inner race and rolling element faults. By identifying characteristic vibration patterns and their fundamental frequencies in a vibration measurement, a bearing fault can be diagnosed.

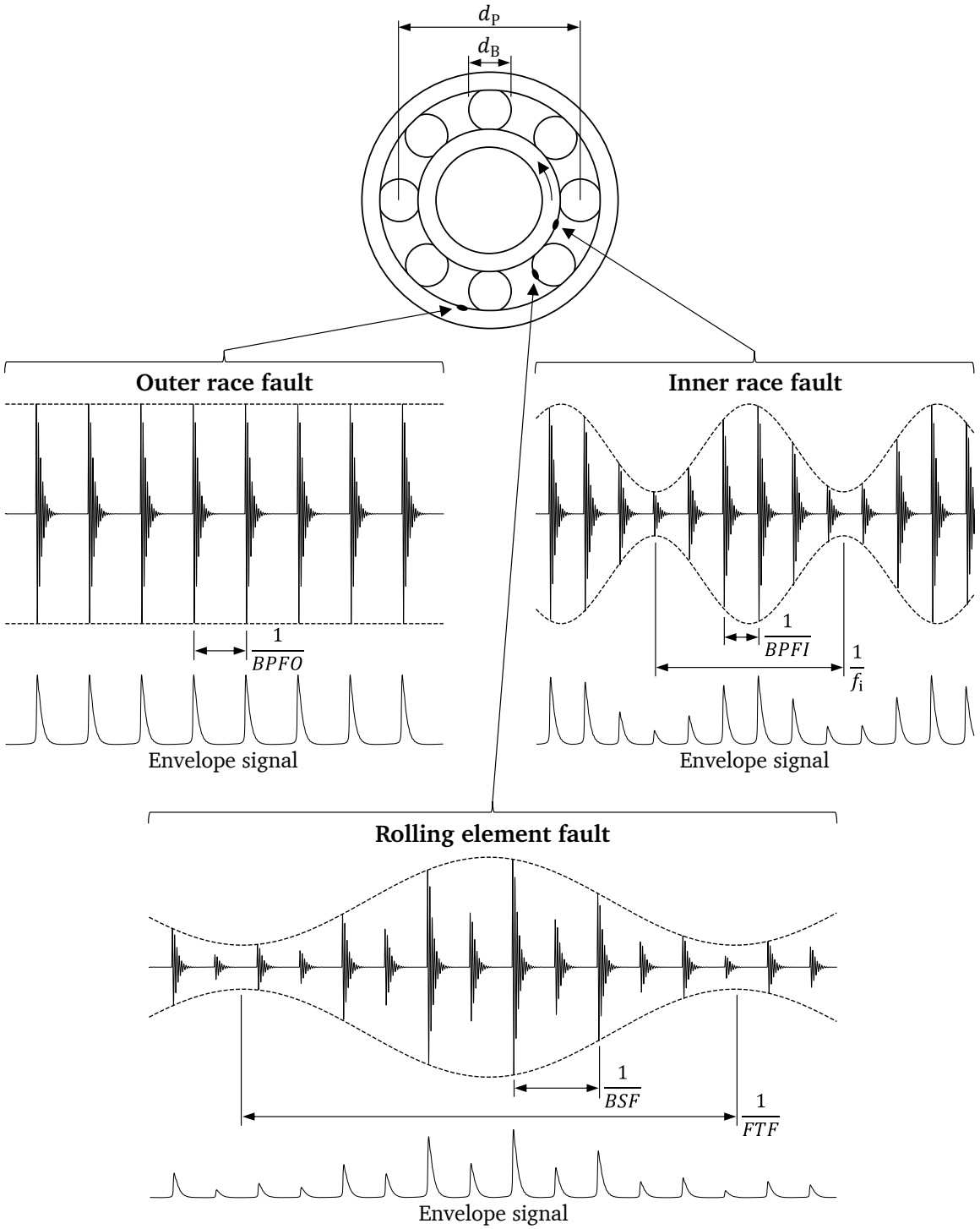

Figure 2.4.: Idealized vibration patterns and corresponding envelope signals of bearing faults; according to [39, p.487].

In addition to the vibration pattern, the amplitude of the vibration can provide information regarding the extend of the bearing fault. To quantify the overall level of a

vibration, a commonly used quantity is the signal's Root Mean Square (RMS) value, since it can provide information about the overall vibrational strength [40]. For information on the mathematical equation to calculate the RMS of a discrete signal, please refer to table 4.2.

2.3.3. Scientific Data Sets

Within past research, data sets were collected at various institutions to develop and verify methods for fault diagnosis of rolling bearings. A majority of these data sets are focused on vibration data. On the one hand, some data sets make use of run-to-failure experiments, in which bearings are operated in endurance tests up to a certain level of damage. On the other hand, several data sets are based on distinct healthy and faulty bearing conditions, prepared prior to the data acquisition test runs. Some institutions provide their acquired data sets to be freely accessible. To provide an overview on these publically available data sets, a selection of them is listed in table 2.2. Systematic reviews on past scientific publications on bearing condition monitoring and fault diagnosis can be found in publications by Schwendemann et al. [41] and Hakim et al. [42]. Both of them summarize a variety of different investigations and the particular data sets used.

Table 2.2.: Overview on widely used, publicly accessible data sets in the context of vibration-based condition monitoring of rolling bearings.

Name	Type of experiments	Number of bearings	Rotational speed in rpm	Sampling rate in kHz
IMS [43]	Run-to-failure	3	2000	20
PRONOSTIA [44]	Run-to-failure	17	1300 to 1800	25.6
XJTU-SY [45]	Run-to-failure	15	2100 to 2400	25.6
CWRU [46]	Healthy and faulty conditions	10	1720 to 1797	12 or 48
MFPT [47]	Healthy and faulty conditions	3	1500	48.8 or 97.6
PU [48]	Healthy and faulty conditions	32	900 or 1500	64

The data sets listed in table 2.2 are now briefly explained. Starting at the top of the table, the IMS (Center for Intelligent Maintenance Systems) data set is also referred to as NASA data set and provides run-to-failure data with experiments running for more than 100 million inner ring revolutions [49]. Similarly, the PRONOSTIA data set, also known as FEMTO data set, provides data from several, accelerated run-to-failure experiments at three different, constant operating conditions [44]. Additionally, the XJTU-SY data

set comprises 5 run-to-failure test runs each for 3 different operating conditions. A primary objective of these three run-to-failure data sets is to enable research on RUL estimation [45].
An extensive data set, frequently used for research on bearing fault diagnosis, is provided by the CWRU (Case Western Reserve University). It comprises data of healthy and faulty bearings at various operating conditions. Therefore, different sizes of seeded faults are given each for inner race, outer race and ball faults [50, 51]. In addition to the CWRU data, both MFPT (Society for Machinery Failure Prevention Technology) and PU (Paderborn University) provide data of healthy and faulty bearing conditions to enable research on fault diagnosis for condition-based maintenance. Therefore, different inner race, outer race, ball and cage faults are used for experimental data acquisition. In particular, the PU data set contains both artificially damaged bearings and bearings damaged using accelerated life tests to produce realistic faults [48]. Later on in the present thesis, a newly collected data set is presented. The characteristics of the measurements for this new data set can be oriented to the publicly available data sets presented above.

2.4. Data-Driven Approaches

Data-driven approaches have gained significant importance in industrial applications, particularly with the emergence of Big Data. By utilizing advanced ML methods, meaningful patterns and trends can be extracted from the data. ML is a subset of AI that enables computers to learn and make predictions or decisions without being explicitly programmed for the specific task. ML methods can interpret large amounts of data by utilizing mathematical algorithms and statistical models. There are various ML algorithms, which can be assigned to the following categories [52, pp.19-23]:

- *Supervised learning* focuses on the utilization of labeled training data, where the algorithm learns to map input data to the desired output.
- *Unsupervised learning* involves training the algorithm on unlabeled data, allowing it to discover hidden patterns or structures within the data.
- *Semi-supervised learning* falls between supervised and unsupervised learning, using some limited amount of labeled data to identify patterns and associate them with additional unlabeled data.
- *Reinforcement learning* is based on the algorithm learning through trial and error, receiving feedback in the form of rewards or penalties to optimize its decision-making process.

For the further course of this work, only supervised learning is considered in more detail. Therefore, figure 2.5 presents a typical workflow when implementing a supervised learning model.

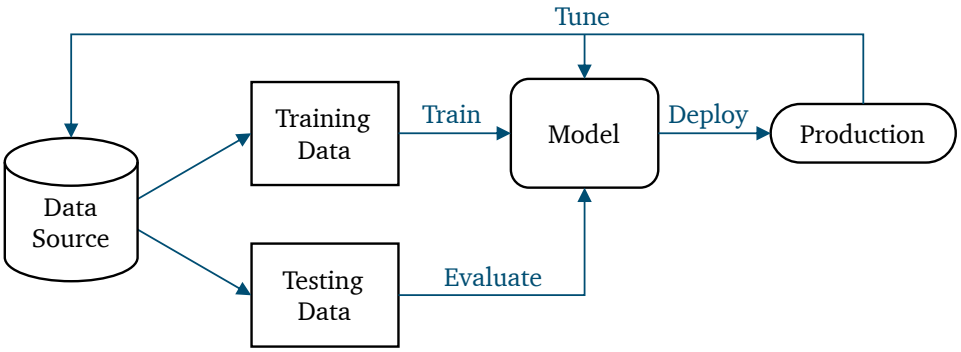

Figure 2.5.: Supervised learning workflow; according to [53].

For supervised learning, labeled data is used to train an ML model. Here, the model is intended to learn the relationships between given input and output values. The input values are referred to as features and the output value is called label. Given a feature space $\mathcal{X}$ and a label space $\mathcal{Y}$, the objektive of the ML algorithm is to learn a mathematical model in terms of an estimation function $\hat{f} : \mathcal{X} \rightarrow \mathcal{Y}$. Given a data sample $S = (\boldsymbol{x}, y) \in (\mathcal{X} \times \mathcal{Y})$, this model shall be able to predict the label y corresponding to the given feature vector $\boldsymbol{x}$. To evaluate the models performance with respect to its prediction of labels, testing data is used. If the model performs satisfactorily, it can be deployed for use with operating data. From the use in production, further data and additional information can be acquired in order to tune the model.
In supervised learning, a distinction can be made between the following two tasks:

- *Classification* for discrete labels.
- *Regression* for continuous labels.

It is important to notice that only the label's type is relevant for deciding whether the current task is a classification (discrete) or a regression (continuous). The features can be discrete, continuous or mixed in both cases [54, p.11].
ML methods require high-quality data and careful model selection to enable reliable predictions. Calculating suitable features and additionally transforming them by using techniques such as the standardization of their distributions can have a significant impact on the prediction quality [55].
For model evaluation, a great variety of different metrics exists. For the reason of compactness, only the so-called accuracy is presented in detail below, as it is a commonly used metric for classification tasks. The accuracy is easy to interpret and particularly suitable for the use with balanced data. Here, the term balanced means that each class is represented with an equal number of data samples. As stated in equation (2.5), the accuracy is defined as the fraction of correct classifications among all classifications made [54, p.147].

$$\text{Accuracy} = \frac{\text{correct classifications}}{\text{all classifications}} \tag{2.5}$$

Since the accuracy is not well suited for the evaluation of imbalanced data, a notable alternative metric for classification is the so-called F-score. In contrast to the accuracy, the F-score can account for differing proportions of individual classes within the data. For comprehensive information on different metrics and their use cases, the reader is referred to available literature on ML, such as the book provided by KUBAT [56].

2.5. Transferability of Data-Driven Models

As already introduced in section 1.2, the present work is driven by the idea to create a bearing fault diagnosis model which can be transferred to a differing technical system. Thus, labeled training data from a first system (source) shall be used to train a data-driven model, which then is meant to enable accurate fault predictions when testing it on a second system (target). Using ML terminology, these two systems are referred to as domains.
With supervised learning, data-driven models are usually trained on labeled data from one domain, and tested on data from the same domain. However, when trying to transfer a data-driven model to a different domain, this scenario is referred to as domain adaption, which represents a subcategory of transfer learning. Figure 2.6 schematically shows the differences between traditional supervised learning and domain adaption. Here, for traditional supervised learning, training and testing data are taken from the same domain $\mathcal{D}^{\mathrm{A}}$. In contrast, with domain adaptation, the training data comes from a source domain $\mathcal{D}^s$ and the testing data is taken from a target domain $\mathcal{D}^t$ [57, pp.534-539].

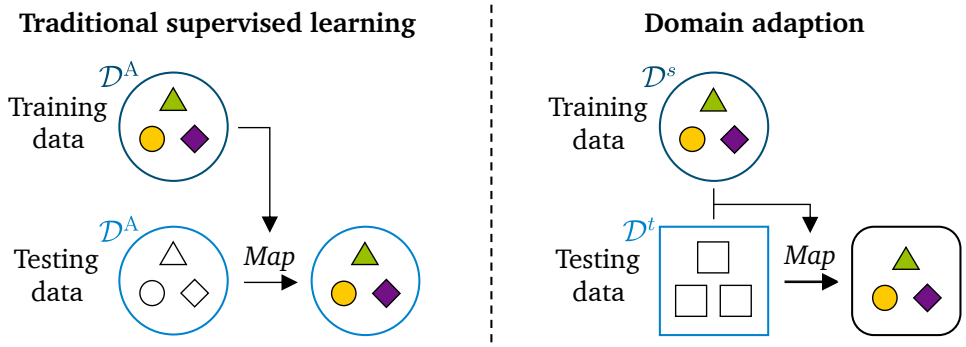

Figure 2.6.: Schematic comparison of traditional supervised learning and domain adaption; according to [58].

The main hurdle to cross with domain adaption is to align the feature distributions in both source and target domains. This is also referred to as domain discrepancy reduction. Let $D = (X, Y) = \{\mathbf{x}_i, y_i\}_{i=1}^{N_{\mathrm{D}}}$ be a labeled data set, consisting of N_{D} data samples and containing the feature set X as well as the corresponding label set Y. Now, $P(X)$ represents the marginal distributions of the feature set X. Due to $\mathcal{D}^s$ being different to $\mathcal{D}^t$, the feature sets of both domains have different marginal distributions $P(X^s) \neq P(X^t)$. To implement domain adaption, a common approach is to search

for a mapping function $\hat{F}(\cdot)$ which enables the mapped, marginal feature distributions $P(\hat{F}(X))$ in both domains to match, so that $P(\hat{F}(X^s)) = P(\hat{F}(X^t))$. However, using data-driven domain discrepancy reduction techniques to create this mapping function requires both labeled samples from $\mathcal{D}^s$ and additional unlabeled samples from $\mathcal{D}^t$, with both of the feature sets X^s and X^t ideally containing samples for the complete label space $\mathcal{Y}^s = \mathcal{Y}^t$ [58, 59].
Thus, for bearing fault diagnosis, the main benefit of the data-driven domain discrepancy reduction techniques is that the samples from the target domain do not necessarily have to be labeled. However, samples should be collected for all bearing faults which are to be detected. Due to this reason, the effort required for data acquisition on the target domain can only be reduced to a limited extent with current, data-driven methods for domain adaptation [27].
To overcome this shortcoming of data-driven domain adaption, a fundamental idea of the present work is to find a domain knowledge-based mapping function $\hat{F}_{\mathrm{dk}}(\cdot)$ to satisfy $P(\hat{F}_{\mathrm{dk}}(X^s)) = P(\hat{F}_{\mathrm{dk}}(X^t))$. In contrast to domain adaption techniques from already available literature, the generation of this mapping function shall not depend on a comprehensive feature set from the target domain $\mathcal{D}^t$. Instead, a transferable model shall be generated using only a labeled data set from the source domain $\mathcal{D}^s$ and additionally incorporated domain knowledge. This is intended to provide advantages in terms of time and cost savings when a fault diagnosis model is to be deployed for a new target system.
Now, having outlined the current state of research, the research design is derived in the next chapter 3.

3. Research Design

The state of research shows that transferability of data-driven models for rolling bearing fault diagnosis is crucial and still a major challenge. Thereby motivated, this chapter specifies the research objectives first. Subsequently, the research hypotheses and Research Questions are derived. Lastly, the further outline of this thesis is presented.

3.1. Research Gap

For the creation of transferable data-driven fault diagnosis models, the main challenge is to avoid changes in the feature distributions inbetween source and target domains [60], see section 2.5. With traditional supervised learning, changes in the feature distributions, which are not correlated to changes of the fault labels, can lead to incorrect predictions. When using vibration measurement data for fault diagnosis, there are some influences which cause exactly such changes of the feature distributions by affecting the measured vibration signals, although the bearing fault remains unchanged. The three main influencing factors on vibration measurement signals for rolling bearing fault diagnosis are presented in figure 3.1.

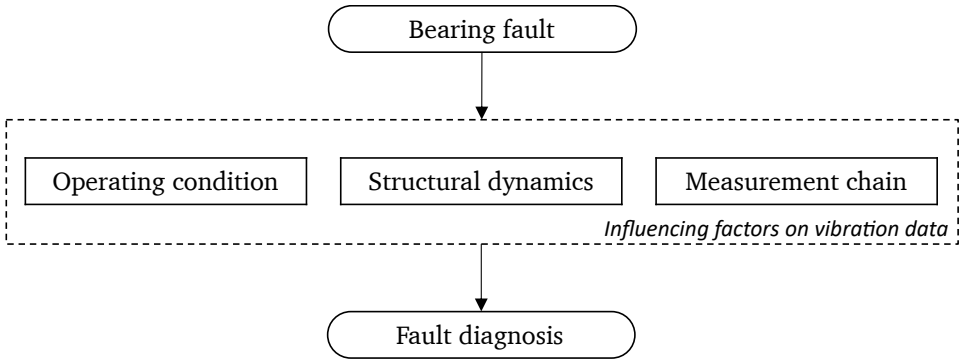

Figure 3.1.: Influencing factors on vibration-based fault diagnosis.

These three main influencing factors are analyzed to different degrees in past literature. Approaches have been made to incorporate some of the influencing factors into data-driven model generation in order to improve the transferability of the resulting models. However, some influences have not yet been taken into account. In the following, the three influencing factors shown in figure 3.1 are elaborated briefly. Building upon this, the research gap is specified.

- Operating conditions: The properties of occurring vibrations depend on the operating condition of the machine. In general, higher system loads lead to greater force excitation amplitudes inside the machine, generating higher levels of vibration. In an analogous manner, a shift in operating speed leads to a shift of the force excitation frequency, also changing the properties of vibration [13, p.47]. Motivated by these influences on the vibration data, data-driven models were already extended in previous research in order to consider the impact of varying operating conditions on the fault predictions [58, 61].
- Structural dynamics: New mechanical systems or new versions of established systems typically differ from the existing ones in terms of their mechanical designs. These changes in mechanical design are accompanied by changes in structural dynamics. Within existing research, the influence of changes in structural dynamics on the vibration-based fault diagnosis has not yet been investigated in isolation. However, the literature indicates that even small changes to a machines structure can have a significant effect on the propagation of structure-borne sound [62].
- Measurement chain: The data acquisition system may vary from one machine to another, leading to different signal properties. This influence can potentially be controlled during product development by selecting data acquisition systems with specific measurement characteristics and adjusted filter settings. Additionally, known measurement characteristics can be used to calibrate the measured data within digital signal processing [63].

As presented above, the influences caused by varying operating conditions or differing measurement chains seem to be manageable according to the state of research. However, there is a research gap regarding the investigation of the influence of differing structural dynamic properties on vibration-based fault diagnosis. In order to create transferable fault diagnosis models, there is a need for novel modeling approaches that can take changes in structural dynamics into account. With this research gap in mind, the Research Questions are derived within the following section.

3.2. Research Questions

The first research objective aims to evaluate the influence of differing structural dynamic properties on the predictive accuracy of data-driven, vibration-based fault diagnosis models. Therefore, the following research hypothesis is stated:

> *Hypothesis: Transferring a data-driven fault diagnosis model for rolling bearings, which is based on vibration measurement data, to a system with differing structural dynamic properties, leads to a reduction of its predictive accuracy.*

The first Research Question aims to test this hypothesis in a quantifying manner by evaluating the predictive accuracy, as defined in equation (2.5):

Research Question 1: To what extent does the transfer of a data-driven, vibration-based fault diagnosis model for rolling bearings to a system with differing structural dynamic properties reduce its predictive accuracy?

The follow-up objective of this work is defined based on the outcome of the first Research Question. Methods are to be developed that enable the generation of models with enhanced transferability to systems with different structural dynamic properties. As introduced in section 2.5, a data-driven solution of this problem would require additional data to be collected on the target system [57]. To avoid this necessity of additional, extensive data acquisition, this thesis focuses on the development of extended models by incorporating domain knowledge of structural dynamics. Therefore, the following hypothesis is proposed:

Hypothesis: Taking domain knowledge into account, extended vibration-based fault diagnosis models can be developed which enable enhanced transferability to systems with differing structural dynamic properties.

Two Research Questions derive from this hypothesis. First, methodological concepts shall be developed for generating extended models that strive to achieve the claims described in the latter hypothesis:

Research Question 2: In which way can domain knowledge on structural dynamics conceptually be utilized to extend vibration-based approaches for bearing fault diagnosis in order to allow for enhanced model transferability to systems with differing structural dynamic properties?

Based on the developed concepts, the evaluation of the extended models follows with regard to their transferability. This evaluation is to be carried out quantifiably within the framework of experimental investigations:

Research Question 3: To what extent do enhanced models, which are created according to the extended approaches from Research Question 2, improve transferability to systems with differing structural dynamic properties in terms of their predictive accuracy?

Summarizing the Research Questions, the present thesis first aims to assess the transferability of vibration-based bearing fault diagnosis to systems with differing structural dynamic properties. Secondly, new approaches are to be derived to enhance transferability by extending these fault diagnosis models using domain knowledge. Thirdly, models are generated using the newly presented approaches and evaluated with respect to the original, state-of-research approaches.

3.3. Thesis Outline

The subsequent chapters of this thesis are structured based on the previously posed Research Questions as underlying guidelines:

- Chapter 4 provides the fundamental methods required for the further course of this work, focusing on the topics of ML, feature generation, signal processing, and structure-borne sound.
- Chapter 5 presents the acquisition of an experimental data set, which is used in the later chapters to answer Research Questions 1 and 3. For this purpose, the experimental design is derived first. Furthermore, the test bench, the preparation of bearing faults, and the procedures required for carrying out the experiments are described.
- Chapter 6 addresses the response to Research Question 1. To assess the acquired data for plausibility, an explorative data analysis is carried out first. Subsequently, various feature engineering methods are investigated and multiple ML algorithms are tuned in terms of hyperparameter optimizations to examine the predictive accuracies of several data-driven models. Initially, the predictive performance of the models is determined on a fixed system without transfer for reference purposes. This is followed by evaluating the transferability of the models using a transfer scenario with differing structural dynamic properties.
- Chapter 7 introduces two novel approaches for generating extended fault diagnosis models. With regard to Research Question 2, both approaches are designed to improve transferability with respect to changes in structural dynamic properties by incorporating domain knowledge.
- Chapter 8 evaluates the approaches developed within the scope of chapter 7 in order to answer Research Question 3. The predictive accuracies are compared to the original vibration-based baseline from chapter 6.
- Chapter 9 discusses the previously determined results with regard to the research questions raised. In addition, the feasibility of the newly proposed approaches is discussed.
- Chapter 10 concludes the contributions of this thesis to the state of research and identifies pending topics for future work.

4. Fundamental Methods

Based on the research questions raised in the previous chapter 3, this chapter now introduces methods which are fundamental for the further course of this work. First, section 4.1 provides a brief overview on the field of ML, focusing specifically on algorithms for classification and the topic of hyperparameter optimization. Furthermore, fundamentals of vibration-based feature generation for ML-based fault diagnosis are presented. On the one hand, extensive lists of statistical features in the time- and frequency-domain are presented in section 4.2. On the other hand, section 4.3 introduces a selection of signal processing methods. Lastly, section 4.4 provides an introduction to the topic of structure-borne sound and its propagation, which is fundamental for a profound understanding of vibration-based fault diagnosis.
The fundamentals presented in the subsequent sections are not intended to cover the entirety of the respective topics, but merely aim to introduce the methods used in the further course of this work. For more comprehensive information on the methods presented here and for further available alternatives, taking a look at the referenced literature is highly recommended.

4.1. Machine Learning Methods

As already introduced in section 2.4, the goal of supervised learning is to approximate an unknown function, which maps a sample of input features to a given label. The further course of this work approaches the task of distinguishing distinct bearing faults. Accordingly, the labels under consideration are of discrete nature. Due to this reason, the introduction of ML algorithms within this section is focused on classification algorithms solely. Subsequent to introducing a selection of classifiers in section 4.1, the topic of hyperparameter optimization is addressed in section 4.1.2.

4.1.1. Algorithms for Classification

For Classification, a wide variety of ML algorithms exists. To provide a brief overview on commonly used classifiers, table 4.1 is considered. Here, the algorithms are assessed with respect to their classification time, training time, and generalization capabilities.

Table 4.1.: Qualitative assessment of ML classifiers; according to [54, p.136].

Algorithm	Classification time	Training time	Generalization
k-Nearest Neighbors	slow	very fast	good for high k
Decision Tree	very fast	fast	very bad
Random Forest	fast	very slow	very good
Discriminant Analysis	fast	slow	good
Artificial Neural Network	fast	slow	good
Support Vector Machine	very fast	very slow	very good

On the one hand, the training time refers to the computational effort necessary to train an algorithm on given, labeled data. On the other hand, the classification time refers to the effort associated with the decision making of an already trained algorithm. For a large proportion of industrial applications, a high amount of computation for training can be afforded, as this only happens initially during the development of an ML-based function. In contrast, the computational effort of an algorithm for the classification on production data is crucial, as it determines the necessary amount of long-term computing resources.
Generalization refers to the ability of an algorithm to correctly apply the learned functional relationship to previously unknown testing data. An important aspect to be mentioned in this context is the so-called overfitting of ML models. Overfitting can be understood as the algorithm's raw memorization of the training data. If the testing data slightly differs from this training data, an overfitted algorithm delivers a significantly decreased performance on the testing data. Generalization refers to the avoidance of overfitting. A well generalizing algorithm therefore produces predictions of approximately equal accuracy for both training and testing data [54, pp.151-154].
The generalization capability of the ML algorithms is of utmost importance for model transferability within a domain adaption scenario. For this reason, the Decision Tree algorithm is discarded due to its bad generalization. Furthermore, the Discriminant Analysis is not considered in further detail, as the Support Vector Machine represents a considerable extension of the Discriminant Analysis [54, p.133].
In accordance with the above mentioned considerations, the four remaining classification algorithms from table 4.1 are elaborated in more detail below. All of these four algorithms allow for good or very good generalization and are capable of approximating non-linear functional relationships. With respect to the explanations below, please keep in mind that not every algorithmic detail is explained here. For full mathematical details, please refer to the cited literature on ML and pattern recognition, such as the textbook written by Bishop [64].

***k*-Nearest Neighbors (*k*-NN)** is an algorithm which uses the similarity between data points to classify new, unlabeled data. Since no real learning is involved despite storing the training data, this type of algorithm is sometimes referred to as "lazy algorithm" [52, p.72]. Figure 4.1 schematically shows how a new testing feature sample, visually represented by the question mark, is assigned to one of two classes by identifying the labels of the nearby training data points. In this example, a two-dimensional feature space is used, represented by the features x_1 and x_2.

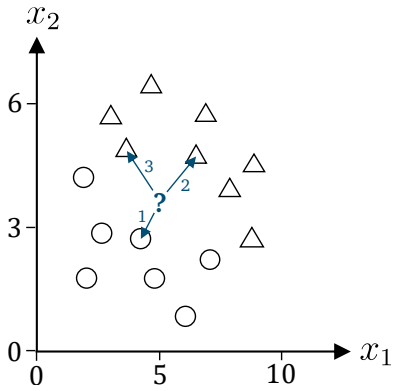

Figure 4.1.: Schematic visualization of the *k*-NN algorithm with $k = 3$.

The number of neighbors, denoted by k, is a hyperparameter of the k-NN algorithm which can be tuned to configure its performance. The choice of a high k-value avoids overfitting and increases the algorithms generalization capabilities. Given the example visualized in figure 4.1, $k = 1$ would lead the new point to be classified as a circle. In contrast, $k = 3$ causes the allocation to the triangle-class due to its majority of the considered nearest neighbors. As visualized, the distance between the data points is decisive for the k-NN classification. Accordingly, the classification result is dependent on the distance measure chosen. A commonly used distance measure is given by the Eucledian distance. In addition to the type of distance measure, feature scaling can have a significant impact on the classification performance. In general, scaling in terms of feature standardization or normalization is recommended to use with the k-NN algorithm. Overall, the k-NN is a very simple classifier with disadvantages in terms of its computational efficiency. However, due to its simplicity, it is well suited as a benchmark in comparison to more complex algorithms [54, pp. 101-103].

Random Forests (RFs) utilize the combination of several Decision Tree (DT) estimators. By combining the predictions of a group of individual ML models, the performance of the overall model can be increased. This approach is called ensemble learning and can be applied to different types of base-learners. Figure 4.2 visualizes the fundamental principle of a RF classifer, which works by predicting the label y_{pred} according to the majority voting of individual DT base-learners. To create an individual DT within the RF, a partition of the original data is used. By making use of the so-called bootstrapping, only some of the features and samples are given to a single DT for training. Based

on this partition of the data, a single DT can be trained by utilizing a chain of simple Boolean decisions [65, p.189].

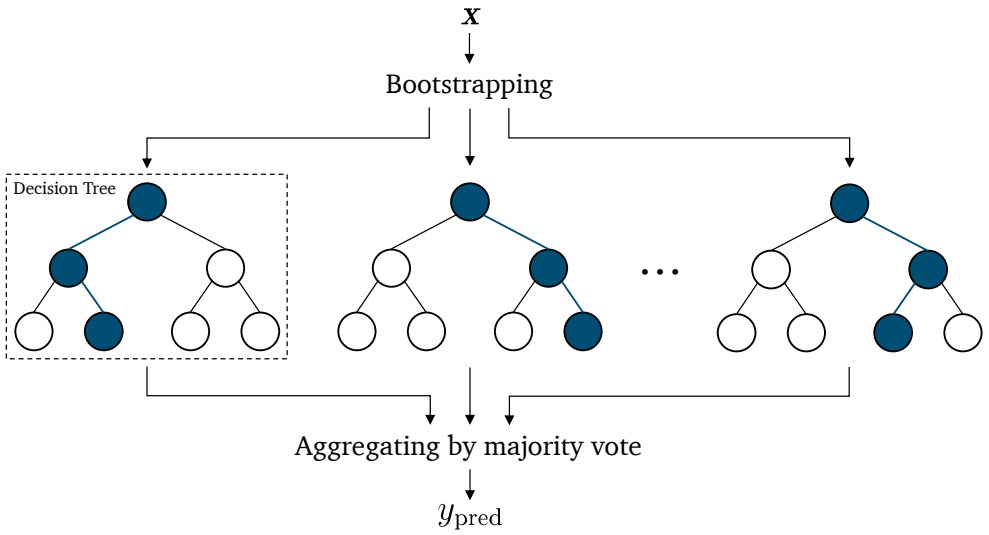

Figure 4.2.: Schematic visualization of DTs voting as part of a RF classifier.

Despite its rather low complexity, the RF is a powerful ML algorithm which provides very good generalization. The performance of the RF can be tuned by several hyperparameters, such as the number of individual DT classifiers, the partition of randomly selected features and the partition of samples used for training of the single DTs. Further hyperparameters can influence the generation of the single DTs, for example by limiting the number of decisions allowed per DT [54, p.107-111].

Artificial Neural Networks (ANNs) are inspired by biological functions found inside the brain or nerve system. An elementary part of the ANN is called a neuron, which can handle multiple inputs to generate an output [52, p.105]. From a mathematical point of view, each artificial neuron makes use of parametrizable weights, an activation function and a bias term. By combining multiple neurons into an ANN, this architecture can be used to approximate functional relationships. Several subtypes of ANNs have been developed in the past decades. Within the present work, only a comparatively simple type of ANN shall be introduced in detail, which is called a feed-forward neural network. It is schematically depicted in figure 4.3 and consists of at least one input and one output layer. Here, each circle visualizes an artificial neuron. To model non-linear functions, at least one hidden layer of neurons has to be incorporated within the ANN [64, pp.225-231].
The number of hidden layers and neurons inside each hidden layer are important hyperparameters to tune when setting up an ANN to be a function approximator. Optimal configurations vary depending on the task's complexity as well as the available amount and quality of training data. If a large number of hidden layers is used, the network is commonly referred to as a Deep Neural Network or simply called Deep Learning (DL). Accordingly, DL can be considered a subgroup of ANNs [54, pp.5-7].

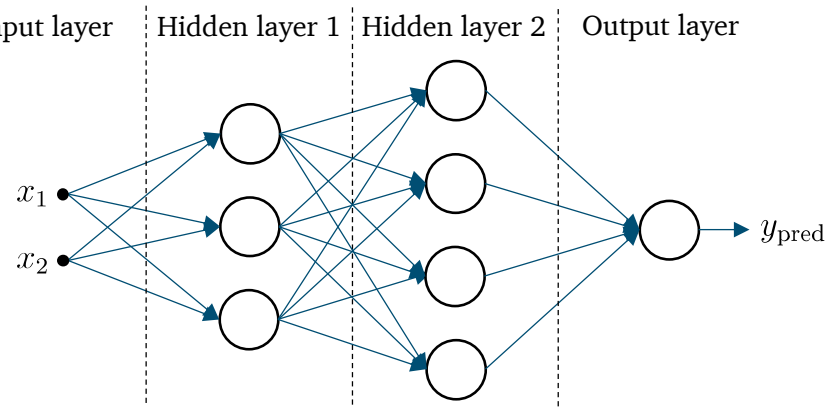

Figure 4.3.: Schematic visualization of a feed-forward ANN with two inputs and one output, using two hidden layers with three and four neurons.

Support Vector Machines (SVMs) make use of so-called hyperplanes to separate the data samples of different classes. A hyperplane is a decision boundary that linearly divides the feature space into two regions. The SVM aims to find the optimal hyperplane, which means to maximize the margin of separation between the hyperplane and the nearest data samples [52, p.58]. Figure 4.4 illustrates this for a two-dimensional feature space in which the hyperplane is given by a dividing straight line.

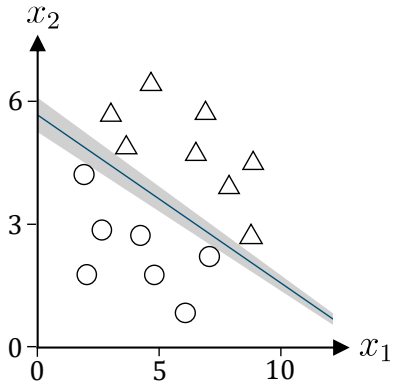

Figure 4.4.: Schematic visualization of a linear SVM separating two classes.

Maximizing the margin between the decision boundary and the data samples usually leads to a very good generalization, which gives the SVM an advantage compared to other classifiers [54, p.134]. In its original form, the SVM is limited to the linear separation of two classes. However, multiclass tasks can also be solved by for example applying the so-called one-versus-the-rest approach in order to use several single hyperplanes in combination [64, p.338]. Additionally, extended versions can also be used to solve non-linear relationships by utilizing so-called kernel functions. The main idea behind the kernel functions is to map the original feature space into a higher dimensional space, where linear separation is possible. The linear separation in this higher dimensional space then corresponds to a non-linear separation in the original feature space. The

specific kernel function to use can be configured via the hyperparameters of the SVM [52, pp.63-66].

4.1.2. Optimization of ML Hyperparameters

ML algorithms contain two categories of parameters. On the one hand, their model parameters are the ones updated and optimized during the training process by fitting the model to the data. On the other hand, the models have hyperparameters which can be used to configure their architectures. This changes the overall behavior of the ML algorithms. In contrast to the model parameters, the hyperparameters are not updated during training process. Instead, they can be tuned to ensure the algorithms optimal performance for the given task and must be set before the final training of the model takes place. Since manual tuning of hyperparameters can be inefficient and lead to suboptimal results, several techniques for automated hyperparameter optimization have been developed. Some examples for these techniques are grid search, random search, evolutionary algorithms or Bayesian optimization [66].
Mathematically, the hyperparameter optimization can be described as follows: Consider given data, comprising a feature set X and a corresponding label set Y. Using this labeled data, an ML model is trained to learn an estimation $\hat{f}(X, \theta)$ of the functional relationship between X and Y. Here, $\theta = (\theta_1, ..., \theta_j)$ is the j-dimensional hyperparameter configuration from the hyperparameter space $\Theta = \Theta_1 \times ... \times \Theta_j$. To assess the performance of the model, a loss function $L(Y, \hat{f}(X, \theta))$ is evaluated. During hyperparameter optimization, this loss is to be minimized with respect to θ in order to get the optimal hyperparameter configuration $\theta^\star$ [67].

$$\theta^\star = \arg\min_{\theta \in \Theta} L(Y, \hat{f}(X, \theta)) \tag{4.1}$$

For the present work, Bayesian Optimization (BO) is utilized for hyperparameter optimization due to its computational efficiency. BO-based methods use previous results to determine the next set of hyperparameters by making use of a surrogate model. The BO procedure can be summarized by the following steps [68]:

- Build a probabilistic surrogate model of the objective function.
- Search for optimal hyperparameter values using the surrogate model.
- Evaluate these hyperparameter values using the real objective function.
- Update the surrogate model using the new evaluation.
- Repeat from second step until termination criterion is reached.

There are multiple types of surrogate models which can be used inside the BO procedure, including Gaussian Processes, Random Forests and Tree-structured Parzen Estimators. For the present work, a Tree-structured Parzen Estimator (TPE) is used inside the BO-based hyperparameter optimization. Main advantages of this BO-TPE optimization

algorithm are its computational efficiency and its capability of handling categorical hyperparameters besides continuous and discrete ones. For full mathematical details on the BO-TPE algorithm, please refer to Bergstra et al. [69].

4.2. Vibration-Based Feature Generation

Feature generation is a process used to derive a useful representation of the original data that is designed to serve as input for the ML algorithm. The generated feature representation is intended to contain the information required for ML-based decision-making in a condensed form. As already stated in the previous chapters, the present work focuses on fault diagnosis by utilizing vibration measurements. To generate features from vibration data, acceleration signals can be processed by using mathematical feature formulas. Feature calculation based on vibration data is commonly categorized into two domains: On the one hand, features can be calculated based on the original time-domain data. On the other hand, the frequency-domain data, usually calculated by applying the Fast Fourier Transform (FFT), can be used for feature calculation. Lei et al. [70, 71] propose a collection of 11 features in the time-domain and 14 features in the frequency-domain. Taking into account the recommendations of Lei et al. and other relevant literature, tables 4.2 and 4.3 provide a collection of frequently used features for application on vibration signals from rotating machinery. This feature collection is already presented within a previous publication of the present author [72]. In the following, table 4.2 presents the formulas of the time-domain features T_i, which are calculated based on the discrete time-domain signal s of length N.

Table 4.2.: Feature formulas in time-domain.

Feature	Formula	
Mean	$T_1 = \frac{1}{N}\sum_{n=0}^{N-1} s(n)$	[70]
Standard deviation	$T_2 = \sqrt{\frac{1}{N-1}\sum_{n=0}^{N-1}\left(s(n)-T_1\right)^2}$	[70]
Square Root Mean (SRM)	$T_3 = \left(\frac{1}{N}\sum_{n=0}^{N-1}\sqrt{\lvert s(n)\rvert}\right)^2$	[70]
Root Mean Square (RMS)	$T_4 = \sqrt{\frac{1}{N}\sum_{n=0}^{N-1} s^2(n)}$	[70]
Maximum absolute	$T_5 = \max(\lvert s\rvert)$	[70]
Skewness	$T_6 = \frac{\sum_{n=0}^{N-1}(s(n)-T_1)^3}{(N-1)\cdot T_2^3}$	[70]
Kurtosis	$T_7 = \frac{\sum_{n=0}^{N-1}(s(n)-T_1)^4}{(N-1)\cdot T_2^4}$	[70]

Crest factor	$T_8 = \frac{T_5}{T_4}$	[70]
Clearance indicator	$T_9 = \frac{T_5}{T_3}$	[70]
Shape indicator	$T_{10} = \frac{T_4}{\frac{1}{N}\sum_{n=0}^{N-1} \lvert s(n) \rvert}$	[70]
Impulse indicator	$T_{11} = \frac{T_5}{\frac{1}{N}\sum_{n=0}^{N-1} \lvert s(n) \rvert}$	[70]
Skewness factor	$T_{12} = \frac{T_6}{T_4^3}$	[73]
Kurtosis factor	$T_{13} = \frac{T_7}{T_4^4}$	[73]
Mean absolute	$T_{14} = \frac{1}{N}\sum_{n=0}^{N-1} \lvert s(n) \rvert$	[74]
Variance	$T_{15} = \frac{1}{N}\sum_{n=0}^{N-1} (s(n) - T_1)^2$	[74]
Peak	$T_{16} = \frac{\max(s) - \min(s)}{2}$	[74]
K factor	$T_{17} = T_{16} \cdot T_4$	[74]
Energy	$T_{18} = \sum_{n=0}^{N-1} s^2(n)$	[75]
Mean absolute deviation	$T_{19} = \frac{1}{N}\sum_{n=0}^{N-1} \lvert s(n) - T_1 \rvert$	[76]
Median	$T_{20} = \text{median}(s(n))$	[76]
Median absolute deviation	$T_{21} = \text{median}(\lvert s(n) - T_{20} \rvert)$	[76]
Rate of zero crossings	$T_{22} = \frac{\text{number of zero crossings}}{N}$	[76]
Product RMS kurtosis	$T_{23} = T_4 \cdot T_7$	[77]
Fifth moment	$T_{24} = \frac{\sum_{n=0}^{N-1}(s(n)-T_1)^5}{T_2^5}$	[78]
Sixth moment	$T_{25} = \frac{\sum_{n=0}^{N-1}(s(n)-T_1)^6}{T_2^6}$	[78]
RMS shape factor	$T_{26} = \frac{T_4}{T_{14}}$	[78]
SRM shape factor	$T_{27} = \frac{T_3}{T_{14}}$	[78]
Latitude factor	$T_{28} = \frac{\max(s)}{T_3}$	[78]

Next, the frequency-domain features are to be introduced. For this purpose, the time-domain signals are transferred into the frequency-domain, using the Fourier Transform (FT). Since discrete signals are processed, a Discrete Fourier Transform (DFT) is used. The specific implementation of the DFT typically uses the FFT algorithm, which enables a particularly computationally efficient calculation of the frequency-domain signal. To reduce so-called spectral leakage, windowing of the time-domain signal has to be performed before applying the DFT calculation. This windowing process is designed to reduce the transients of the discrete, finite signal at its boundaries. For the investigations carried out within this work, the very commonly used Hann window is applied for this purpose [79, pp.187-198]. The discrete Hann window w is calculated according to

$$w(n) = \frac{1}{2}\left[1 - \cos\left(\frac{2\pi n}{N}\right)\right] \tag{4.2}$$

for $n = 0, 1, 2, ..., N-1$.
To achieve correct amplitude scaling in frequency-domain, a amplitude correction factor q_{w} has to be introduced.

$$q_{\mathrm{w}} = \frac{N}{\sum_{n=0}^{N-1} w(n)} \tag{4.3}$$

Now, the DFT-based, scaled, double-sided frequency-domain spectrum S_{ds} can be calculated according to

$$S_{\mathrm{ds}}(m) = \frac{q_{\mathrm{w}}}{N} \sum_{n=0}^{N-1} s(n)w(n) \cdot e^{-\frac{j2\pi mn}{N}} \tag{4.4}$$

with $j = \sqrt{-1}$.
The double-sided spectrum can be converted into the single-sided spectrum S by discarding the negative frequency components and multiplying the amplitudes of the positive frequency components by two. As already mentioned previously, in practice, the FFT is used instead of the original DFT calculation due to computational benefits. For mathematical details on the FFT algorithm, please refer to standard texts on signal processing, such as [80, pp.448-475].
Within the present work, frequency-domain signals are notated using the capital letters of their time-domain representations. Given the discrete, one-sided frequency-domain signal S, its length M and frequencies f, the frequency-domain features F_i can be calculated according to the formulas presented in table 4.3.

Table 4.3.: Feature formulas in frequency-domain.

Feature	Formula	
Mean	$F_1 = \frac{1}{M} \sum_{m=0}^{M-1} S(m)$	[70]
Variance	$F_2 = \frac{1}{M-1} \sum_{m=0}^{M-1} (S(m) - F_1)^2$	[70]
Third moment	$F_3 = \frac{\sum_{m=0}^{M-1} (S(m)-F_1)^3}{M \cdot (\sqrt{F_2})^3}$	[70]
Fourth moment	$F_4 = \frac{\sum_{m=0}^{M-1} (S(m)-F_1)^4}{M \cdot F_2^2}$	[70]
Grand mean	$F_5 = \frac{\sum_{m=0}^{M-1} f(m) \cdot S(m)}{\sum_{m=0}^{M-1} S(m)}$	[70]
Standard deviation 1	$F_6 = \sqrt{\frac{\sum_{m=0}^{M-1} (f(m)-F_5)^2 \cdot S(m)}{M}}$	[70]
C Factor	$F_7 = \sqrt{\frac{\sum_{m=0}^{M-1} f^2(m) \cdot S(m)}{\sum_{m=0}^{M-1} S(m)}}$	[70]
D Factor	$F_8 = \sqrt{\frac{\sum_{m=0}^{M-1} f^4(m) \cdot S(m)}{\sum_{m=0}^{M-1} f^2(m) \cdot S(m)}}$	[70]
E Factor	$F_9 = \frac{\sum_{m=0}^{M-1} f^2(m) \cdot S(m)}{\sqrt{\sum_{m=0}^{M-1} S(m) \sum_{m=0}^{M-1} f^4(m) \cdot S(m)}}$	[70]
G Factor	$F_{10} = \frac{F_6}{F_5}$	[70]
Third moment 1	$F_{11} = \frac{\sum_{m=0}^{M-1} (f(m)-F_5)^3 \cdot S(m)}{M \cdot F_6^3}$	[70]
Fourth moment 1	$F_{12} = \frac{\sum_{m=0}^{M-1} (f(m)-F_5)^4 \cdot S(m)}{M \cdot F_6^4}$	[70]
H Factor	$F_{13} = \frac{\sum_{m=0}^{M-1} \sqrt{f(m)-F_5} \cdot S(m)}{M \cdot \sqrt{F_6}}$	[70]
J Factor	$F_{14} = \sqrt{\frac{\sum_{m=0}^{M-1} (f(m)-F_5)^2 \cdot S(m)}{\sum_{m=0}^{M-1} S(m)}}$	[71]

Thus, a total of 28 time-domain and 14 frequency-domain feature formulas are provided for feature generation within this work.

4.3. Signal Processing Methods

The features presented in the previous section can be applied directly to the raw signal and its frequency-domain representation. However, it is also common to use additional signal processing methods and perform the feature calculation based on such processed signals [71, pp.60-65]. A great variety of different techniques for signal processing exists in literature. To limit the scope of this work, only a few important methods are to be

presented here. These methods are selected with reference to a previous publication by the present author [72] with respect to the predictive performances obtained there. Therefore, firstly the frequency band separation is introduced as a processing method for feature generation. Furthermore, the mathematical operation of convolution is explained briefly. Subsequently, the Wavelet Transform and the Hilbert Transform are presented, which are of importance for the further course of this work.

4.3.1. Frequency Band Separation

Within previous publications, the present author demonstrated the benefit of splitting the frequency-domain data into separate frequency bands before applying the frequency-domain feature formulas. This split is visualized in figure 4.5, showing equally sized frequency band separation with an exemplary number of frequency bands $N_{\mathrm{FB}} = 10$.

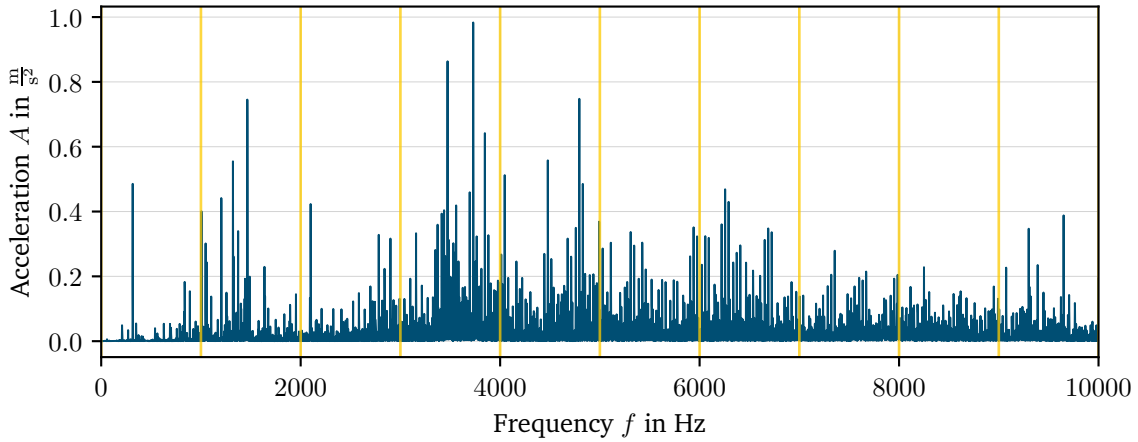

Figure 4.5.: Equally sized frequency band separation (yellow) of an amplitude spectrum (blue) into ten frequency bands; according to [72].

The number of frequency bands N_{FB} can be tuned to optimize the performance of an ML-based model for fault diagnosis. In general, the Frequency Band (FB) processing method was analyzed to be computationally efficient in comparison to other methods of data processing. Originally, only the mean values were proposed for feature calculation based on the separated frequency bands [81, 82]. Furthermore, the calculation of the complete range of frequency-domain features, presented in table 4.3, was applied on the separated frequency bands. As part of the most recent publication of the present author, superior predictive performance of ML-based fault diagnosis models was obtained when comparing the FB processing methods to other processing techniques using the CWRU data set [72].

4.3.2. Convolution

Convolution is a mathematical operation in which two signals are combined to form a third signal. This operation is used in several sections of this work and shall therefore be explained here. To emphasize the importance of convolution, SMITH uses the following words: "Using the strategy of impulse decomposition, systems are described by a signal called the impulse response. Convolution is important because it relates the three signals of interest: the input signal, the output signal, and the impulse response." [83, p.107]. Thus, convolution is a crucial operation when investigating the interrelationship between excitation and response of a system's structural dynamic.
The convolution of two signals s and u is denoted by $s * u$ and defined according to equation (4.5). Here, the result of the convolution is designated as r.

$$r(t) = s(t) * u(t) = \int_{-\infty}^{\infty} s(\tau)u(t-\tau)\,d\tau \tag{4.5}$$

An important property of the convolution operation is its commutativity: $s * u = u * s$ [13, pp.74-75]. According to the convolution theorem, the proof of which is presented in appendix A, the time-domain convolution is mathematically equivalent to the frequency-domain multiplication. Thus, with R, S, and U being the Fourier transformed frequency-domain representations of the time-domain signals r, s and u, the following holds true.

$$R(f) = S(f) \cdot U(f) \tag{4.6}$$

Therefore, according to the convolution theorem, the operation of convolution in time-domain can be implemented computationally efficient by means of the more simple operation of multiplication in frequency-domain.
The convolution of signals by certain kernel functions can be used to process them in a modifying manner. For example, a common smoothening approach is given by the Gaussian filtering, which uses a Gaussian kernel function g for convolution [84, p.6].

$$g(t) = \frac{1}{\sqrt{2\pi}\sigma} e^{-\frac{t^2}{2\sigma^2}} \tag{4.7}$$

Here, the amount of smoothening is defined by the standard deviation σ of the Gaussian kernel. The smoothed signal $\tilde{s}$ is defined as follows.

$$\tilde{s}(t) = s(t) * g(t) \tag{4.8}$$

In the further course of this thesis, Gaussian filtering is applied in chapter 7 to create smoothed visualizations of frequency-domain spectra.

4.3.3. Wavelet Transform

The Wavelet Transform (WT) was originally introduced by MORLET, primarily for the purpose of analyzing seismic measurement data [85]. In the past decades, numerous variations of the WT have been proposed, leading to the discovery of many additional

applications. One such variation is the Continuous Wavelet Transform (CWT), which provides a time-frequency representation of a signal. It is expressed by the following integral [84, p.242]:

$$W(b_1, b_2) = \frac{1}{\sqrt{|b_1|}} \int_{-\infty}^{\infty} s(t)\psi^* \left(\frac{t - b_2}{b_1} \right) dt \tag{4.9}$$

Here, $\psi(t)$ is a so-called mother wavelet, which has a fixed shape, but can be shifted in time by b_2 and dilated by the factor b_1, with $\psi^*(t)$ denoting the complex conjugate of $\psi(t)$. A very commonly used mother wavelet for signal analysis is given by the complex Morlet wavelet [84, p.246], which is defined as follows:

$$\psi(t) = \frac{\sigma}{\sqrt{\pi}} e^{-\sigma^2 t^2} e^{j2\pi f_0 t} \tag{4.10}$$

This Morlet wavelet represents a Gaussian-windowed sinusoid, with f_0 parameterizing its center frequency and σ specifying its width [13, pp.131-133].
In contrast to the Short-Time Fourier Transform (STFT), the resolution in time and frequency of the CWT is not constant. The CWT provides a high time-resolution and a low frequency-resolution for the high frequency range. Vice versa, the low frequency range is presented in low time-resolution and high frequency-resolution [84, p.243]. For the vibration-based analysis of technical systems, this property of the CWT can be beneficial, since those systems in practice often times are subject to rapid changes in high frequencies, while only slow changes are present in low frequencies [71, p.64]. For this reason, the CWT is preferred over the commonly used STFT for the creation of time-frequency domain visualizations in the data exploration section 6.1 of this work.

4.3.4. Hilbert Transform

For vibration monitoring of rolling bearings, envelope analysis is a widely used technique to separate the fundamental excitation frequencies from the high-frequency vibrations of a technical system [13, pp.49-50]. Figure 2.4 already presented idealized vibration patterns and corresponding envelope signals. There, it was shown how envelope signals can be utilized to localize rolling bearing faults. To generate the envelope signals, a demodulation of the original signal has to be performed, which can be implemented by applying the so-called Hilbert Transform (HT) [13, pp.95-103]. In general, the HT of a signal is defined as follows, resulting in the Hilbert transformed signal s_{H} [71, p.58].

$$s_{\mathrm{H}}(t) = \frac{\int_{-\infty}^{\infty} \frac{s(t)}{t-\tau}\, d\tau}{\pi} = s(t) * \frac{1}{\pi t} \tag{4.11}$$

The HT can therefore be seen as a convolution of the original signal s with $\frac{1}{\pi t}$. Having both the original signal s and its Hilbert transformed s_{H}, the analytic signal z can be calculated.

$$z(t) = s(t) + j s_{\mathrm{H}}(t) \tag{4.12}$$

Moreover, the so-called instantaneous amplitude z_a provides an envelope of the original signal s. It is given by the amplitude of the complex-valued analytic signal.

$$z_a(t) = |z(t)| = \sqrt{s^2(t) + s_H^2(t)} \tag{4.13}$$

This HT-based instantaneous amplitude is used later in section 6.1 to generate the envelopes of the measured acceleration signals for data exploration. Afterwards, the envelope signals are used for feature generation in section 6.3.

4.4. Structure-Borne Sound

In the later chapters of this work, knowledge on structure-borne sound is required to understand the root cause of the measured acceleration signals and to generate novel data processing approaches for fault diagnosis. Introducing into this topic, the term structure-borne sound refers to the "field of physics, which encompasses generation, transmission, propagation and radiation of wave motions in solid structures" [86, p.1]. As presented in figure 4.6, the generation of sound can generally be differentiated to be either direct or indirect.

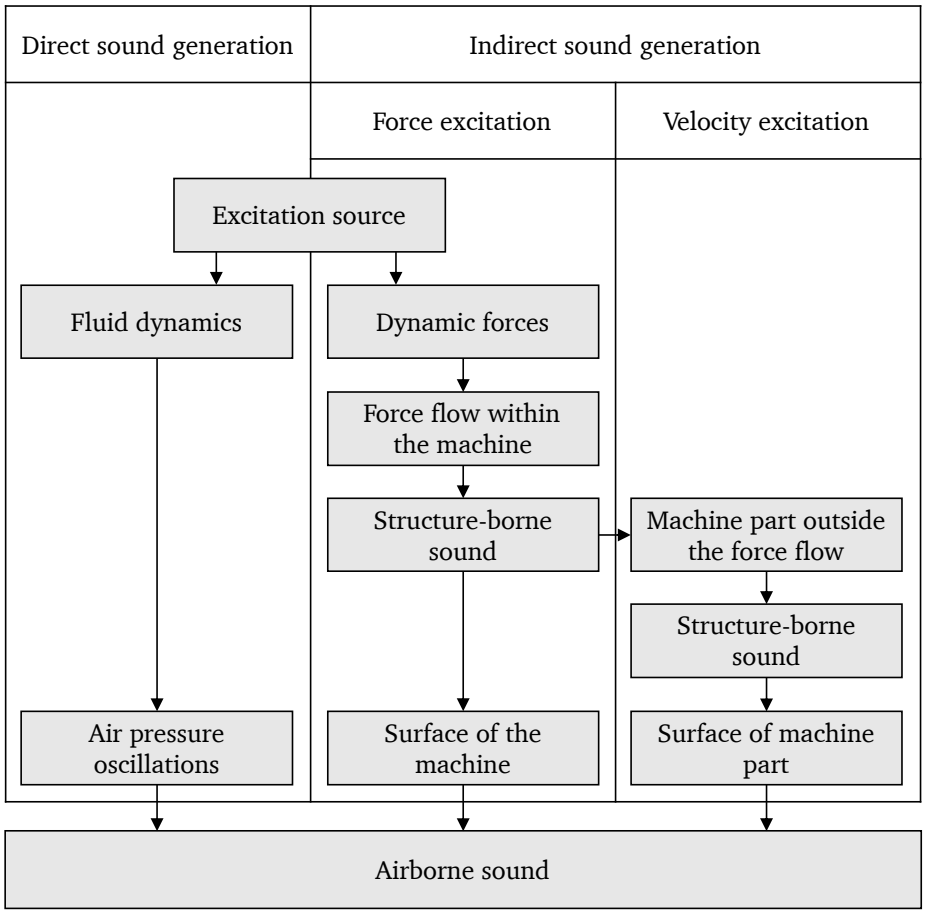

Figure 4.6.: Direct and indirect generation of sound; according to [62, p.O34].

Within the present work, the indirect, force excited sound generation is of interest with a particular focus on structure-borne sound propagation from the dynamic forces to the surface vibrations of the machine. The dynamic excitation forces that excite the structure of a machine, usually originate from the machine's operating forces which are essential for the function of the machine [62]. Additionally, a fault of the machine can cause changes of excitation forces. This latter effect is utilized in vibration-based condition monitoring [3].
A particularly important aspect in the generation of machine vibrations is the transmission path from a dynamic force excitation to the resulting vibration at a point on the structure. The behavior of this transmission path can be quantified in terms of its Frequency Response Function (FRF).

4.4.1. Frequency Response Functions

The FRF represents the relationship between excitation and response of a system. Thus, it describes the systems transmission behavior between the point of excitation and response. In the context of structural vibrations, the excitation is usually described by its force. The response can be measured using either displacement, velocity, or acceleration of the vibration [87, p.14]. Knowing the excitation and the FRF of a system, the corresponding vibration response is calculated via convolution. For the given case, the response is considered to be measured in terms of acceleration. Therefore, the so-called accelerance h represents the frequency response funcion by mathematically describing the transmission behavior inbetween an excitation force e and its acceleration response a. According to equation (4.14), the acceleration response a can be calculated by convolving the force excitation e and the accelerance h [87, p.361].

$$a(t) = h(t) * e(t) = \int_{-\infty}^{\infty} h(\tau) e(t-\tau)\, d\tau \tag{4.14}$$

Equation (4.14) can be transformed with the help of the convolution theorem, the proof of which can be found in appendix A. Accordingly, the corresponding frequency-domain representation of equation (4.14) is given by a pointwise multiplication as stated in equation (4.15).

$$A(f) = H(f) \cdot E(f) \tag{4.15}$$

The accelerance of a transmission path can be determined experimentally by exciting the structure with a known excitation force and measuring the responding acceleration. On the one hand, the excitation can be provided by a sweeping sine signal, exciting only one frequency simultaneously. On the other hand, a broad band excitation can be applied, exciting the complete frequency spectrum of interest at once. Most important excitation signals for broad band excitations are white noise and the dirac impulse, both of which in theory provide constant power density to the entire frequency range [87, p.361].

For real measurements, one option is to excite the structure with a sine sweep or white noise excitation using a so-called shaker. Another option is to use an impulse hammer to excite the structure with an approximated dirac impulse. For the present work, the impulse hammer method is considered in more detail due to its versatile operability.

4.4.2. Impulse Hammer Method

To calculate the accelerance using an impulse hammer, the structure is excited by knocking at the desired points of excitation. The impulse hammer is equipped with a force sensor inside its tip to measure the applied force impulse. Additionally, an accelerometer is applied at the desired response point of interest. As visualized in figure 4.7, the acceleration behaves in response to the systems structural dynamics. Knowing both the hammer-based force excitation e_h and the corresponding acceleration a_h, the accelerance can be determined in frequency-domain by pointwise division of the acceleration A_h by the force excitation E_h.

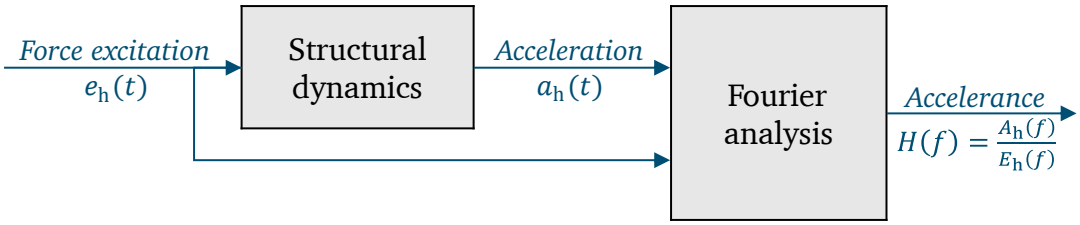

Figure 4.7.: Schematic of impulse hammer method; according to [87, p.362].

In contrast to the theory, where an idealized impulse excites the structure with constant power density for all frequencys, in reality the frequency range is limited inverse proportionally to the duration of the non-idealized impulse. Thus, a shorter impulse duration leads to a larger frequency range. The impulse duration can be influenced by the tip material of the hammer and its weight. Harder tip materials and lower hammer weights lead to shorter impulse durations and thus to higher frequency ranges. However, this combination also decreases the frequency-wise force magnitude and thus increases the influence of noise in Fourier analysis.
Given the introduction of fundamental methods within the present chapter, the now following chapter 5 focuses on the experimental data acquisition which is necessary to address the defined Research Questions.

5. Experimental Data Acquisition

With the aim of providing a suitable data set to tackle the Research Questions raised in chapter 3, the present chapter focuses on the experimental data acquisition. Firstly, the experimental design is elaborated in section 5.1. Furthermore, the test bench setup and the preparation of bearing faults are introduced in sections 5.2 and 5.3. Finally, the experimental procedure is presented in section 5.4.

5.1. Experimental Design

The main topic of Research Questions 1 and 3 is to evaluate the fault diagnosis accuracy in a transfer scenario from a reference system (source domain) to a system with differing properties in structural dynamics (target domain). For information on the general principle of transfering an ML model from a source domain to a target domain, please refer to section 2.5. To enable the investigations on model transfer in the given fault diagnosis case based on experimental data, the experimental requirements are specified in section 5.1.1. Building upon this, section 5.1.2 introduces the experimental concept.

5.1.1. Determination of Experimental Requirements

To derive the experimental requirements, an overview of possible influencing factors on vibration signals for fault diagnosis is required. It is important to emphasize that there are a variety of influencing factors beside the actual bearing fault having impact on the vibration measurement signals. Thus, the complete effect chain of influences on the measurement data has to be taken into account for the determination of requirements. Figure 5.1 extends the considerations already presented in figure 3.1 by visualizing the chain of potential influencing factors when transferring a trained, vibration-based, data-driven fault diagnosis model to a different system in general.
Starting at the top of figure 5.1, fault development is mainly influenced by the bearing design itself and the operating condition it is working in. Given a bearing fault, the dynamic force excitation depends on several influences. On the one hand, it is influenced by the bearing fault itself. If a bearing fault arises or propagates, this leads to changes within the dynamic force excitation at the bearing raceway. Rolling contact fatigue for example can cause spalling and thus surface irregularities at the raceway, leading to dynamic force excitations when a rolling element passes. Here, the amount of force excitation is dependent on the fault severity. On the other hand, both bearing design and operating conditions influence the force excitation. The bearing design for example has the bearing fundamental frequencies as its dependent properties via the number of

rolling elements, which affect the force excitation frequency. Additionally, changes in the operating condition like varying bearing forces or rotational speeds affect the excitation amplitude and its frequency.

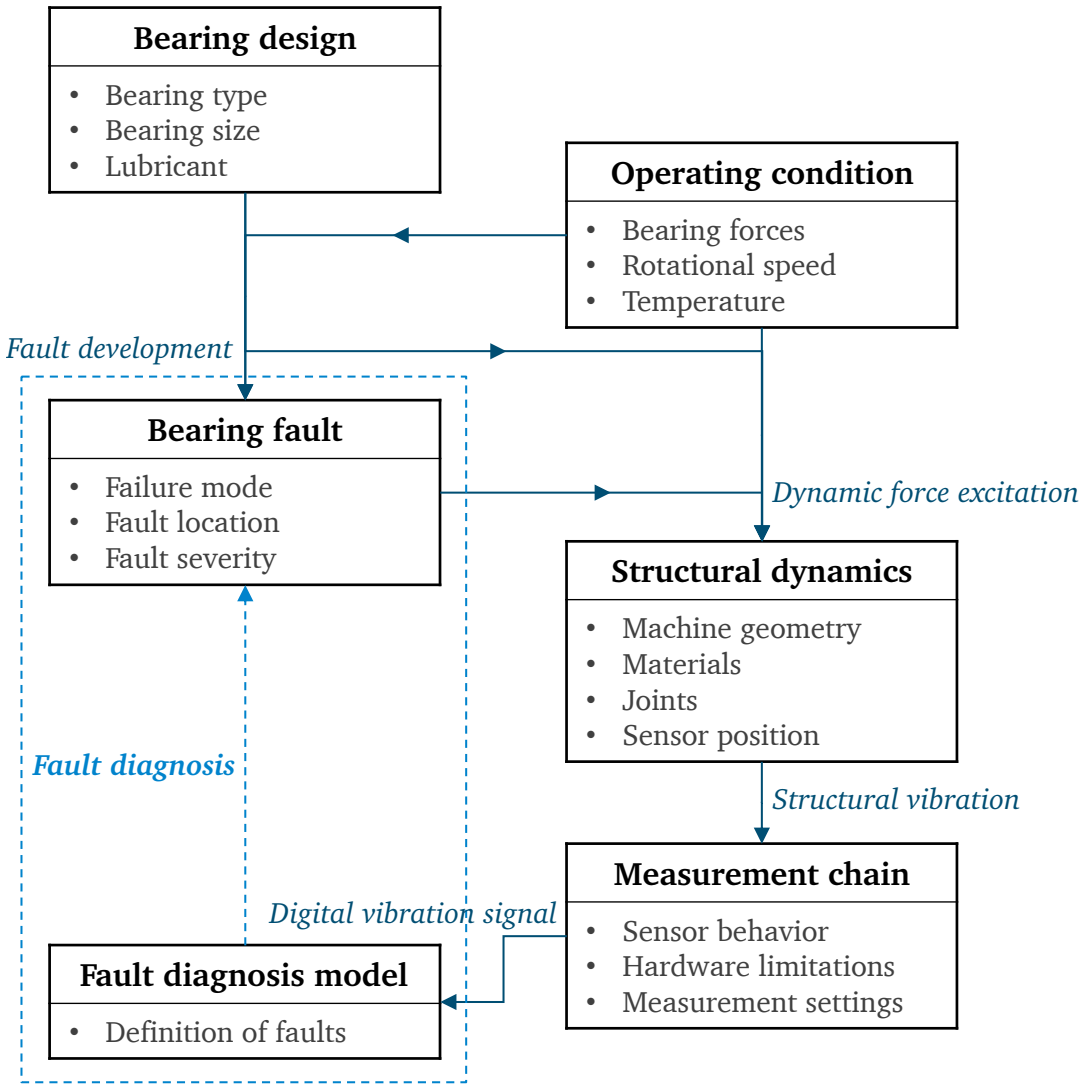

Figure 5.1.: Effect chain of influencing factors on vibration-based fault diagnosis.

Assuming a given force excitation, the structural dynamics of the system and especially the properties of vibration transmission inbetween the bearing and the vibration-measuring sensor modify the vibration behavior at the sensor location.
This vibration is measured using a measurement chain to receive a digital signal. Since different measurement equipment may have different characteristics and limitations regarding its hardware as well as its software, the digital signal can differ inbetween different measurement chains.
After passing all these influencing factors, the digital vibration signal can be used for fault diagnosis. It becomes clear that the bearing fault itself is not the only influencing factor

on the vibration signal. Instead, additionally the bearing design, its operating conditions, the structural dynamics and measurement chain may change from one system to another. As already derived in section 3.1, the present work aims to bridge the research gap regarding differing structural dynamics. Therefore, the influence of differing structural dynamic properties shall be investigated and reduced using an isolated approach. Thus, on the one hand, the structural transmission paths must be differable within the data acquisition. Additionally, the bearing faults need to be variable in order to build a data-driven fault diagnosis model. On the other hand, all influencing factors except the structural dynamics must be kept constant to avoid them interfering within the investigations. Given this context, the following fixed experimental requirements R1 to R5 are derived: The experimental setup must enable ...

- R1: ...variable structural dynamic behaviors inbetween a test bearing and the sensor(s) for influence investigation.
- R2: ...variable bearing faults to enable fault diagnosis.
- R3: ...a fixed bearing design: Constant bearing type, size and lubricant.
- R4: ...a fixed operating condition: Constant bearing forces, rotational speed and temperature.
- R5: ...a fixed measurement chain: Constant sensor type, hardware and measurement settings for data acquisition.

An additional requirement derives from the state of research of available scientific datasets for bearing fault diagnosis, presented in section 2.3.3. A shortcoming within those data sets is that they do not provide consistently separated training and testing experiments for the exact same faults and operating conditions. Thus, to test a ML model, training and testing in past literature usually is performed based on exactly the same experimental runs. This cannot ensure that the actual bearing fault is detected, since other test bench properties, such as the joint stiffness of screw connections, may have changed during the process of bearing replacement. These changes can cause the vibration data to differ between different experimental runs, even without any fault modifications being introduced to the bearing. To eliminate the ambiguous cause of distinguishable vibration signals for fault diagnosis, the following additional requirement R6 is set up:

- R6: Training data and testing data must be acquired from separated experimental runs.

In addition to the previously stated fixed requirements, an additional wish is set up for the experimental design. As this research is motivated by enhancing bearing fault diagnosis for automotive e-machine applications, the following would be beneficial:

- R7: Ideally, the data for bearing fault diagnosis is acquired from a real e-machine which is designed for automotive applications.

Using all the requirements presented above, the experimental concept is introduced within the following section.

5.1.2. Experimental Concept

Main goal of the experimental concept is to meet the fixed requirements R1 to R6 and the wish R7. Furthermore, the concept shall be as simple as possible to minimize uncertainties resulting from experimental complexity.
Addressing requirement R1, there are different possibilities to vary the vibration transmission path resulting from the structural dynamic properties. As already shown in figure 5.1, the structural properties depend on the machine's geometry, the materials of the single parts as well as their joints. Additionally, the positioning of the sensor does influence the measured vibration. In order to elaborate Research Questions 1 and 3, the variation of one single influencing factor on the vibration transmission is sufficient. Among the given options, the most simple solution for varying the transmission path inbetween bearing and sensor is to mount multiple sensors of the same type at different locations on a single test bench structure.
In order to fullfill requirement R2, two alternatives are feasible in accordance with the literature, as already introduced in section 2.3.3. On the one hand, faulty bearings can be prepared in advance and then let run inside the test bench. Since the corresponding labels of the prepared faults are known, this concept enables fault diagnosis through supervised learning via classification. On the other hand, naturally progressing bearing faults can be used to build a regression task. The regression concept brings uncertainties regarding labeling, since the bearing fault cannot distinctly be assessed during complete test run operation. In comparison, the classification concept can be applied in a simpler and more precise way based on bearing faults being prepared in advance. Therefore, it is the preferred concept for the present investigations. In particular, it is aimed for a classification based on balanced data. This means that all classes set up shall be represented by an equal amount of data samples.
According to requirements R3 to R5, all further influencing factors are supposed to remain constant during the experimental procedure. To ensure this, one single technical system is to be used at constant operating conditions for all the experimental runs. Additionally, to fulfill the wish R7, the experimental investigations shall focus on a rolling bearing inside an automotive e-machine.
Addressing requirement R6, each prepared bearing has to run within two separated experimental runs to provide clearly separated experimental data for training and testing. For further bias reduction, the order of the experimental test runs is to be shuffled inbetween the two experimental series. Taking into account the considerations outlined above, the derived experimental concept and the subsequent data processing are visualized in figure 5.2. According to this concept, the data is acquired from two independent experimental series A and B. Within each series, the same prepared test bearings are run at constant operating conditions within the same test bench e-machine. The number of differently prepared bearings for classification is denoted by N_{C}. To ensure different structural dynamic properties, data is recorded from a number of individual sensors N_{S} of the same sensor model, each placed at a different location at the test bench.

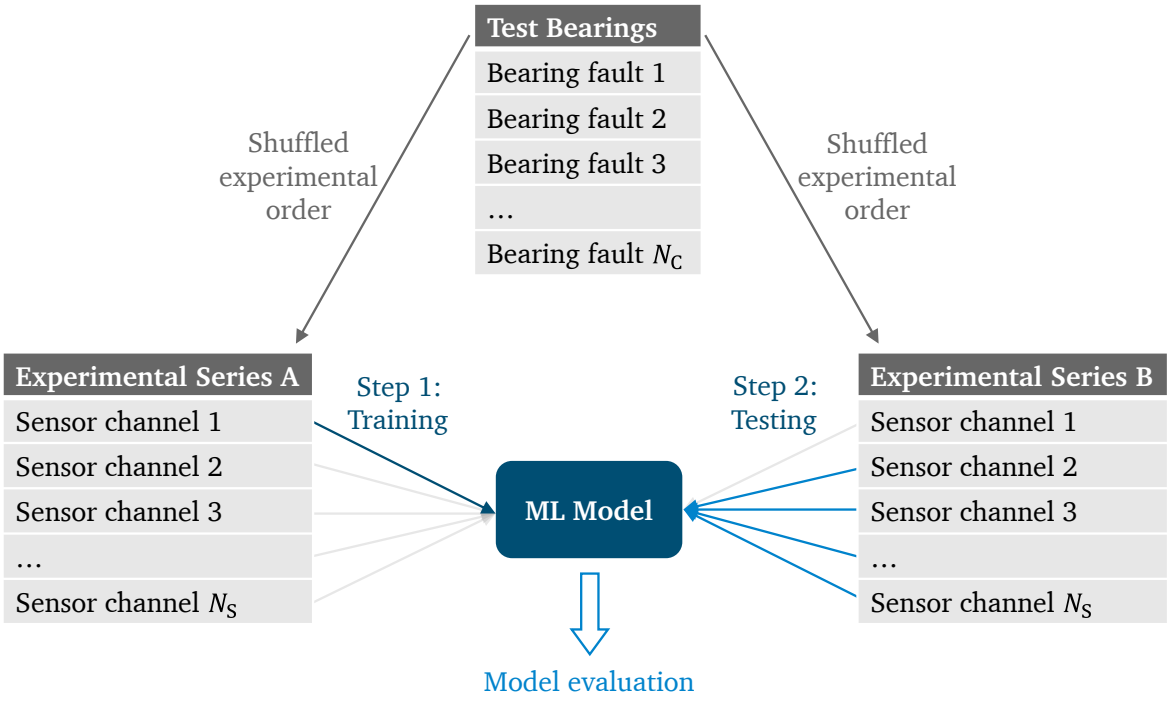

Figure 5.2.: Concept for the experimental data processing.

For final evaluation of the ML-based fault diagnosis models regarding their transferability, a cross-validation is used. Therefore, per iteration during cross-validation only one sensor channel from one experimental series is used for the training step. For performance evaluation realized within the testing step, the predictions based on the remaining $N_S - 1$ sensor channel data from the second experimental series are used for accuracy determination. Since the sensor data used for training can be varied inbetween all N_S sensor channels from both of the experimental series, this conceptual setup allows for a cross-validation with $2 \cdot N_S$ folds. This enables statistical analysis of the fault diagnosis results for model evaluation.

5.2. Test Bench Setup

According to the experimental requirements presented in section 5.1.1, the test bench in use is built for research on bearing fault diagnosis in e-machine applications. The particular e-machine in use for the present investigations is a separate motor-generator with 60 kW of nominal power. Specifically, it is a Permanent-Magnet Synchronous Motor (PMSM), primarily developed for use in off-highway applications for the automotive industry and mobile machinery. Its detailed specifications are provided within the appendix at table B.1. A picture of the complete test bench setup including the described PMSM is shown in figure 5.3.

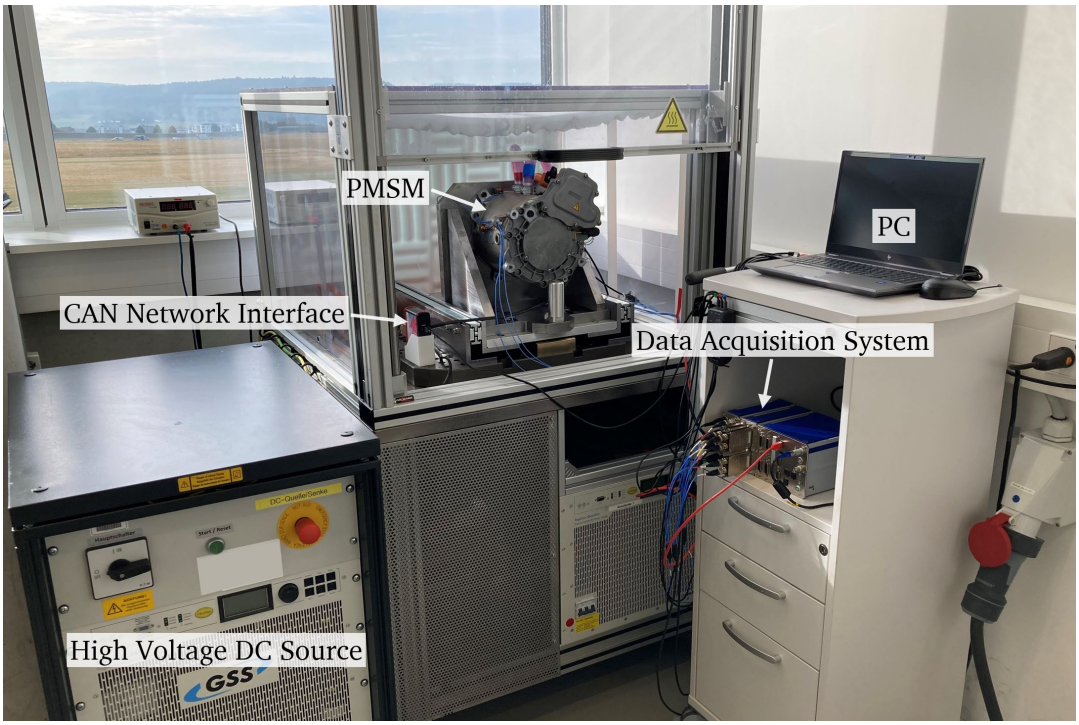

Figure 5.3.: Picture of the e-machine bearing fault test bench.

Additionally, the interactions inbetween the test bench components are schematically visualized in figure 5.4.

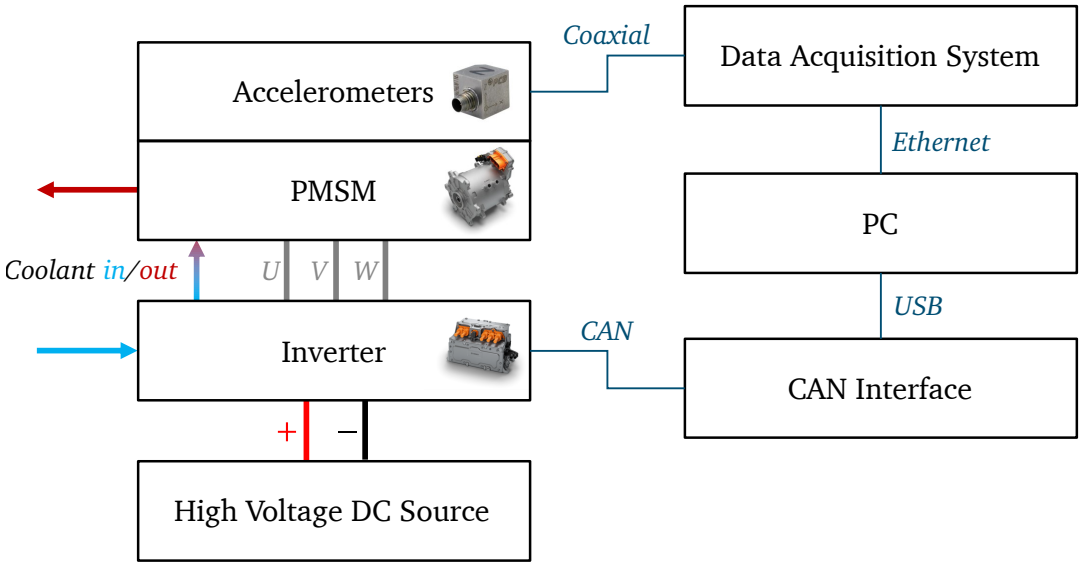

Figure 5.4.: Schematic test bench setup;
Image sources: Accelerometers [88], PMSM [89], Inverter [90].

The high voltage Direct Current (DC) source provides 400 V to power the inverter. The target rotational speed of the PMSM can be set at the Personal Computer (PC).

The Controller Area Network (CAN) interface is connected to the PC and provides the control signals to the inverter. Based on the control target, the inverter supplies the corresponding phase currents to the PMSM.
The main machine element of interest during the investiations within the present work is one of the two ball bearings inside the PMSM, which is located at the shaft connection side. For further details on the internals of the PMSM, figure 5.5 provides a sectional view.

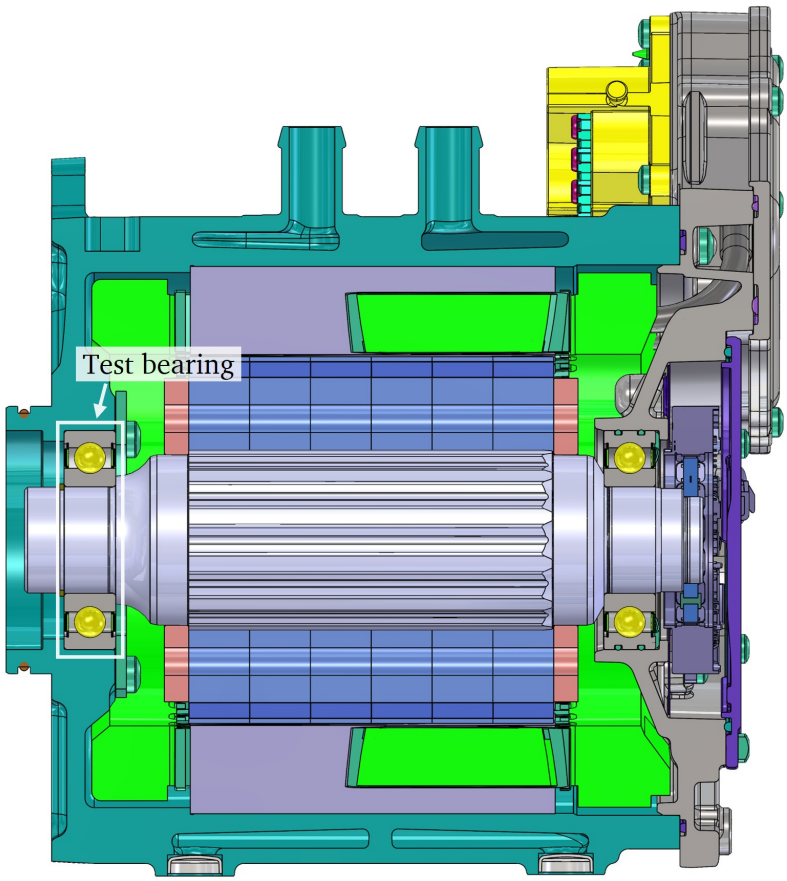

Figure 5.5.: Sectional CAD visualization of the PMSM.

In addition to the CAD visualization in figure 5.5, figure 5.6 presents a picture of the PMSM as it is mounted on the test bench. For data acquisition, three PCB Piezotronics Model 356A15 triaxial accelerometers are glued to the test bench at different locations. The placements of the accelerometers are selected to have different vibration transmissions inbetween test bearing and sensors. Therefore, sensor 1 is placed at the the solid steel mounting plate of the test bench construction. Sensors 2 and 3 are mounted directly onto the PMSM, sensor 2 beeing located near to the test bearing and sensor 3 having a greater distance in axial direction.

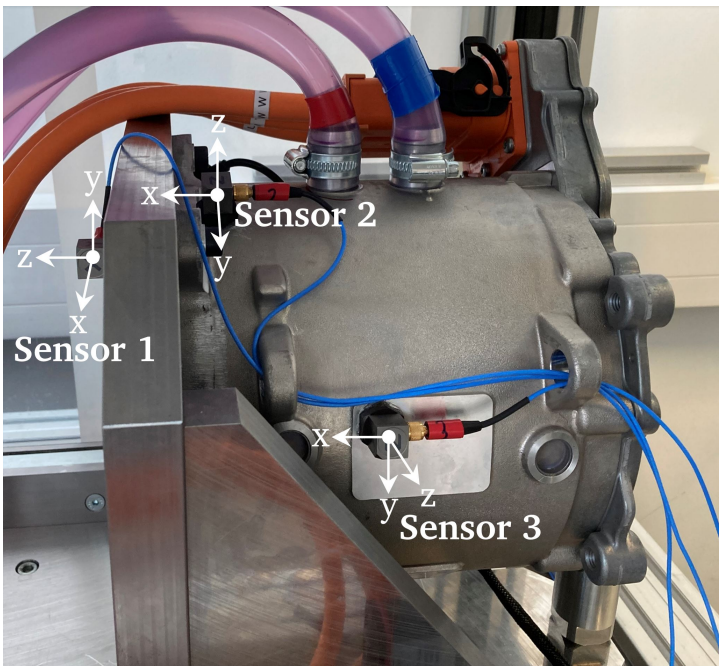

Figure 5.6.: Sensor placements at the test bench.

The differences of the vibration transmissions inbetween the test bearing and the different sensors are verified by measuring the FRFs, see section 7.1.1. Each sensor comprises three separate channels according to their x-, y- and z-directions. The total of nine sensor channels of the three sensors are connected to a data acquisition system via coaxial cables, which itself connects to the PC via Ethernet. Guided by the publicly available data sets, presented in section 2.3.3, a sampling rate of 20 kHz is chosen for data acquisition. To satisfy the Nyquist-Shannon sampling theorem [91], an anti-aliasing filter is used inside the acquisition system to suppress any analog frequency components above 10 kHz. Specifically, an 8^{th}-order low-pass with Cauer characteristics is used for this purpose at a cutoff frequency of 8 kHz. Furthermore, the acceleration amplitude is recorded with a resolution of 24 bits.

5.3. Preparation of Bearing Faults

Within section 5.1.2, the experimental concept and the design for a classification-based data processing was derived. Based on this experimental design, the bearing faults have to be prepared, which are to be classified later on.
The test bearings inside the test bench PMSM are specified to be 6207 deep groove ball bearings with a radial bearing clearance of C3H and sealings of type 2Z. The cages are made of plastic in a snap-type design and the lubrication is provided by grease. Specifically, a heat-resistant and low-noise urea grease is used, which is designed for use in outer ring rotating bearings. Figure 5.7 shows the components of a disassembled test bearing without grease.

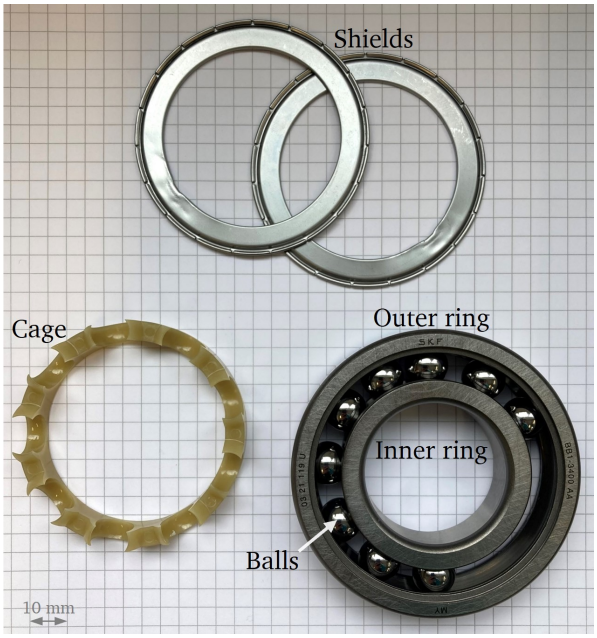

Figure 5.7.: Partially disassembled test bearing.

Guided by the fundamentals on damaging mechanism presented in section 2.3.1, four specific bearing faults are selected for preparation. Here, the aim is to represent a wide variety of damaging mechanisms. The naming of the prepared bearing faults, their description and the represented damaging mechanisms are listed in table 5.1. For the failure modes, the naming conventions as given by ISO 15243 [31] are used, which were already introduced in table 2.1. In addition to the four bearing faults, an undamaged reference bearing is used for the investigations.

Table 5.1.: Bearing faults mapped to failure modes.

Bearing name	**Bearing fault description**	**Represented failure mode**
Reference	No fault	No failure
Brinell	Static overload at $2 \cdot C_0$	Plastic deformation
Corrosion	Corrosion in hydrochloric acid for 2 h	Corrosion
IR Laser	Inner race laser-ablated 120 µm groove	Rolling contact fatigue
OR Laser	Inner race laser-ablated 120 µm groove	Rolling contact fatigue

Thus, the 5 different bearings shown in figure 5.8 are prepared, which are to be detected later using the ML-based fault diagnosis. Accordingly, the classification algorithms have to distinguish between $N_C = 5$ different classes, which are specified by the bearing names.

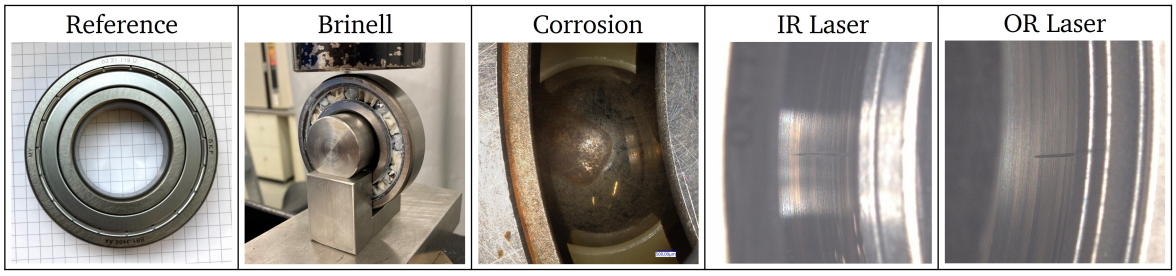

Figure 5.8.: Preparated bearing faults.

To prepare the Brinell fault, first, one of the two bearing shields is removed to reveal the ball locations. Next, the bearing is placed at a hydraulic press as visualized in figure 5.8 (Brinell), sitting at its inner ring. A force of 30.6 kN is applied radially to the outer ring, with one of the balls located in the center to transmit the maximum amount of force. The applied force corresponds to twice the basic static load rating $C_0 = 15.3$ kN of the type 6207 bearing. Accordingly, this static overload leads to plastic deformations at the contact areas. After introducing the Brinell fault, the shield is reinstalled and the bearing is ready for the experimental runs.
For the preparation of the Corrosion, Inner Race (IR) Laser and Outer Race (OR) Laser faults, the two shields and the grease are removed completely. For the corrosion fault, the bearing is placed into hydrochloric acid for 2 hours. Afterwards, it is cleaned, refilled with new grease and the shields are reinstalled. For the IR and OR Laser faults, additionally, the snap-type cage is removed in a non-destructive way. Next, the balls are pushed aside and fixed to enable the laser ablation process. After introducing the faults by using an ultrashort pulse laser, the bearings are cleaned and all parts are remounted, including the insertion of new grease.
For further fault specification, figures 5.9 and 5.10 show surface topographies of the IR Laser and OR Laser faults. The surface topographies presented in these figures are measured after performing the experimental runs. Thus, the bearings and their faults are already run-in before measuring the topographies. The measurements are conducted with a Hommel Etamic Waveline 920 which uses a tactile method for scanning the surface. Reason for using the tactile measurement instead of other surface measurement techniques like optical measurements is the accessibility of the raceways. The tactile measurement technique does not require the bearings' inner and outer rings to be disassembled completely. As the rings would have to be deformed during this complete disassembly, plastic deformation of the material could not be ruled out. This is therefore avoided here by using the tactile measurement, for which only bearing shields, grease and cage have to be removed to obtain the surface measurements.

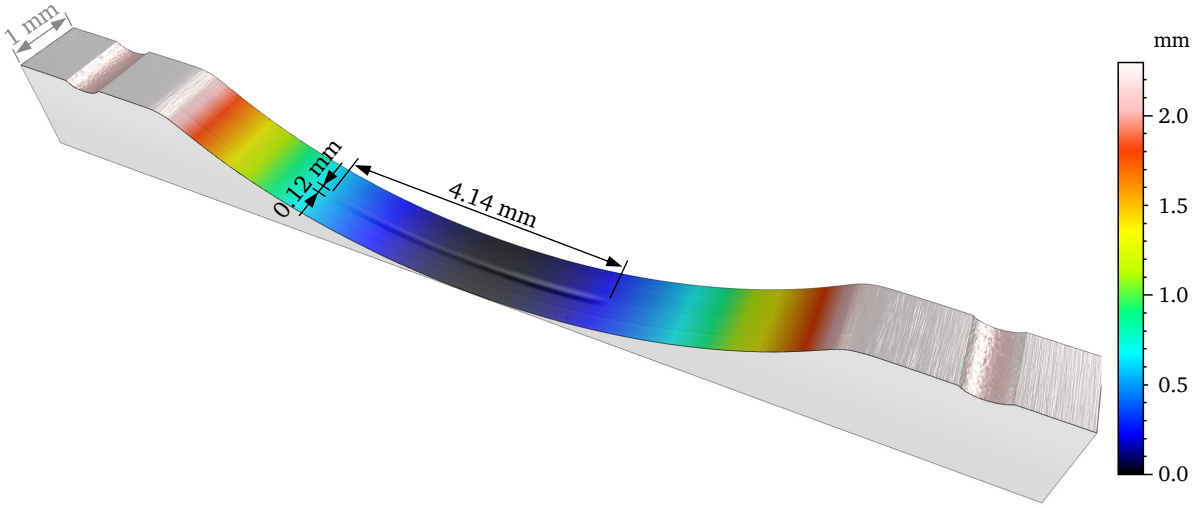

Figure 5.9.: Measured topography of the IR Laser fault.

Both IR and OR Laser faults show a width of 120 µm. The balls of the given type 6207 bearings have got diameters of 11.11 mm. Assuming ideal kinematics for a ball passing the IR Laser fault, the generated movement of the ball in radial direction is limited to 0.4 µm due to the small fault width. The depth of the fault is 5 µm with only slight variations in axial direction. Thus, the fault depth does not constrain the ball movement from a kinematic point of view. Overall, the generated IR and OR faults are considered to be of very little severity.

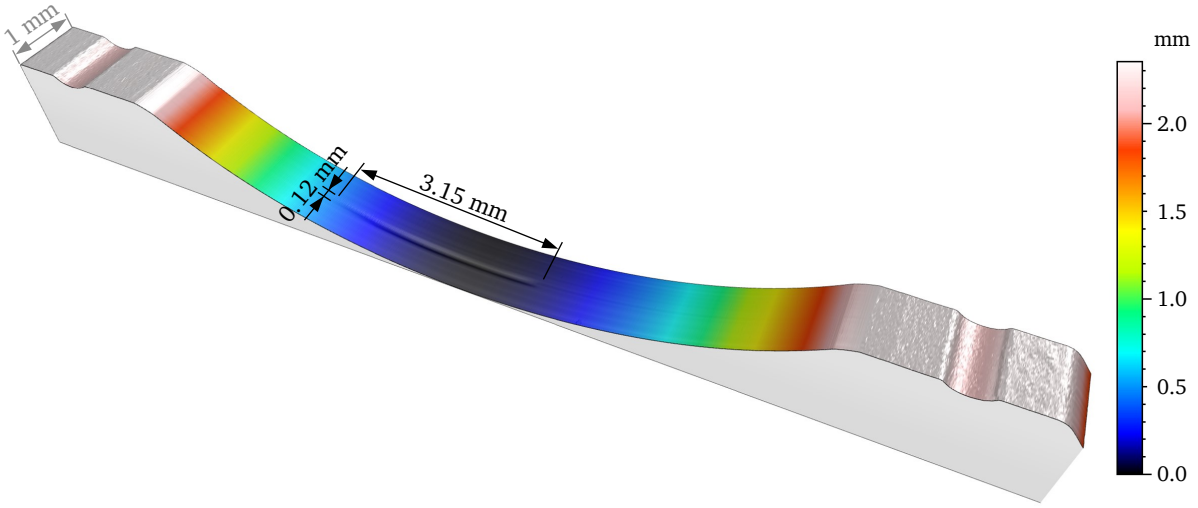

Figure 5.10.: Measured topography of the OR Laser fault.

The IR and OR faults are not perfectly centered in axial direction. To ensure that the balls get in contact with the faults during the later experiments, the bearings are oriented inside the PMSM by taking the contact angle, which is dependent on the axially

applied preloading forces, into account. Having prepared all five bearings, the following section 5.4 explains the procedure for conducting the experiments.

5.4. Experimental Procedure

As already derived conceptually in section 5.1.2, each of the prepared bearings is to be installed two separate times within the PMSM. In practice, two separate experimental series A and B are performed in sequential order. Shuffling the order of the experimental runs inbetween both series as shown in figure 5.11 avoids bias that could arise from the experimental order.

Series A experiments	
Order	**Test bearing**
1	IR Laser fault
2	OR Laser fault
3	Brinell fault
4	Corrosion fault
5	Reference

Series B experiments	
Order	**Test bearing**
6	OR Laser fault
7	Reference
8	IR Laser fault
9	Brinell fault
10	Corrosion fault

Figure 5.11.: Order of the test bearings within two separate experimental series.

The exchange of the test bearing requires a comprehensive procedure of disassembly and reassembly. The steps to perform during the process of disassembly are briefly outlined within the following list:

- Disconnect all cables and dismount the PMSM from the test bench.
- Transport the PMSM to the nearby workshop and mount it at the modified lathe, visualized in figure 5.12.
- Open the PMSMs back side and extract the stator from the rotor.
- Change the test bearing.

Once the test bearing is replaced, the entire process is performed in reverse to reassemble the PMSM on the test bench.

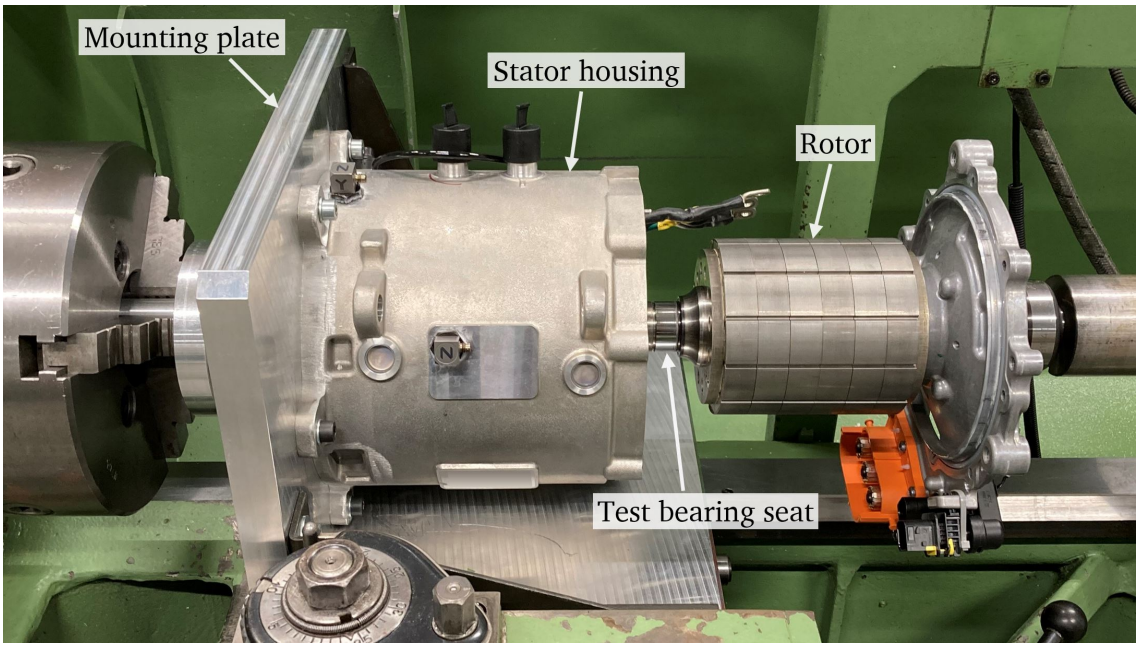

Figure 5.12.: Picture of the PMSM at a modified lathe during bearing replacement.

When mounting a test bearing inside the PMSM, which has got a prepared fault on its outer race, its orientation with respect to radial, gravitational forces is crucial. Thus, for the OR Laser and Brinell faults, the outer rings orientation is ensured to have its main fault at the bottom side of the PMSM. In this way, the fault location is ensured to be inside the load zone due to the rotors gravitational forces.
During reassembly of the PMSM and its installation on the test bench, it is particularly important to keep the assembly process controlled to minimize changes with respect to structural dynamics. These changes potentially can occur due to differing properties of the joints, such as their stiffness and damping. Therefore, all screws are tightened in a consistent sequence using defined torques. Additionally, a dedicated lubricant is applied to the screw threads to minimize fluctuations in the tightening forces due to varying coefficients of friction.
Once the test bearing is replaced and the PMSM is set up again at the test bench, the experimental run can start. As already specified for the experimental requirements in section 5.1.1, the operating conditions shall be kept constant for all experimental runs within this work. For this purpose, each experiment is performed at a fixed rotational speed of 3500 rpm. The motor is running freely without any torque applied. Additionally, the motor is permanently cooled by a 15 °C water-based coolant. As visualized in figure 5.13, the PMSM runs for 5 hours before the actual measurement acquisition for the later investigations takes place in order to enable sufficient run-in of the bearing and to ensure a quasi-steady-state operating condition. After run-in, measurement data is recorded for 5 minutes.

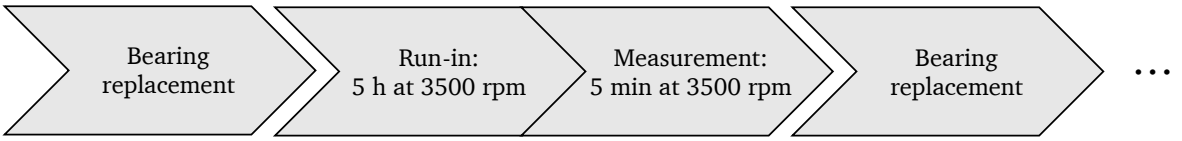

Figure 5.13.: Sequence of the experimental procedure for data acquisition.

Accordingly, 300 seconds of measurement data are acquired from each of the 9 sensor channels per experimental run. This data acquisition is carried out for all 10 experimental runs, using each of the 5 different bearings twice, as already described in figure 5.11. Given the resulting set of vibration data, the now following chapter 6 addresses the ML-based fault diagnosis.

6. Fault Diagnosis Based on Vibration Data

This chapter aims to answer Research Question 1 by investigating the fault diagnosis performance based on vibration data. Therefore, first the measured data itself is explored in section 6.1 using several techniques of visualization. Section 6.2 then introduces the procedure for evaluating the transferability of the data-driven fault diagnosis models. Based on the feature engineering investigations and ML hyperparameter optimizations described in sections 6.3 and 6.4, the resulting diagnosis performance of the vibration based model is presented and concluded with respect to the former Research Question 1 in section 6.5.

6.1. Data Exploration

The present section focuses on the explorative analysis of the recorded measurement data in order to perform a plausibility check for each individual bearing fault measurement. Additionally, the differences inbetween various sensor channels are analyzed. Therefore, different visualizations are utilized to inspect the data in time-domain, frequency-domain, and time-frequency-domain.
For a first visualization, figure 6.1 shows the time-domain RMS, calulated for each single measurement second and plotted for the 300 seconds of recorded measurement data. As already introduced in section 2.3.2, the RMS-based analysis of an acceleration signal enables the comparison of the overall vibration strength. To preserve the clarity within figure 6.1, only three sensor channels and two experimental runs are visualized. For the sensor channels, the signals of the axial directions of each physical sensor (1z, 2x and 3x) are chosen. The corresponding sensor placements and their axis orientations can be found in figure 5.6. For now, only the Reference bearing and the prepared IR Laser fault experimental runs from series A are visualized. For descriptions of the prepared bearings, please refer to section 5.3.
The measurements are exposed to little fluctuations over time. This is to be expected as the operating conditions are constant for the complete experiments. However, both the change of the sensor channel and the bearing class make the signals RMS differ. One very important thing to notice in figure 6.1 is that the IR Laser fault cannot consistently be distinguished from the Reference bearing for the 3 displayed sensor channels by setting a single RMS threshold. This gives a major first hint on the main challenge regarding transferability of fault diagnosis models.

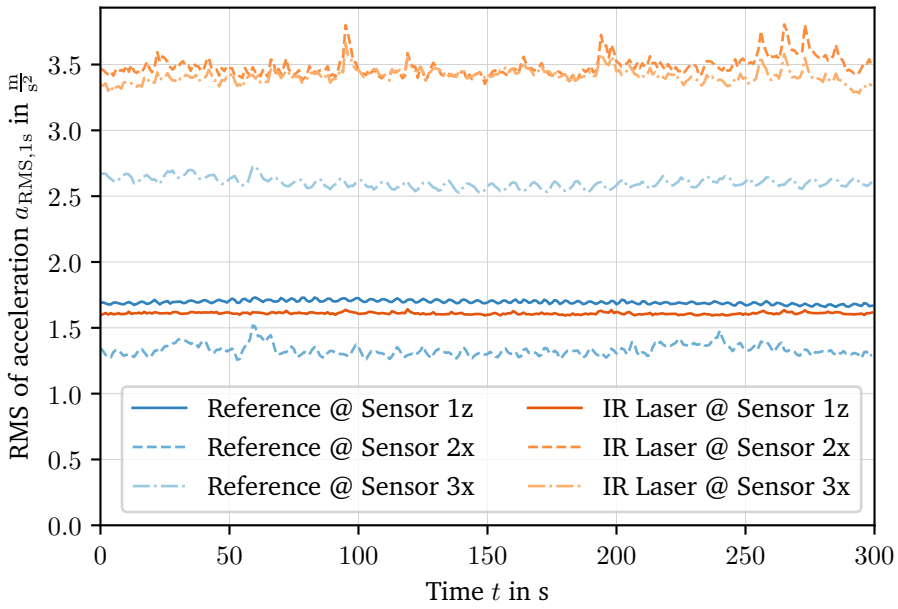

Figure 6.1.: RMS of acceleration for exemplary measurements from experimental series A.

To further expand the RMS-based analysis by using all sensor channels and experiments, figure 6.2 shows the RMS of the entire 300 seconds of measurement for each individual experimental run and each sensor channel.

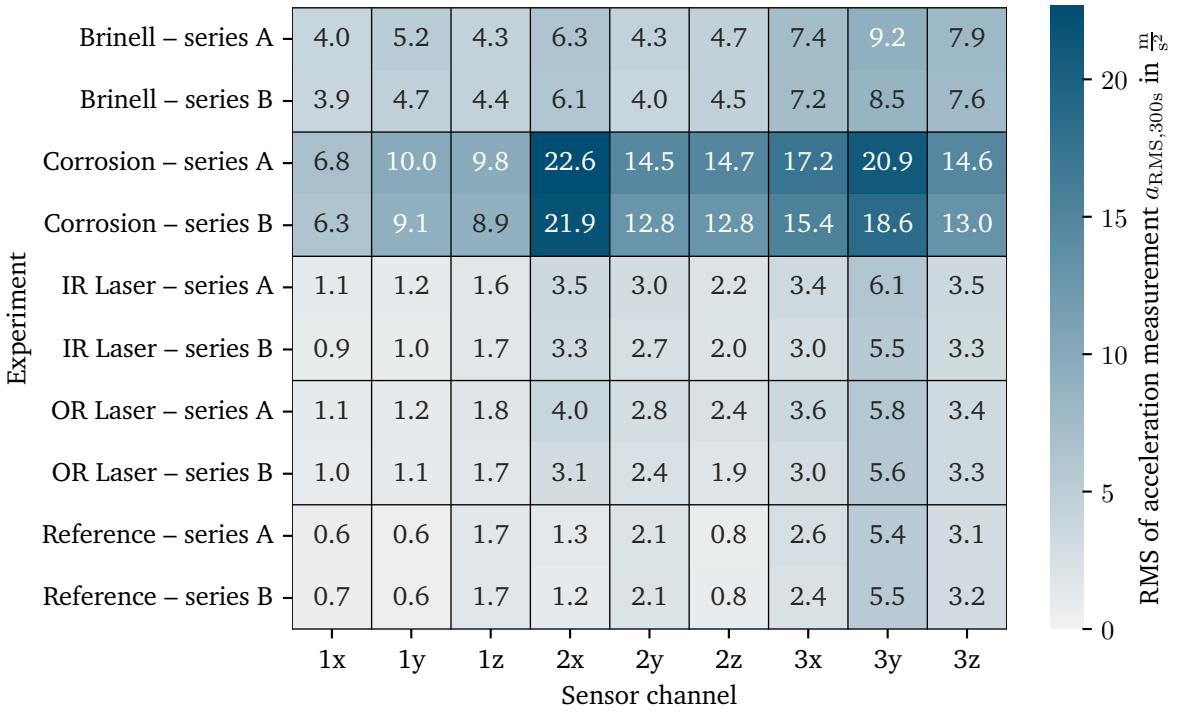

Figure 6.2.: Comparison of RMS values for each experiment and sensor channel.

Clear differences are visible, correlated to the different prepared bearings and to the sensor channels. Looking at the different bearings, the Corrosion fault causes the most powerful RMS values, followed by the Brinell fault. Both IR Laser and OR Laser faults show comparatively weak RMS values and thus, are very close to the Reference bearing. When comparing the two experimental series A and B, only slight differences are obtained. In general, the RMS values of experimental series B are slightly lower than those of experimental series A. This may be related to the additional 5 hours of run-in of each bearing at the beginning of the series B experimental runs, which presumably smoothes out the faults.
For further analysis within the subsequent paragraphs, data is plotted for single sensor channels and for every bearing fault individually. For the reason of compactness, only data excerpts from experimental series A are shown in detail. As a first time-domain visualization, figure 6.3 shows an exemplary excerpt of the OR Laser fault measurement in time-domain for sensor channel 2x. Therefore, the raw data is plotted alongside its envelope signal. The envelope signal is computed using the HT, the mathematical foundations of which are presented in section 4.3.4.

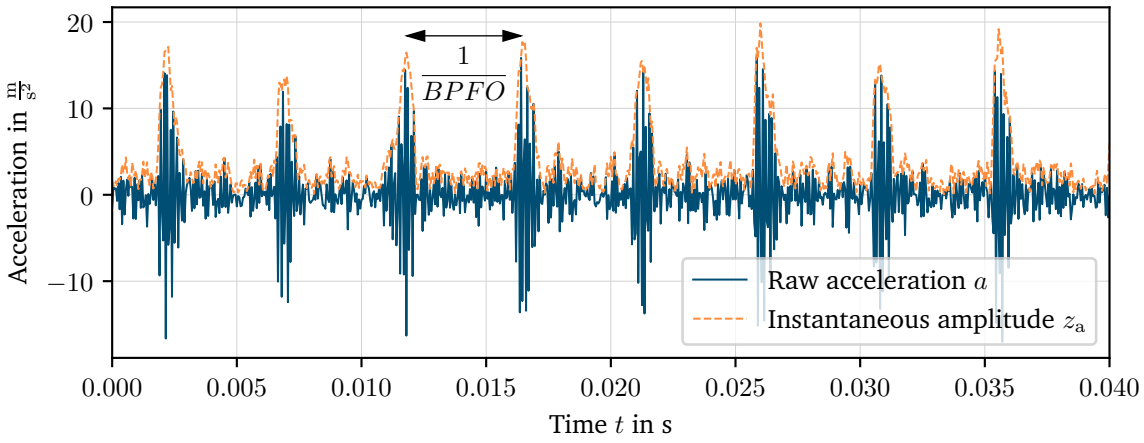

Figure 6.3.: Time-domain data and envelope signal for OR Laser fault from channel 2x.

As already described by Randall and Antoni [39], a local outer race fault within the load zone of the bearing leads to periodic force excitations. For a system with fixed outer ring and rotating inner ring, this periodic excitation has a regular behavior. In figure 6.3, the HT-based instantaneous amplitude provides an envelope of the raw acceleration signal and thus, visualizes the modulation of the acceleration amplitude. The rate of this modulation corresponds to the force excitation rate and is given by the fundamental frequency $BPFO$. For information on the fundamental frequencies, please refer to section 2.3.2.
To enable a more indepth analysis of the visualized data, the inner ring frequency as well as the fundamental frequencies are calculated for the given type 6207 bearing and summarized in table 6.1. The bearing dimensions necessary for the underlying calculations

can be found in the appendix at table B.2. The contact angle ϕ is dependent on the applied bearing forces and thus not specifically predetermined by geometry. Instead, it is derived to be $\phi = 13\ ^\circ$ by fitting the calculated fundamental frequencies to the measured excitation frequencies within the acquired acceleration data.

Table 6.1.: Fundamental frequencies of type 6207 deep groove ball bearing at inner ring speed $f_\mathrm{i} = 3500$ rpm.

	Frequency	**Period duration**	**Order of f_i**
f_i	58.3 Hz	17.15 ms	1
$BPFI$	315.6 Hz	3.17 ms	5.41
$BPFO$	209.4 Hz	4.78 ms	3.59
FTF	23.3 Hz	42.92 ms	0.40
BSF	134.7 Hz	7.42 ms	2.31

Knowing the calculated $BPFO$ and the corresponding period duration of 4.78 ms, this duration can be spotted in figure 6.3 as the distance between two maxima of the instantaneous amplitude.
For a further visualization, exactly the same time frame from figure 6.3 is used in figure 6.4 for time-frequency CWT visualization. For fundamentals on the CWT and an explanation of the main differences to the STFT, please refer to section 4.3.3. In the given case, a morlet wavelet is used to create this image representation.

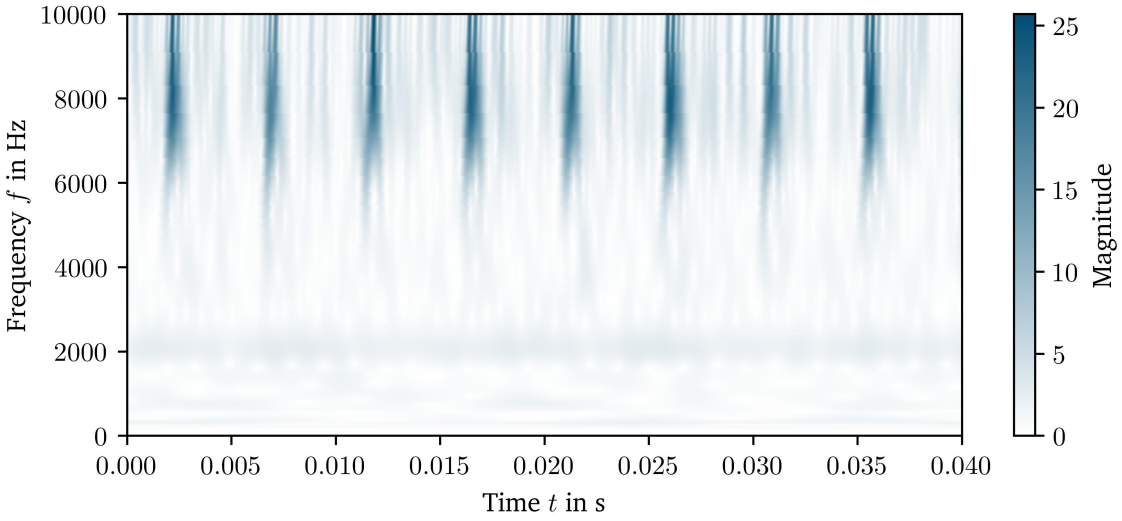

Figure 6.4.: CWT for OR Laser fault from channel 2x.

Again, the timings of the force excitations can be detected. Additionally, the acceleration response frequencies become visible at high frequency ranges around 6 to 10 kHz for the

given case. The 10 kHz upper limit is constrained by the measurement frequency of 20 kHz. Additionally, the low-pass anti-aliasing filter starts suppressing the amplitudes from 8 kHz on. Most probably, the structure is responding with even higher frequencies in the range above 10 kHz which cannot be detected here.
An additional visualization technique for traditional fault diagnosis is presented in figure 6.5. Here, the HT-based instantaneous amplitude, which was shown in figure 6.3, is transformed into frequency-domain via FFT, resulting in the envelope spectrum. In addition to the envelope's amplitude in frequency-domain, the orders of the inner ring frequency f_i as well as the orders of $BPFI$ and $BPFO$ are visualized as vertical lines.

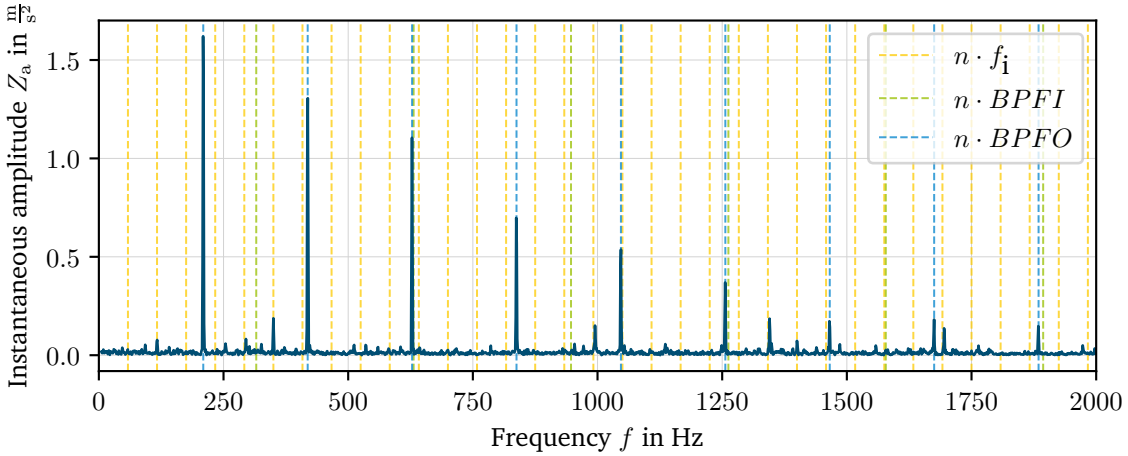

Figure 6.5.: Envelope spectrum for OR Laser fault from channel 2x.

It is apparent that the $BPFO$ and its higher orders are very dominant within the envelope signal of the OR Laser fault bearing. Thus, the outer race fault is well recognizable using the measurement data from channel 2x. In contrast, figure 6.6 shows the envelope spectrum of exactly the same moment in time, but from sensor channel 3x instead.

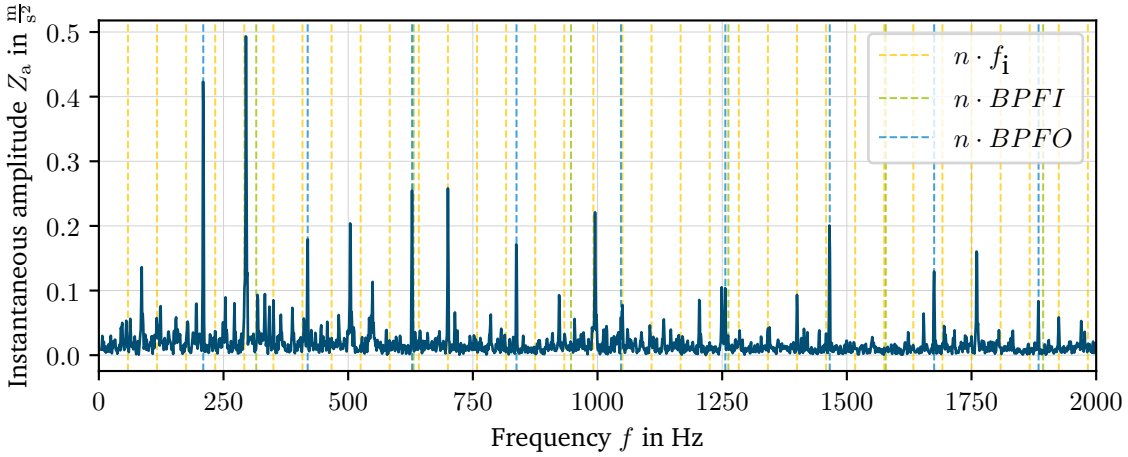

Figure 6.6.: Envelope spectrum for OR Laser fault from channel 3x.

In comparison to channel 2x, the $BPFO$ orders are less dominant for channel 3x which is why this fault cannot be identified as easily using traditional condition monitoring techniques. For channel 3x, some harmonics of the inner ring frequency f_i are much more present within the envelope spectrum. Apparently, the signal properties are strongly dependent on the sensor position. Due to reasons of compactness, not every channel is explored in detail within the present chapter. However, additional visualizations of the measurement data can be found in appendix C.
Moving back to channel 2x, next, data from the IR Laser fault is explored. Therefore, an excerpt of the acceleration measurement and its instantaneous amplitude are visualized in figure 6.7.

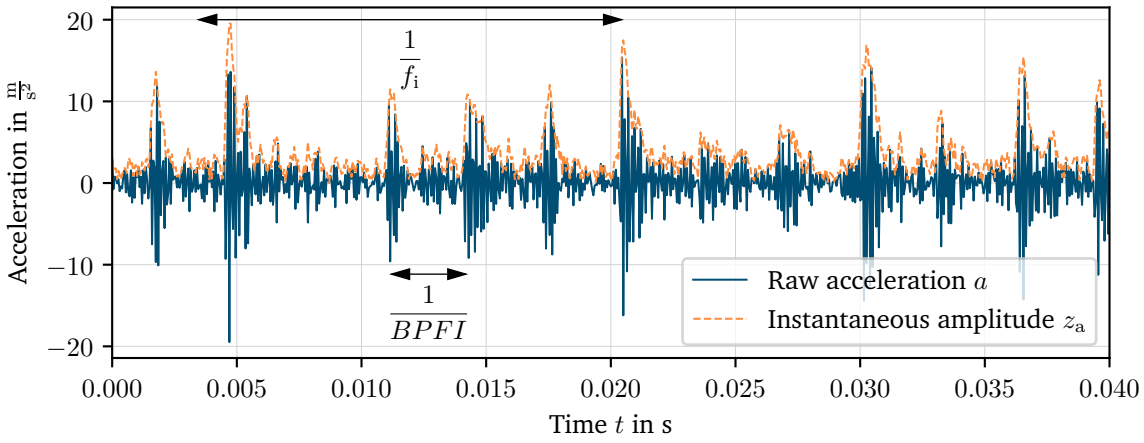

Figure 6.7.: Time-domain data and envelope signal for IR Laser fault from channel 2x.

According to Randall and Antoni [39], a single inner race fault leads to periodic excitations at the rate of the $BPFI$. With stationary outer ring and present radial bearing forces, this excitation is additionally modulated in its amplitude by the inner ring rotational frequency f_i. This effect is caused by the fault passing through the load zone. The roughly 3.17 ms period duration of $BPFI$ can be seen in figure 6.7 as the distance between two nearby excitations. Additionally, the amplitude modulation of the excitation can be assigned to the inner ring frequency f_i which is calculated to have a period duration of 17.15 ms, see table 6.1. Next, figure 6.8 provides the CWT representation of the IR Laser fault measurement.

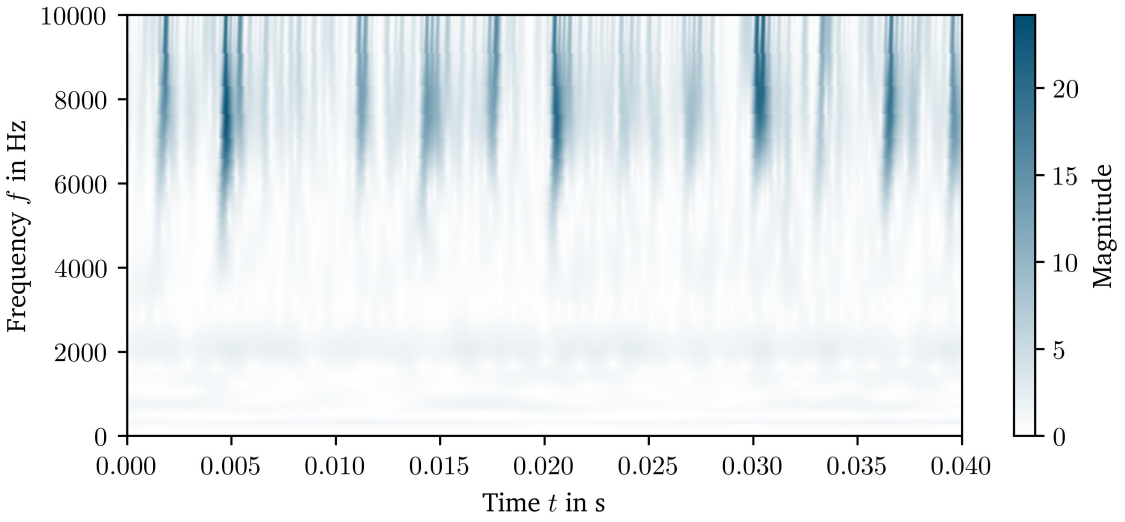

Figure 6.8.: CWT for IR Laser fault from channel 2x.

Again, the excitation events can be spotted in time. Similarly to the OR Laser fault, the frequency response is particularly present in the high frequency range inbetween 6 and 10 kHz for the IR Laser fault.
Taking a look at the envelope spectrum of the IR Laser fault in figure 6.9, the $BPFI$ and its higher orders are dominant.

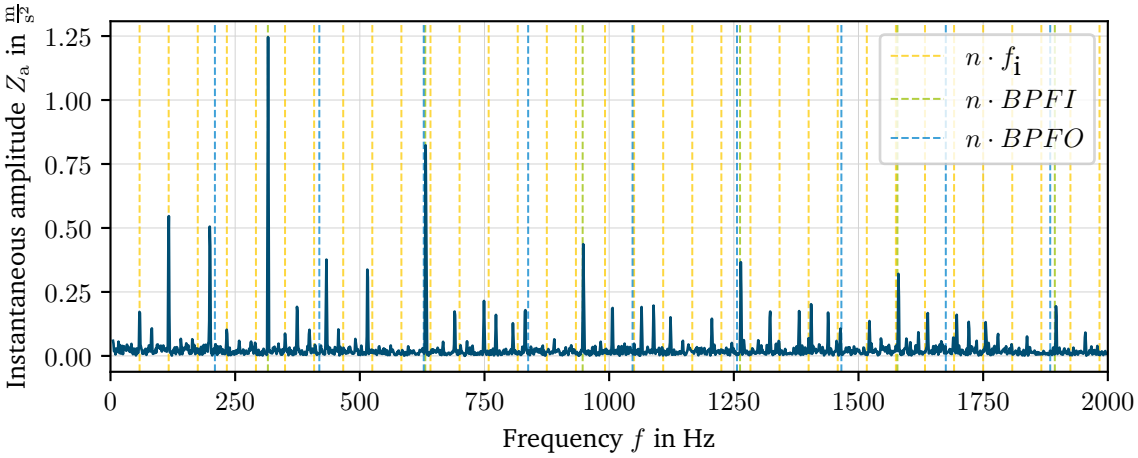

Figure 6.9.: Envelope spectrum for IR Laser fault from channel 2x.

This clear identifiability of the inner race fault is lost to a significant amount when taking a look at the same moment in time from channel 3x instead, visualized in figure 6.10.

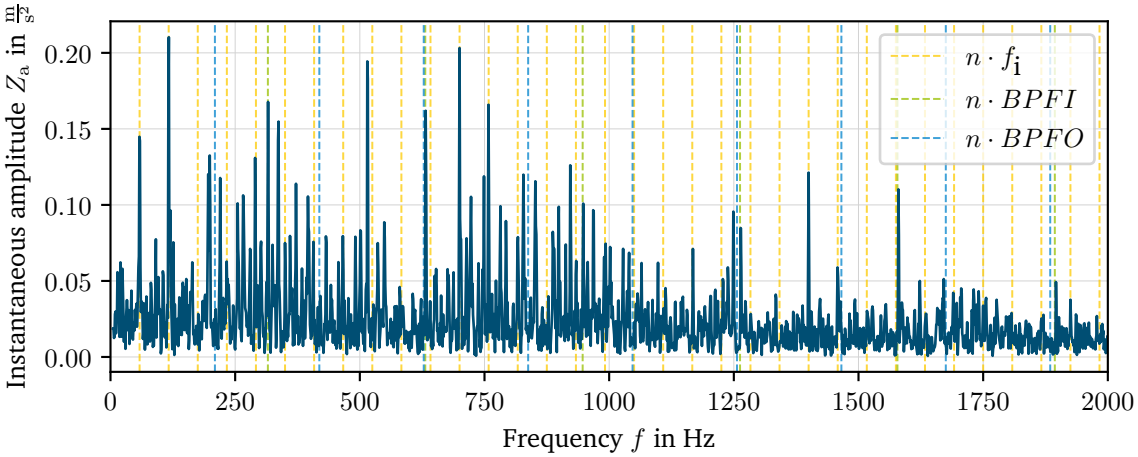

Figure 6.10.: Envelope spectrum for IR Laser fault from channel 3x.

This confirms the difference in signal properties for different sensor locations already noticed for the OR Laser fault. The less pronounced fault-indicating properties observed for sensor 3 can be explained by the larger distance between sensor and test bearing. The sensor placements have already been shown in figure 5.6. Additionally, the greater proximity of sensor 3 to the rotor of the PMSM might capture additional vibrations caused by the electromagnetic forces inside the PMSM.
To preserve the compactness of this work, only the envelope spectra are shown for the upcoming visualizations of Brinell, Corrosion and Reference bearings. Further CWT-based time-frequency-domain visualizations for these three bearings are presented in the appendix C within figures C.1 to C.3. Additionally, raw time-domain signals from each of the 9 sensor channels for all five bearings can be inspected within figures C.4 to C.12. Next, the Brinell fault is visualized in figure 6.11 by means of its envelope spectrum.

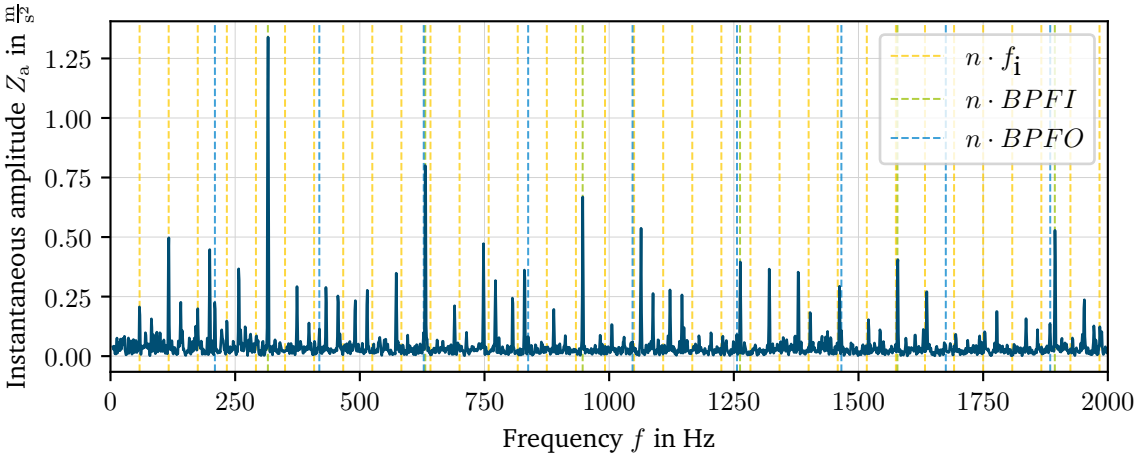

Figure 6.11.: Envelope spectrum for Brinell fault from channel 2x.

Looking at the fundamental frequencies, mainly the $BPFI$ and its higher orders domi-

nate. Thus, it can be concluded that the fault introduced is predominantly at the inner race. The less affected outer race can be explained by the different radii of curvature at inner and outer race, leading to higher contact stresses at the inner race during fault introduction and thus, to higher plastic deformations.
Figure 6.12 shows the envelope spectrum for the Corrosion fault, which has the highest amplitudes in comparison to the other bearing faults.

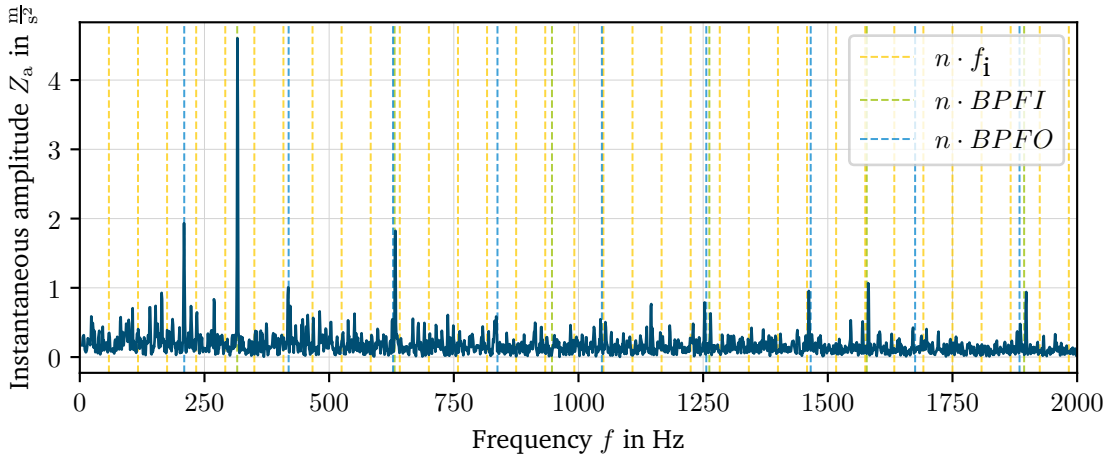

Figure 6.12.: Envelope spectrum for Corrosion fault from channel 2x.

Here, the first order of both $BPFI$ and $BPFO$ are dominant. This is reasonable as the Corrosion fault is present on the inner and outer races to a similar degree. Although this fault is introduced all over the raceways and balls, there are spots that are affected more severely by the corrosive surface alteration than others. This leads to the instantaneous amplitude revealing the outer and inner race fundamental frequencies.
Finally, the same kind of visualization is given for the Reference bearing in figure 6.13.

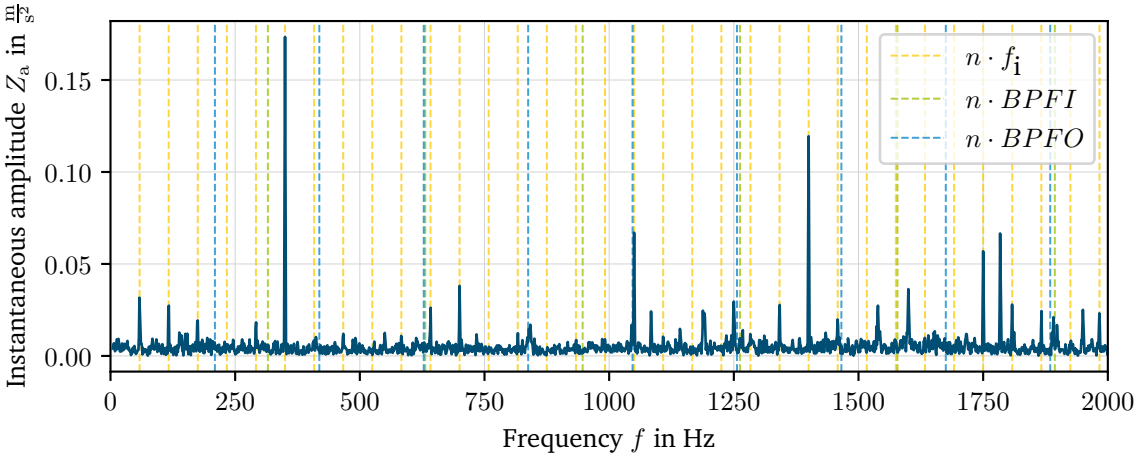

Figure 6.13.: Envelope spectrum for Reference bearing from channel 2x.

Neither $BPFI$ nor $BPFO$ are magnified within this envelope spectrum, which fits the non-existent fault. However, increased envelope amplitudes are noticeable which are fitting exactly to the sixth order of the inner ring speed f_{i} and its harmonics. This phenomenon of the dominant sixth order rotational frequency can be explained by the characteristic of the PMSM in use, having six pole pairs at the rotor. Thus, these frequencies can be attributed to electromagnetic force excitations caused by the topology of the PMSM.
To conclude the data exploration, bearing fundamental frequencies can be found in plausible coherence to each bearing fault when looking at data from sensor channel 2x. In comparison, the visualizations based on data from channel 3x are less suitable for fault identification. This sensor-dependent suitability of the data for traditional fault identification is caused by the different positions and orientations of the sensor channels. For the sake of compactness, only sensors 2x and 3x have been visualized within the present section. However, the differences in signal behavior extend to the remaining sensor channels in an analogous manner. This can be seen in more detail within the extended data visualizations provided in appendix C. Based upon the presented data, the following sections aim to evaluate the transferability of vibration-based fault diagnosis models to different sensor positions.

6.2. Procedure for Evaluation of Transferability

To evaluate the predictive performance in a transfer scenario to differing structural dynamics, a fixed procedure has to be specified. Therefore, the processing pipeline shown in figure 6.14 is set up and used as a framework.
The framework starts with the data collection, which was already described as part of chapter 5. Accordingly, the data already explored in the previous section 6.1 is used here. Next, the acceleration data is processed within the feature generation step. The complete measurements with a length of 300 seconds are split into 1 second intervals, each of which is used for feature calculation. These intervals of 1 second length ensure that at least 20 periods of even the lowest fundamental frequency $FTF = 23.3$ Hz are contained. The calculated values of all fundamental frequencies can be looked up in table 6.1. As part of the later investigations within section 6.3, different feature generation techniques are investigated with respect to the models predictive accuracy. Given the generated features, a train-test split is performed. This split is executed using different so-called transfer scenarios. These transfer scenarios are introduced in the context of figure 6.15 and thus elaborated in more detail within a subsequent paragraph.
To ensure suitable feature input ranges for the ML algorithms, feature scaling is generally recommended, see section 4.1.1. One common implementation of feature scaling is the standardization, which is also referred to as the calculation of the so-called Z-score. This technique scales the mean of the feature distribution to be 0 and its standard deviation to be 1 [92].
According to equation (6.1), the features split for training are used to fit a standard-scaler by calculating the mean $\mu(x_{i_{train}})$ and standard deviation $\sigma(x_{i_{train}})$. Next, the

features for both training and testing can be standardized by using the scaling rule defined from the training features. The standardized feature samples are denoted by $\tilde{x}_i$.

$$\tilde{x}_i = \frac{x_i - \mu(x_{i_{train}})}{\sigma(x_{i_{train}})} \tag{6.1}$$

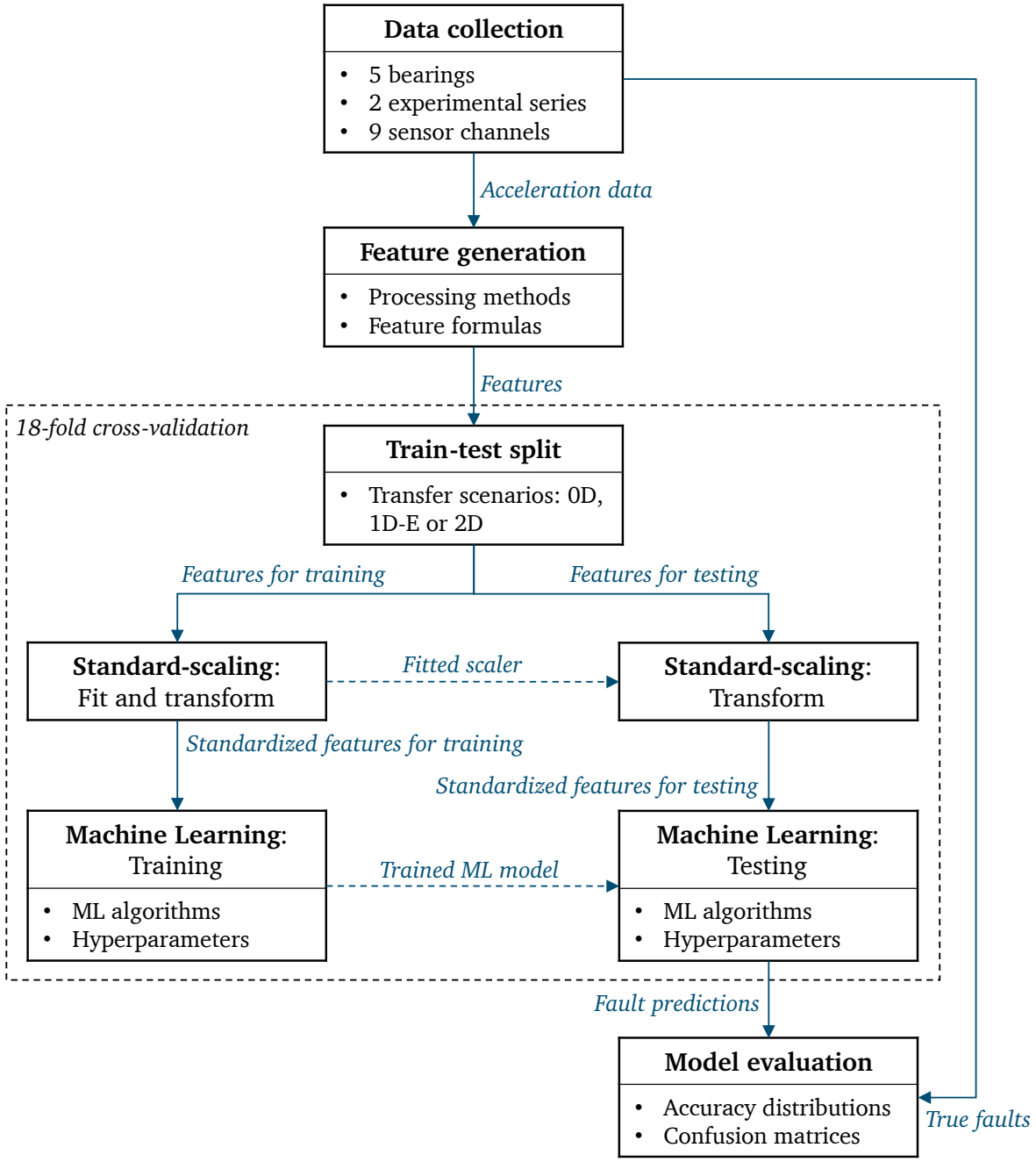

Figure 6.14.: Data processing framework for model evaluation.

After standardization, the training features are used to train the ML algorithm. Different

ML algorithms are investivated within the present chapter. To ensure well suited configurations of the algorithms in use, their hyperparameters are optimized in section 6.4. After training, the scaled features for testing are given to the trained ML algorithm to make predictions on the bearing faults. As a final step, the performance of the model can be evaluated using the fault predictions and the ground truth of the faults which is known from the data set. Since train-test splits are performed multiple times by making use of cross-validation techniques, the predictive accuracies can be evaluated statistically via their distributions. Furthermore, the predictions are analysed by utilizing confusion matrices.
The different transfer scenarios which are taken into account within the present work are categorized in figure 6.15. These scenarios represent different ways to split the data for training and testing. Two dimensions are introduced. On the one hand, a transfer to a different experimental series is investigated to evaluate the influence of the bearing removal and installation process on the predictive accuracy. On the other hand, the transfer to different sensor positions is investigated to address the Research Questions defined in section 3.2.

	Same experimental series	**Different experimental series**
Same sensor position	**0D**: No transfer	**1D-E**: Transfer to different experimental series
Different sensor position	**1D-S**: Transfer to different sensor position	**2D**: Transfer to different sensor position at different experimental series

Figure 6.15.: Assignment of different scenarios to the dimensions of transfer between training and testing.

Three of the four quadrants visualized in figure 6.15 are considered within this work. First, the 0D scenario without any transfer is used to generate a benchmark since this is the common way how fault diagnosis algorithms are evaluated in literature. For the 0D scenario, stratified train-test splits at ratios of 2/3 for training and 1/3 for testing data are performed using the same experimental series for training and testing. At this point, the term stratified refers to the proportions of all classes in the training and test sets being representative of the entire data set. Second, the 1D-E transfer to different experiments is compared to the 0D scenario to evaluate the influence of the bearing removal and installation process, which was described in section 5.4, on the predictions. As visualized in figure 6.16, the 1D-E transfer scenario to different experimental series is used to select a feature set as well as optimize the hyperparameters of the ML algorithms. Finally, the optimized models are evaluated by their transfer capabilities to different

structural dynamics using the 2D transfer scenario to a different sensor position from different experiments. The 1D-S scenario mentioned in figure 6.15 would not provide added value for this work, as it does not represent an application-relevant model transfer. Therefore, it is not considered any further here.
For both the 1D-E and 2D transfer scenarios, a cross-validation procedure is implemented by making use of the different sensor channels and the separate experimental series. This was already conceptually designed in section 5.1.2 and is now refined within figure 6.16. With the given 2 experimental series A and B, introduced in figure 5.11, and the $N_S = 9$ given sensor channels, a total of $2 \cdot 9 = 18$ cross-validation iterations can be performed. This 18-fold cross-validation involves training and testing 18 individual times for each setting to be examined.

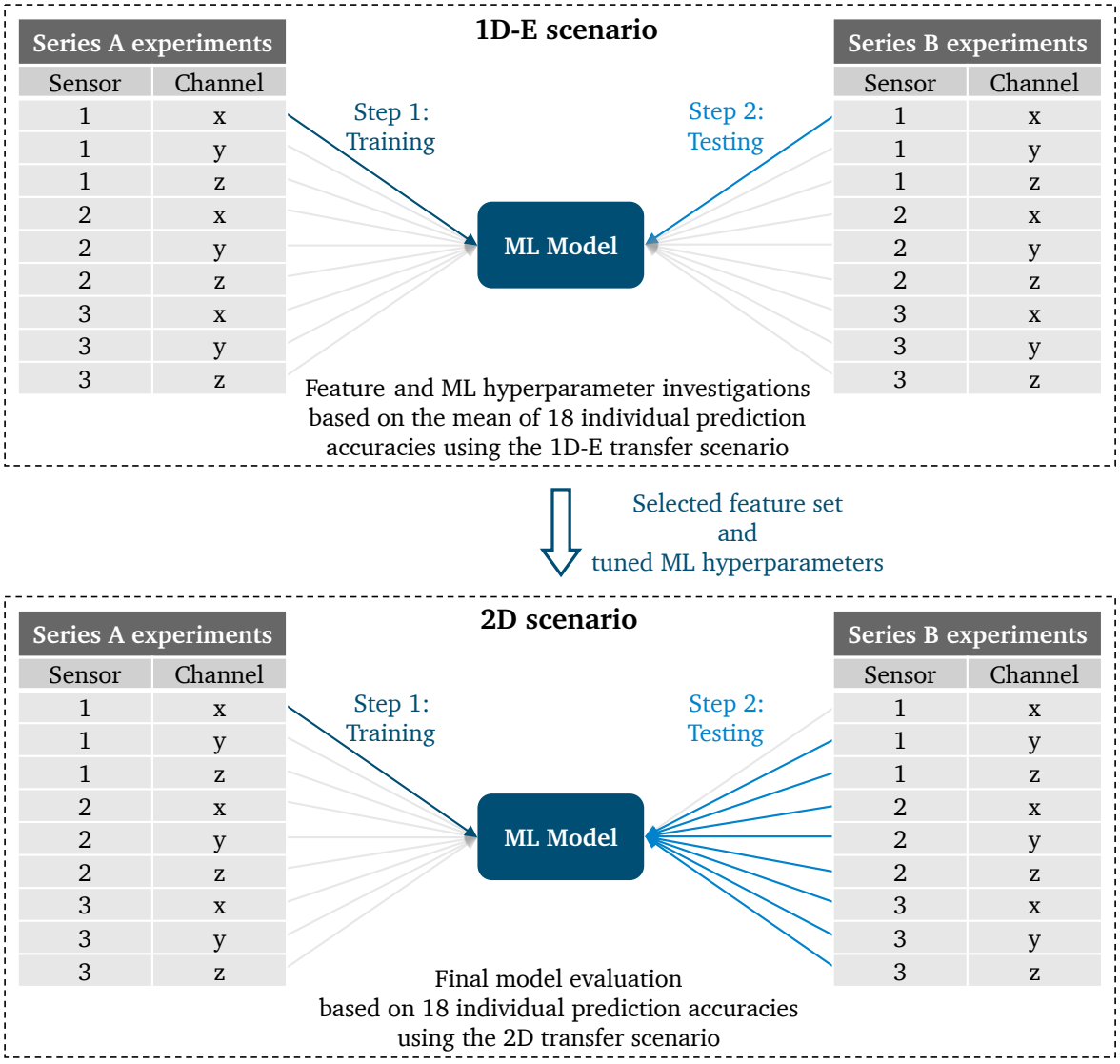

Figure 6.16.: Workflow incorporating the cross-validation procedure for model tuning with the 1D-E scenario and model evaluation with the 2D scenario.

To ensure an unbiased evaluation of the models' performances, the final evaluation must be carried out on testing data that was never given to the algorithm during the process of feature set selection or ML hyperparameter tuning. This is ensured by decoupling the 2D scenario from the 1D-E-based feature and hyperparameter investigations.
Within the following two sections, the procedure for feature set selection and ML hyperparameter tuning is described. For this purpose, section 6.3 presents feature engineering investigations first, using a predefined ML algorithm. Second, multiple ML algorithms are introduced and tuned with respect to their hyperparameters in section 6.4 to optimize their performances.

6.3. Investigations on Feature Engineering

A wide variety of techniques for feature engineering is summarized from the literature in chapter 4.2. In orientation to a prior publication of the present author [72], a selection of feature sets is created by combining signal processing methods and feature formulas. Therefore, the three main signal processing methods RAW, ENV and FB are introduced and presented in figure 6.17.

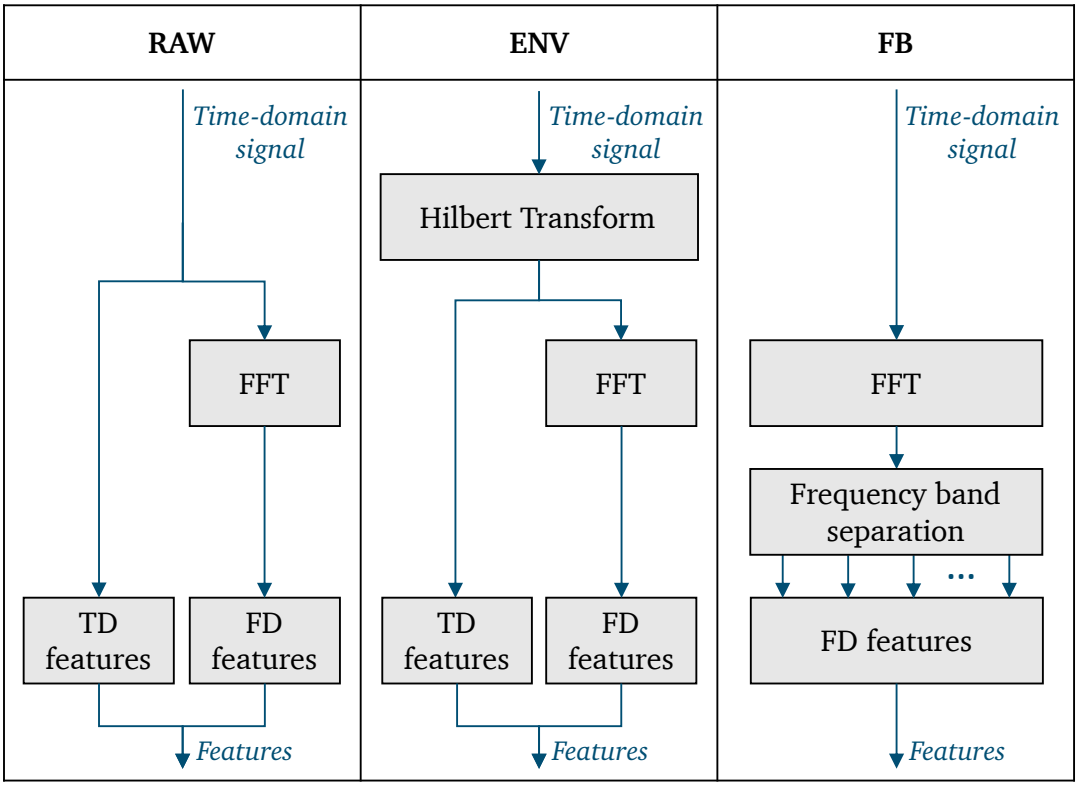

Figure 6.17.: Feature generation using different processing methods.

Building upon these 3 methods, different combinations of feature formulas are used for the feature engineering investigations. All investigated feature sets are listed in table 6.2 and described within the subsequent paragraphs.

Table 6.2.: Feature set explanations.

Feature Set Name	Processing Method	Feature Formulas	Complete Feature Count
RAW_TD	Raw signal	28 time-domain features: T_1 to T_{28}	28
RAW_FD	Raw signal	14 frequency-domain features: F_1 to F_{14}	14
RAW_Lei	Raw signal	25 features according to Lei et al.: T_1 to T_{11} and F_1 to F_{14}	25
RAW_all	Raw signal	All 42 features: T_1 to T_{28} and F_1 to F_{14}	42
ENV_Lei	Envelope signal	25 features according to Lei et al.: T_1 to T_{11} and F_1 to F_{14}	25
ENV_all	Envelope signal	All 42 features: T_1 to T_{28} and F_1 to F_{14}	42
FB4_FD	Frequency bands $N_{\mathrm{FB}} = 4$	14 frequency-domain features: F_1 to F_{14}	56
FB10_FD	Frequency bands $N_{\mathrm{FB}} = 10$	14 frequency-domain features: F_1 to F_{14}	140
FB25_FD	Frequency bands $N_{\mathrm{FB}} = 25$	14 frequency-domain features: F_1 to F_{14}	350
FB50_FD	Frequency bands $N_{\mathrm{FB}} = 50$	14 frequency-domain features: F_1 to F_{14}	700
FB50_FD-mean	Frequency bands $N_{\mathrm{FB}} = 50$	1 feature: Mean value in frequency domain: F_1	50
FB100_FD-mean	Frequency bands $N_{\mathrm{FB}} = 100$	1 feature: Mean value in frequency domain: F_1	100
FB250_FD-mean	Frequency bands $N_{\mathrm{FB}} = 250$	1 feature: Mean value in frequency domain: F_1	250
FB500_FD-mean	Frequency bands $N_{\mathrm{FB}} = 500$	1 feature: Mean value in frequency domain: F_1	500

For the calculation of the first four feature sets, the raw signal is used. Besides the feature sets calculated from time-domain (TD) and frequency-domain (FD) only, the feature set proposed by Lei [71] is used, combining both time- and frequency domain features. Additionally, the expanded feature set using all 42 feature formulas collected in tables 4.2 and 4.3 is used for comparison. To evaluate the impact of the envelope analysis for feature generation, the features proposed by Lei as well as all 42 features are applied to the HT-based envelope signal within two additional feature sets.
For the remaining eight feature sets, the focus is placed at the Frequency Band (FB) processing method, which was already introduced in section 4.3.1. Previous research of the present author on different data sets already found this processing method to work particularly well. This good performance was first shown on a Bosch data set acquired to enable a regression task [81]. Additionally, the publicly available CWRU data was used to compare a variety of different feature engineering methods on a classification task [72]. For implementing the FB processing method, the frequency-domain signal is divided into equally sized frequency bands, as already introduced in section 4.3.1. Here, the number of frequency bands N_{FB} are chosen in orientation to the preferred numbers of series proposed in DIN 323-1 [93]. Some deviations from DIN 323-1 are made to keep the discrete frequencies, in this case characterised by a resolution of 1 Hz and a range of up to 10 kHz, dividable by the number of frequency bands without remainders. The maximum count of features is limited to 700 in order to constrain computational effort. Two different sets of feature formulas are investigated for the FB method. On the one hand, all FD features are used. On the other hand, only the mean value in frequency-domain (FD-mean) is calculated for every frequency band.
Using the CWRU bearing fault data for feature engineering investigations in [81], feature reduction techniques could not lead to increased prediction accuracies. For this reason, and to avoid additional process complexity, no feature reduction is applied within the present work. Instead, the complete feature sets, as defined in table 6.2, are compared with respect to their ML-based prediction accuracies.
The selection of the best suited feature set and the hyperparameter tuning of multiple ML algorithms are performed in sequential order due to limited computing capacities. For reasons of comparability, all ML algorithms are to be trained and tested using the same feature set. Although it cannot be guaranteed that the selected feature set works in an optimal way for all of the different ML algorithms, the later shown results present their good performances in comparison, see section 6.5. To select a feature set, a single reference ML algorithm has to be specified for comparing the already defined feature sets. A RF algorithm is selected for this purpose because it is known for its good performance when using default hyperparameters without elaborate tuning [82]. For fundamentals on the RF, please refer to section 4.1.1. According to Breiman [94], RFs are by design not subject to the problem of overfitting due to the law of large numbers. This makes them particularly well suited for the present application. For the feature set investigations, the RF is parameterized with a number of DT estimators $n\_estimators = 500$ and a maximum tree depth $max\_depth = 20$. All further hyperparameters remain to be the default values as given by the *Python* software package *scikit-learn*. All software packages and their version numbers in use are listed in the appendix at table B.3.

The performances of the different feature sets in terms of their mean prediction accuracies resulting from the classification of the $N_C = 5$ bearing classes is shown in figure 6.18. Here, each feature set is evaluated based on the three different transfer scenarios 0D, 1D-E and 2D.

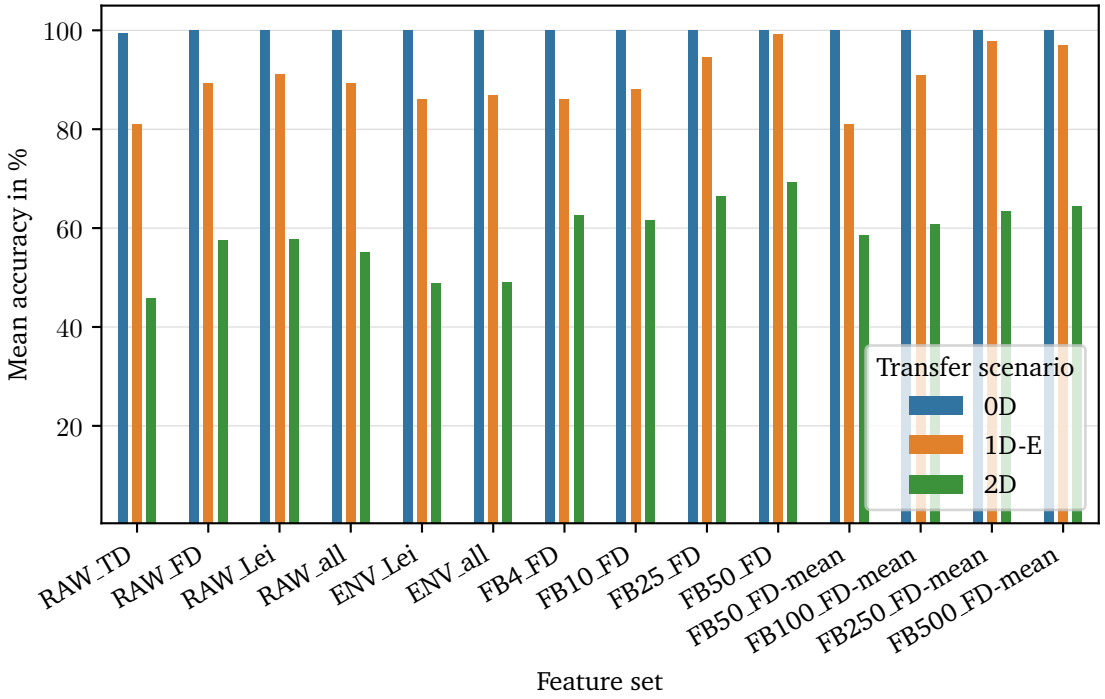

Figure 6.18.: Bar plot of mean predictive accuracies comparing the different feature sets; with baseline RF.

First, lets take a look at the 0D scenario, visualized in blue. Almost all of the feature sets enable the RF to achieve a perfect accuracy of 100 %. Only the RAW_TD feature set falls very slightly behind with a mean accuracy of 99.5 %. All numerical values represented in figure 6.18 can be looked up in the appendix at table D.1. The overall very high accuracy of the 0D scenario shows the simplicity of this classification task. Since a simple train-test split is performed based on the same experiments, it cannot be ensured that the bearing fault itself is detected by the algorithm. Instead, unknown influencing factors may have changed inbetween the experimental runs which may lead to their separability. These changes can for example be caused by the disassembly and reassembly of the e-machine, potentially effecting joint stiffnesses of the screw connections and thus, changing the structural dynamics of the system.
To overcome the ambiguity about the cause leading to the data being distinguishable in the 0D scenario, the 1D-E scenario was introduced in the context of figure 6.15. Here, training and testing are performed on two completely separated experimental series to ensure the detection of the actual bearing fault. The classification accuracies visualized in figure 6.18 show that the bearing faults are much harder to predict in the 1D-E scenario

in comparison to the 0D scenario. Taking a look at the orange bars, the mean accuracies vary inbetween the different feature sets. Thus, their comparitive evaluation is enabled. Besides comparing the mean of the cross-validation accuracies in figure 6.18, figure 6.19 additionally shows each single of the 18 cross-validation iterations as a point within a boxplot to visualize the corresponding accuracy distributions. As already presented in the context of figure 6.16, each of the 18 individual iterations within cross-validation represents the procedure of ML training on one of the 9 sensor channels, using the data from one of the two experimental series, and the evaluation of the trained model on the testing data from the same sensor channel, but from the second experimental series.

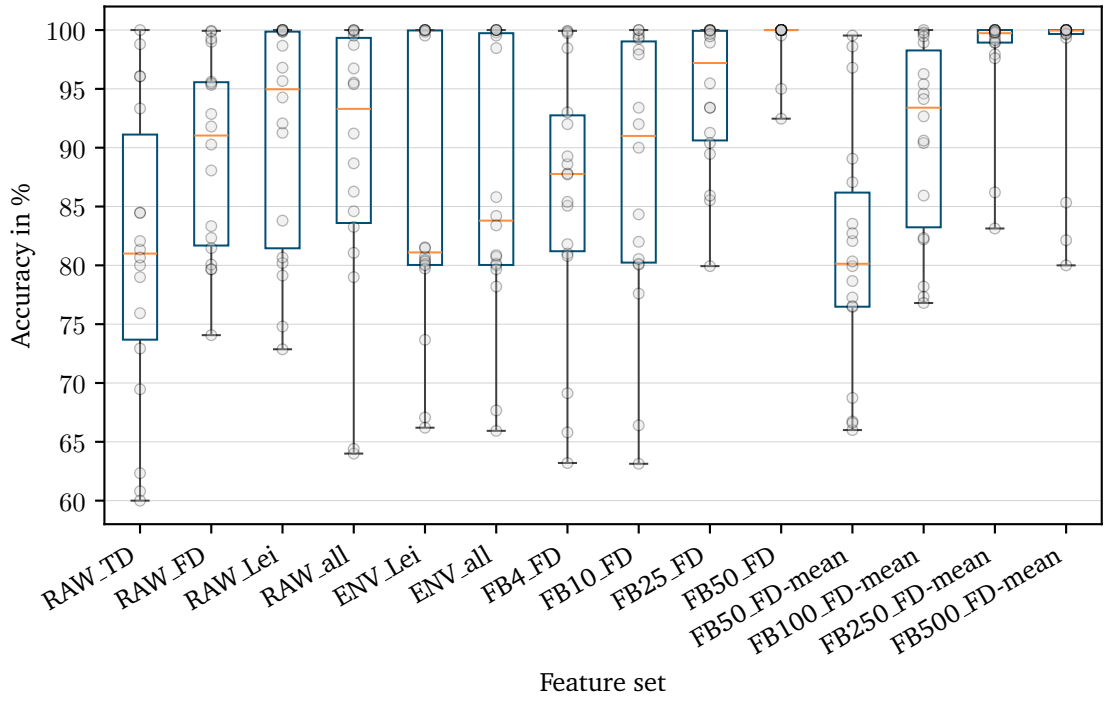

Figure 6.19.: Box plot of predictive accuracies comparing the different feature sets using the 1D-E scenario; with baseline RF.

The box plot in figure 6.19 visualizes the accuracies of the single points by subdividing their distributions into quarters:

- The middle line (here: orange) represents the median of the underlying distribution.
- The rectangle (here: blue) around the median visualizes the range inbetween the first and third quartile.
- The whiskers (here: dark gray) start at the minimum and end at the maximum value of the distribution.

Starting the in-depth result analysis with the raw signal-based feature sets (RAW), the frequency-domain RAW_FD features perform better than the time-domain RAW_TD features. Combining both domains in RAW_Lei and RAW_all leads to even better results. However, adding additional Features in comparison to the features proposed by Lei et al. [70, 71] cannot improve the accuracy any further. This finding is in agreement with the results presented in [72].
Using the HT to preprocess the signal for the envelope based feature sets ENV_Lei and ENV_all leads to slight deteriorations of the mean accuracy and thus, is not recommendable here.
The FB method with an increasing number of frequency bands can significantly increase the prediction accuracies. Using 50 frequency bands and all 14 frequency-domain features in the FB50_FD feature set enables the first quartile of the cross-validation to be at 100 % accuracy. The corresponding mean accuracy equals 99.3 %, which is the best result achieved within these feature set investigations. Besides calculating all FD features, the four feature sets shown on the right of figures 6.18 and 6.19 use only the FD-mean feature formula for every single frequency band. It can be seen that further increased frequency resolution induced by the larger number of frequency bands can increase prediction accuracies, but does not outperform the FB50_FD feature set which uses all FD features with a smaller number of frequency bands.
A more indepth look at figure 6.18 allows for the comparison between the prediction accuracies of the 1D-E scenario and the 2D scenario. It can be seen that all 2D scenario-based results are worse than using the 1D-E scenario. This is to be expected due to the added sensor channel transfer dimension. Nevertheless, the trends regarding feature set performances in the 1D-E and 2D scenarios correlate very well.
Overall, it is shown for both the 0D and the 1D-E scenarios that, with a sufficiently sophisticated feature set, a correct classification of almost all data samples is achieved. However, as presented in section 6.1 and appendix C, depending on the sensor channel, some of the faults are not easy to identify when examining the data visually. Accordingly, the superiority of a data-driven fault diagnosis approach in comparison to purely human-based fault detection becomes apparent.
For further investigations in the upcoming sections, the FB50_FD feature set is selected due to its overall excellent performance within the previously presented feature set comparison. The now following section 6.4 focuses on the use of further ML algorithms and the optimization of their hyperparameters.

6.4. Hyperparameter Optimizations for Multiple ML Algorithms

After feature generation, the feature data is available in tabular format. As already visualized in figure 6.14, the next steps are to perform a train-test split, standardize each feature distribution and apply an ML algorihm for training and testing. In the given case of bearing fault diagnosis, five different classes are to be distinguished, each

corresponding to a single prepared bearing. Accordingly, the ML task is categorized to be supervised learning via multiclass-classification. As already presented in section 4.1.1, a wide variety of ML algorithms for multiclass-classification exists. A selection has to be made for the further investigations. However, using multiple ML algorithms later on allows for insights on the general applicability of the methods developed in this work.
For the present fault diagnosis case, the main challenge for the algorithm is to be transferable to different experimental runs and sensor positions. Thus, the most important requirement for the ML algorithm is to generalize very well. With generalization as main selection criterion, the four algorithms k-NN, RF, ANN and SVM are chosen on the basis of the considerations presented in section 4.1.1.
As already introduced in section 4.1.2, the hyperparameters of ML algorithms can be tuned to configure their architectures and thus their overall learning behaviors. Tuning these hyperparameters can considerably influence the performance of the final model. Therefore, they have to be adjusted to the present task. An established approach for tuning the hyperparameters of ML models in order to achieve optimal performances on a given task is to use Bayesian Optimization (BO). For the present work, the BO-TPE optimization algorithm is applied, the procedure of which was already explained within section 4.1.2.
For implementation of the BO-TPE hyperparameter optimization, this work makes use of the *Python* software package *hyperopt* [95]. For the ML algorithms, the implementations provided by *scikit-learn* are used. For an overview on the software versions in use, please refer to table B.3 in the appendix. The hyperparameters to be optimized in the present work are selected based on the overview on hyperparameter optimization given by Yang and Shami [66, p.310]. Table 6.3 presents the selected hyperparameters to be optimized, their search spaces as well as their final values resulting from the optimization process.
As described within figure 6.16, the hyperparameter optimization is performed using the 1D-E scenario. The objective of this hyperparameter optimization is the maximization of the mean accuracy from the cross-validation procedure. Within the feature engineering investigations already presented in section 6.3, the FB50_FD feature set shows the best performance and therefore is used for the final answering of Research Questions 1 and 3. However, since the mean prediction accuracy with the FB50_FD feature set and baseline RF already reaches 99.3 %, there is very little headroom left for hyperparameter optimization. To generate a larger headroom, the less well performing feature set FB10_FD is used for this purpose. At this point, it is assumed that the results of the hyperparameter optimization are approximately valid for the larger FB50_FD feature set as well. For each of the four ML algorithms, the BO-TPE optimization process is carried out for 500 iterative evaluations. As results, the best-performing ML hyperparameter configurations are given by the final values described in table 6.3.

Table 6.3.: Configuration spaces for hyperparameter optimization and the final, configured values.

	Hyperparameter	Type	Search space	Final value
***k*-NN**	*n_neighbors*	Discrete	[5, 300]	186
	weights	Categorical	["uniform", "distance"]	"uniform"
	p	Continuous	[1, 2]	1.9
RF	*n_estimators*	Discrete	[100, 1000]	135
	max_depth	Discrete	[1, 20]	13
	min_samples_leaf	Discrete	[1, 50]	24
	max_features	Continuous	(0, 1]	0.415
	max_samples	Continuous	(0, 1]	0.104
ANN	*hidden_layer_1_size*	Discrete	[10, 200]	58
	hidden_layer_2_size	Discrete	[10, 200]	149
	hidden_layer_3_size	Discrete	[10, 200]	178
	activation	Categorical	["tanh", "relu"]	"tanh"
	alpha	Continuous	[1e-3, 1e3]	0.0578
SVM	*C*	Continuous	[1e-2, 1e3]	172
	gamma	Continuous	[1e-8, 1e-3]	1.79e-7

The next section 6.5 aims to evaluate the transferability of vibration-based fault diagnosis models according to Research Question 1. For this purpose, the optimized ML hyperparameters are used in combination with the best-performing FB50_FD feature set.

6.5. Evaluation of Transferability

In a similar fashion to the feature engineering investigations already presented in figure 6.19, the predictive performance is now evaluated using the accuracy distributions of the 18-fold cross-validations. Figure 6.20 on the one hand shows the accuracies of the 1D-E scenario, based on which the feature set and hyperparameters were chosen. On the other hand, the performance for the 2D scenario is presented for comparison.

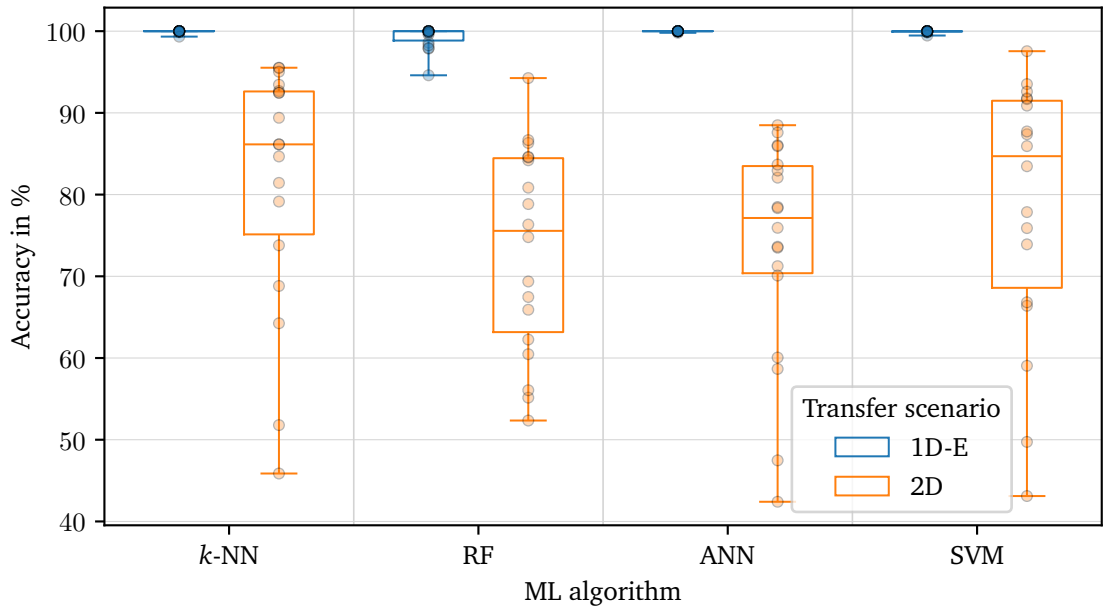

Figure 6.20.: Box plot of predictive accuracies comparing the transfer scenarios 1D-E and 2D using acceleration data; with FB50_FD feature set and optimized hyperparameters.

All four presented ML algorithms clearly depict a large performance difference inbetween the 1D-E and 2D scenarios. To supplement figure 6.20, table 6.4 provides the mean values of the prediction accuracies.

Table 6.4.: Mean accuracy comparison between the transfer scenarios 1D-E and 2D using acceleration data; with FB50_FD feature set and optimized hyperparameters.

	Mean accuracies	
ML algorithm	1D-E scenario	2D scenario
k-NN	100.0 %	81.6 %
RF	99.3 %	73.4 %
ANN	100.0 %	73.7 %
SVM	99.9 %	78.6 %

Both figure 6.20 and table 6.4 clearly show that transfering the trained ML algorithms to a differing sensor position and thus, changing the acoustic transmission path inbetween bearing and sensor, leads to significant losses in predictive accuracy. Comparing the four different ML algorithms among each other, the accuracy results only differ slightly. Taking an exemplary look at the ANN, perfect predictions without any misclassifications

are achieved for the 1D scenario. In contrast, for the 2D scenario, about one quarter of all predictions are misclassified.
For further analysis, the allocation of incorrect classifications is visualized using confusion matrices. Since the four ML algorithms show qualitatively similar results, the SVM algorithm is selected representatively for confusion matrix visualizations due to its consistently good performance within this entire work and its very fast classification time, see table 4.1, which make it suitable for industrial applications. The results for the 1D scenario in figure 6.21 and the 2D-E scenario in figure 6.22 can be examined in comparison.

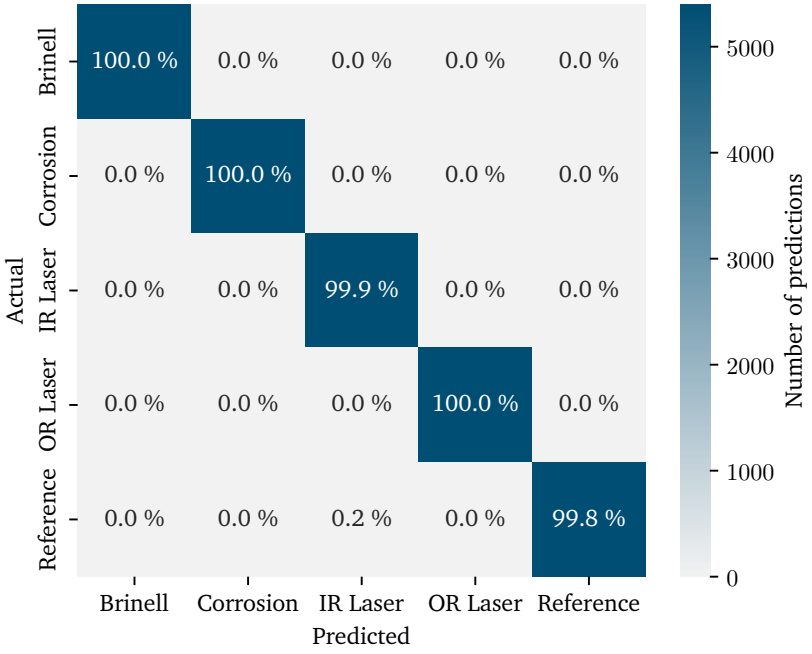

Figure 6.21.: Confusion matrix for the 1D-E scenario using acceleration data; with FB50_FD feature set and hyperparameter-optimized SVM classifier.

Taking a look at the confusion matrix of the 1D-E scenario, 5400 predictions are evaluated per bearing class. This number results from the 18-fold cross-validation, each using 300 samples per class for testing. Here, almost all predictions are made on the correct classes corresponding to the diagonal of the matrix. Only very few missclassifications are present for the Reference and IR Laser classes.
In contrast to the 1D-E scenario visualized in figure 6.21, figure 6.22 shows a lot more incorrect predictions for the 2D scenario. For the 2D transfer scenario, 43200 predictions on the testing data are evaluated per bearing class. This number is eight times higher in comparison to the 1D scenario due to the eight sensor channels used for testing, see figure 6.16.

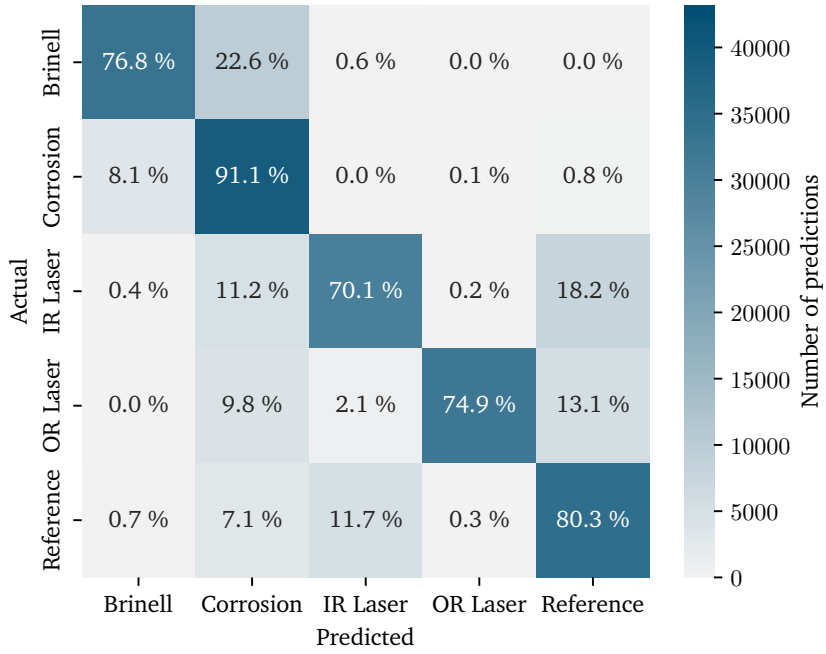

Figure 6.22.: Confusion matrix for the 2D scenario using acceleration data; with FB50_FD feature set and hyperparameter-optimized SVM classifier.

Looking at the confusion matrix of the 2D scenario, the Corrosion fault is classified correctly with the highest rate of 91.1 %. This advantage over the other classes can be explained by the high severity of the Corrosion fault in comparison to the other faults, which makes it easier to identify. For the remaining bearings, a smaller proportion of predictions are correct. In particular, the IR Laser and OR Laser classes show high rates of missclassification to the Reference bearing. This seems to be reasonable, as it was already shown in figure 6.2 that the IR Laser and OR Laser faults only generate slightly pronounced vibrations. Thus, their vibration measurements are close to the measurements obtained with the Reference bearing.
In general, the confusions are widely spread inbetween all classes. It can be observed that the confusions are not quite symmetrical to the diagonal. Accordingly, some faults are more likely to be identified than others. Overall, the observations presented in the two confusion matrices underline the already in figure 6.20 presented loss in predictive accuracy when moving from the 1D to the 2D-E scenario.
To answer Research Question 1 in a conclusive way, the mean prediction accuracy for the given investigations gets reduced from approximately 100 % to around 80 % as shown in table 6.4. The exact loss in accuracy slightly depends on the ML algorithm in use. As demonstrated, the acceleration-based fault diagnosis models are not well suited for a transfer to a different sensor position, representing a change of the structural dynamic properties. With the aim of overcoming this shortcoming in terms of transferability, the next chapter proposes extended methodological concepts for bearing fault diagnosis.

7. Model Extension Involving Domain Knowledge

The previous chapter demonstrated that transferring a vibration-based ML model for fault diagnosis to a different sensor position leads to a significant reduction of its predictive accuracy. It is therefore concluded that, given the current state of research, a transfer of this kind is not recommended. Instead, a new ML-based fault diagnosis model needs to be created based on new training data for every single structural dynamics behavior. In particular, the training data has to incorporate all possible conditions which are to be predicted from the operating data later on. The more complex the requirements for the fault diagnosis model are, the more effort is required to collect the necessary training data.
Section 6.1 explored that the different transmission paths between the bearing and the different sensors cause the measured signals to have different properties. Now, with regard to Research Question 2, the goal of the current chapter is to develop methodological concepts that overcome the limitations imposed by different transmission paths. To address this goal within the subsequent sections, two distinct conceptual approaches[1] are proposed which incorporate knowledge of structure-borne sound propagation. The main idea behind the newly proposed approaches is to enable the transferability of the ML-based fault diagnosis model by incorporating an additional calibration step into the chain of data processing. By introducing additional calibration data, whose acquisition is aspired to be considerably less expensive in comparison to the original training data acquisition, domain knowledge is contributed to the model. The underlying concept is presented schematically in figure 7.1.

[1] Both of the two novel approaches introduced within the present chapter were filed as individual patent applications at the German Patent and Trade Mark Office (DPMA):

- Approach 1: DPMA application number 10 2022 213 123.1
- Approach 2: DPMA application number 10 2023 213 129.3

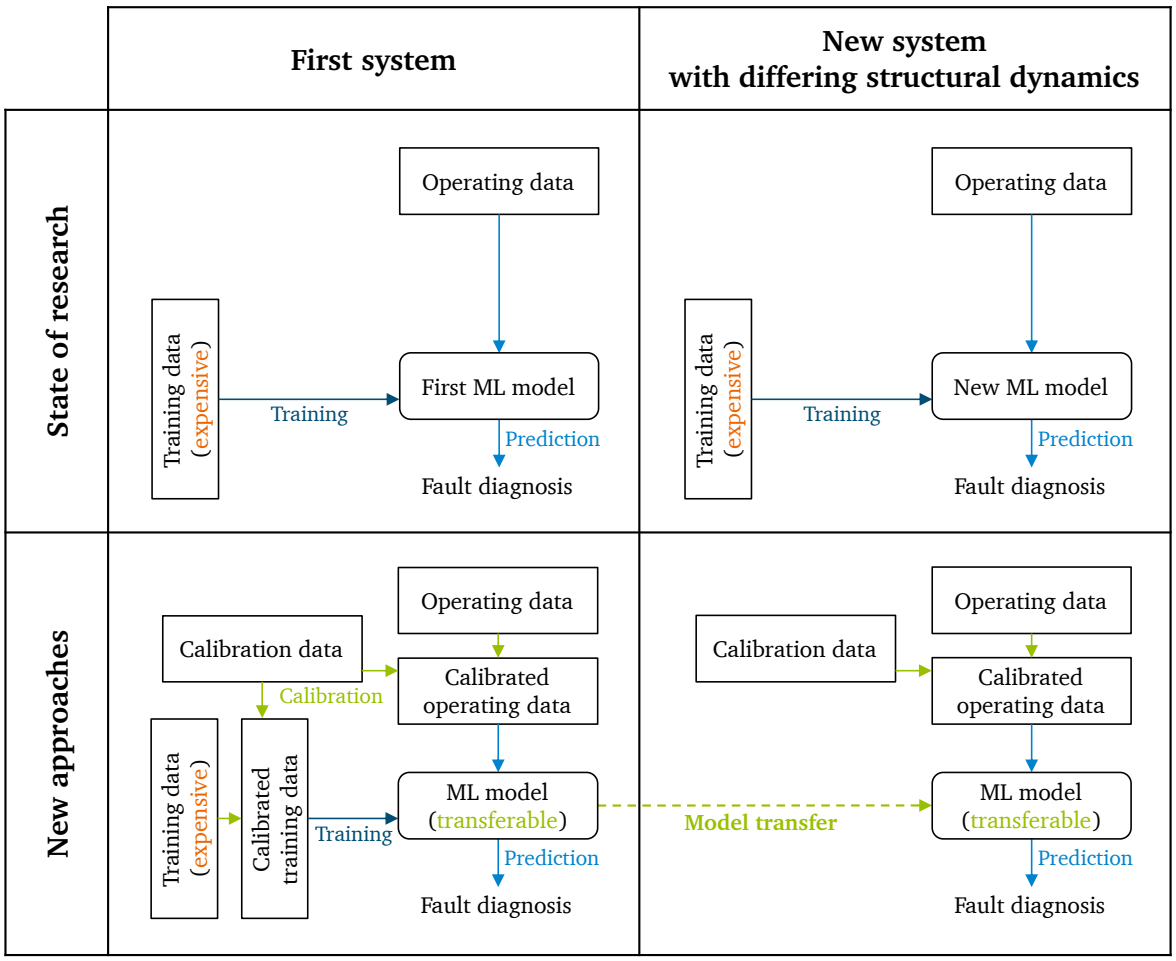

Figure 7.1.: Conceptual approach to improve transferability in comparison to the state of research.

As conceptualized, in comparison to the state of research, the new approaches aim to avoid the necessity of additional, time-intense and expensive training data acquisition for every new system with different structural dynamics. To achieve this, the comparatively little additional effort of acquiring calibration data is tolerated. Based upon this general concept, two new approaches are presented in detail within the following sections 7.1 and 7.2.

7.1. Approach 1: Virtual Forces

To exclude the influence of differing structural dynamic properties using domain knowledge, Approach 1 aims to calculate virtual, dynamic excitation forces at the bearing – from here on shortly referred to as virtual forces. To achieve this, measured Frequency Response Functions (FRFs) are used to calibrate the frequency domain data. The basic idea of this approach can be shown with the help of figure 7.2.

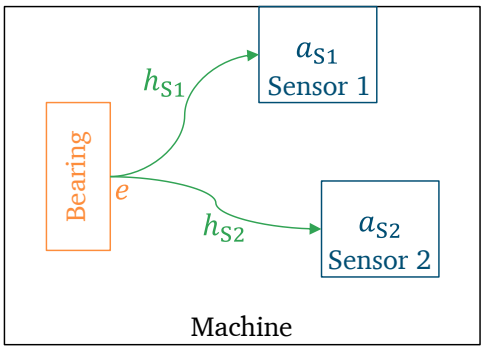

Figure 7.2.: Schematic visualization of FRFs.

During machine operation, the bearing fault dependent dynamic force excitation e leads to accelerations a at the sensor positions. As already presented in section 6.1, the acceleration differs for each sensor channel. Referring to the fundamentals on structure-borne sound, introduced in section 4.4, this can be explained by the differing transmission paths as part of the structure-borne sound propagation inbetween the bearing and the different sensor positions. As presented in section 4.4.1, the FRF of a transmission path can be described by its accelerance h.
For the virtual force approach, the key idea is to calculate virtual forces v as approximates of the actual bearing force e by using knowledge of the sensors' accelerations a and the corresponding accelerances h. Therefore, each accelerance inbetween the bearing and the different sensor channels has to be determined.

7.1.1. Determination of Frequency Response Functions

Building upon equation (4.15), the virtual forces are calculated using the known acceleration measurements and additional measurements of the FRFs in terms of their accelerances. The accelerance measurements are performed using the impulse hammer method, already introduced in section 4.4.2.
It is worth mentioning that several preliminary attempts have been performed to carry out these impulse hammer-based measurements using different experimental approaches. This involves experimenting with different points of excitation next to the bearing's raceways, which could only be realized to a limited extend due to space constraints. Additionally, reciprocal measurements are performed, for which the locations of the force excitations and vibration measurements are reversed. In these preliminary tests, the reciprocal measurements offer advantages in terms of realizability and reproducibility. For these reasons, reciprocal accelerance measurements are presented in detail below and subsequently used to calculate the virtual forces.
Most mechanical systems in reality are naturally subject to a certain degree of non-linearity with respect to their structural dynamics [63, p.322]. However, a reciprocal measurement is based on the assumption of linear system behavior [96]. For the presented case, using the e-machine test bench, this linearity cannot be clearly validated due to experimental space constraints. Here, the assumption of linear frequency re-

sponse functions is expected to be valid only to a limited extent because of the complex structural design of the e-machine including several joints, which may cause frictional energy dissipation. Thus, the final results of the virtual force approach may be affected by these uncertainties in determining the accelerances.
The experimental setup for acquiring the FRF measurements for the later presented virtual force calculations is shown in figure 7.3.

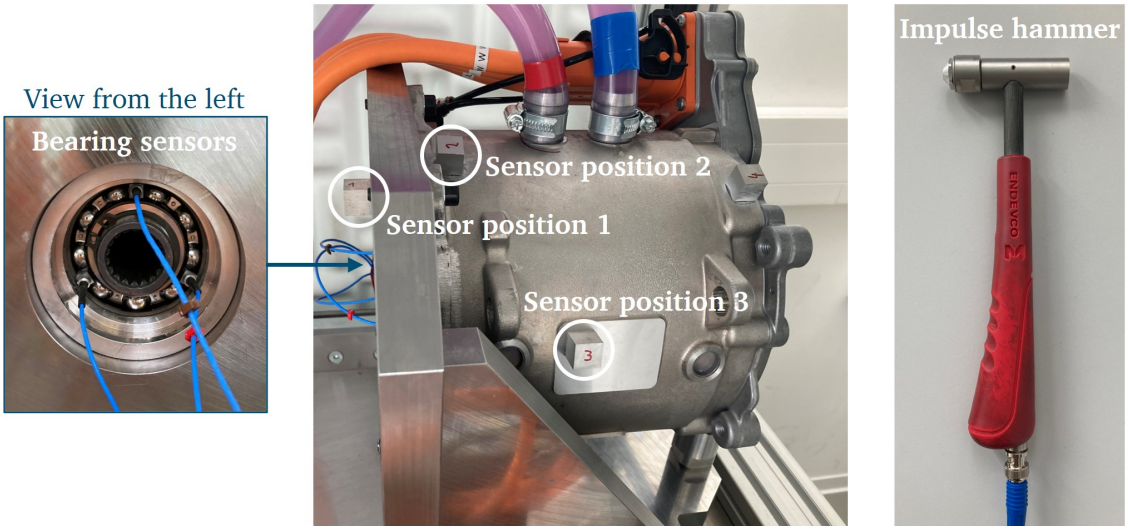

Figure 7.3.: FRF measurement setup at the e-machine test bench.

In contrast to the original measurement setup which was used to acquire data from the bearing experimental runs, presented in figure 5.6, instead of the actual sensors, aluminium cubes are glued at the sensor positions to enable the force excitations with the impulse hammer in all 3 spatial directions. To measure the acceleration response, three PCB Piezotronics Model 356A03 triaxial accelerometers are glued inside a type 6207-C3 bearing at the outer ring. In contrast to the original test bearings prepared for fault diagnosis in chapter 5.3, this bearing comes with a different cage design and offers more installation space which is needed for mounting the accelerometers. The bearing accelerometers are placed with an angular distance of 120°. Reason for the use of multiple accelerometers is to measure a wider variety of transmission paths, since the real location of force excitation inside the bearing depends on the fault location and can vary during operation of the machine. A weighted average of the different bearing sensors' FRFs are used for final FRF determination. More specifically, the final accelerances are calculated by using the mean values of the accelerances from each bearing sensor's gravitational direction.
For FRF measurement acquisition, the software *ArtemiS SUITE* is used. Within the measurement prodecure, each spatial direction of the aluminium cubes is excited ten times using the impulse hammer. Performing ten consecutive measurements on each excitation point helps to ensure that the measurements are not corrupted by incorrect hammer excitations. For these measurements, the hammer is equiped with an aluminum

tip to enable short impulse durations which lead to high frequency ranges of the broadband excitation, see section 4.4.2. For each measurement, the impact force is measured by the force sensor inside the hammer and the responding acceleration is recorded from the bearing sensors. A single, exemplary hammer force excitation e_h and the corresponding acceleration response a_h are visualized in figure 7.4.

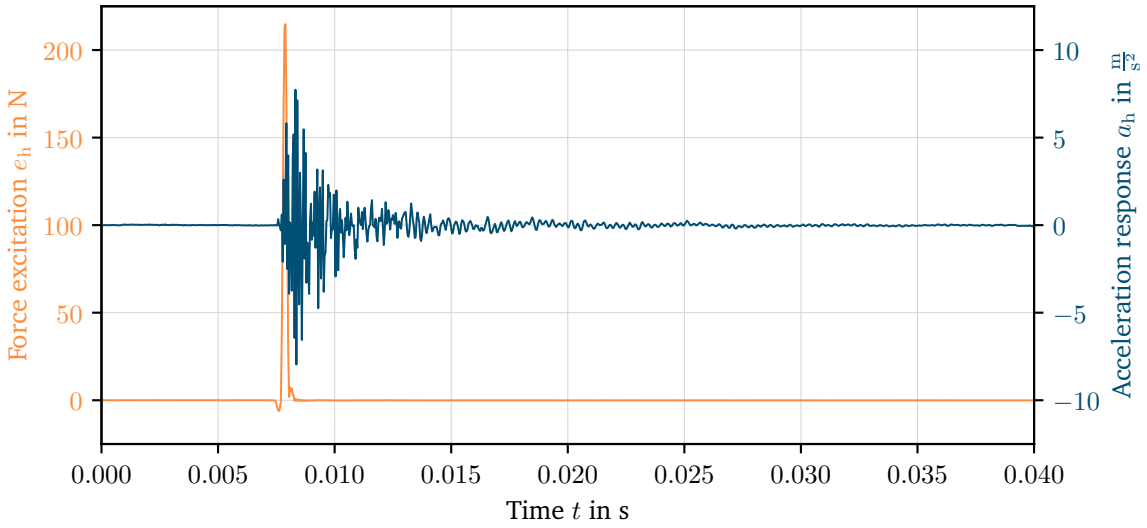

Figure 7.4.: Exemplary FRF measurement in time-domain.

In accordance with the mathematical foundations already explained in section 4.4.1, the accelerance is determined in frequency-domain by making use of the convolution theorem. First, both the hammer force and the responding acceleration signals are transformed into frequency-domain via FFT. Second, the accelerance is determined by frequency-wise division.

$$H(f) = \frac{A_\mathrm{h}(f)}{E_\mathrm{h}(f)} \tag{7.1}$$

To visualize the differences inbetween the FRFs in frequency-domain, exemplary accelerances are presented in figure 7.5. Specifically, the axial directions of the individual physical sensors (1z, 2x and 3x) are selected for this visualization. The positionings and orientations of the sensor channels mentioned can be found in figure 5.6. Comparing the three accelerance spectra in the logarithmically plotted diagram, particularly large deviations are visible in the high frequency ranges from 7 to 10 kHz.

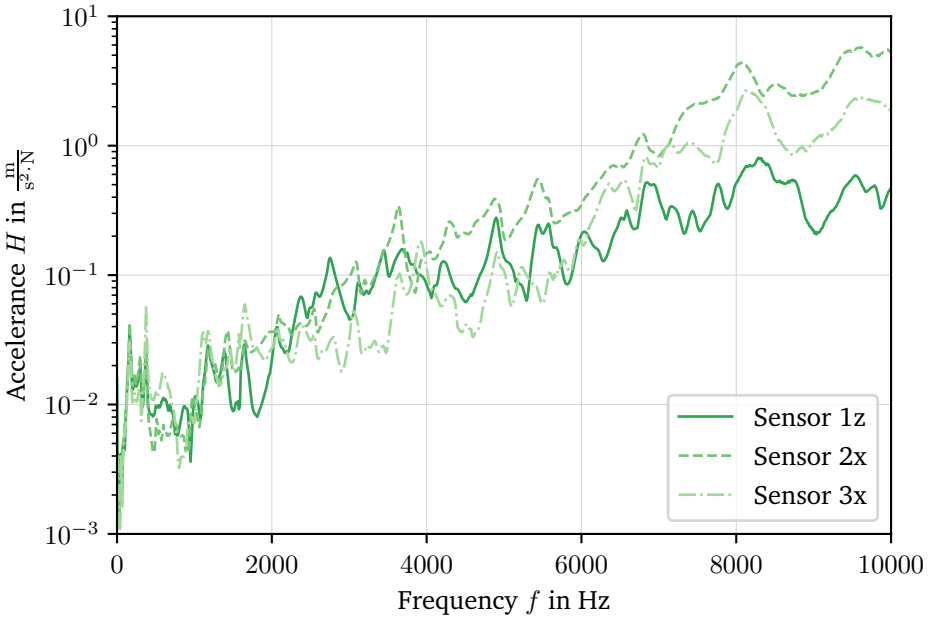

Figure 7.5.: Exemplary accelerances in frequency-domain.

Based on the measured frequency-domain accelerances, the now following section 7.1.2 explains the virtual force determination.

7.1.2. Calculation of Virtual Bearing Force Spectra

The virtual force spectra are calculated on the basis of the bearing fault acceleration measurements, the acquisition of which already was presented in chapter 5. By applying the FFT on the acceleration time-domain signals, acceleration amplitude spectra are generated. Figure 7.6 exemplarily shows these spectra for the 3 sensor channels already considered in figure 7.5. For the bearing fault classes, only the Reference bearing and IR Laser fault measurements from experimental series A are visualized due to the purpose of visual clarity. To suppress the noisy behavior of the original spectrum, a Gaussian filter is applied before generating the visualization by convolving the original frequency-domain data with a Gaussian kernel function characterized by a standard deviation of 50 Hz. For further information on this Gaussian-based smoothening, please refer to section 4.3.2. The Gaussian filtering is used for visual purposes only and is not applied for the processing presented later for utilization of the ML algorithms.
Having both accelerations (figure 7.6) and accelerances (figure 7.5) in frequency-domain, the virtual force spectra can be calculated by rearranging equation (4.15) and replacing the actual excitation force E with the virtual force V.

$$V(f) = \frac{A(f)}{H(f)} \tag{7.2}$$

Similar to the acceleration spectra visualized in figure 7.6, figure 7.7 shows the Gaussian-smoothed virtual force spectra.

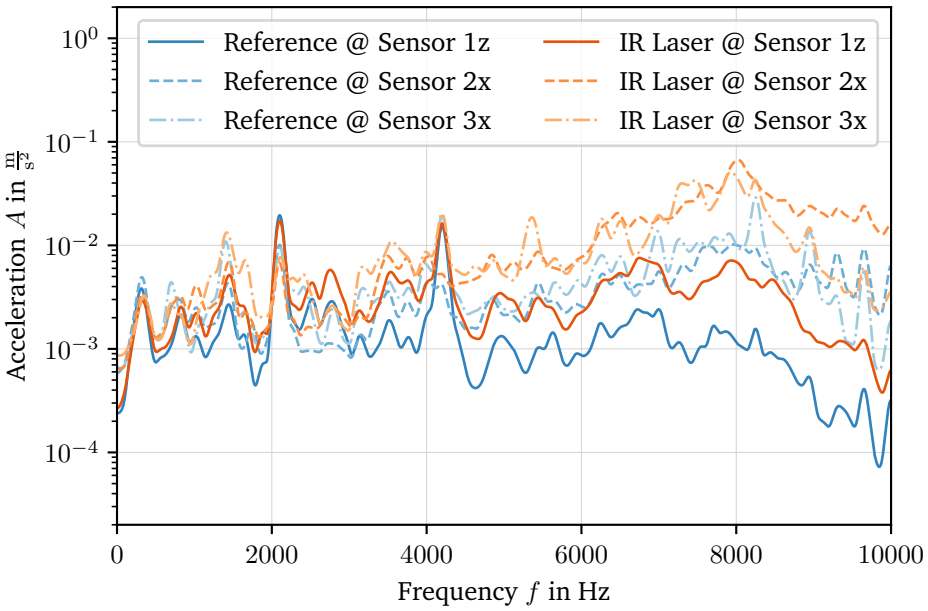

Figure 7.6.: Exemplary acceleration frequency-domain spectra.

Taking a comparitive look at figures 7.6 and 7.7, the overlap inbetween the Reference bearing (blue) and IR Laser fault (orange) can be analysed.

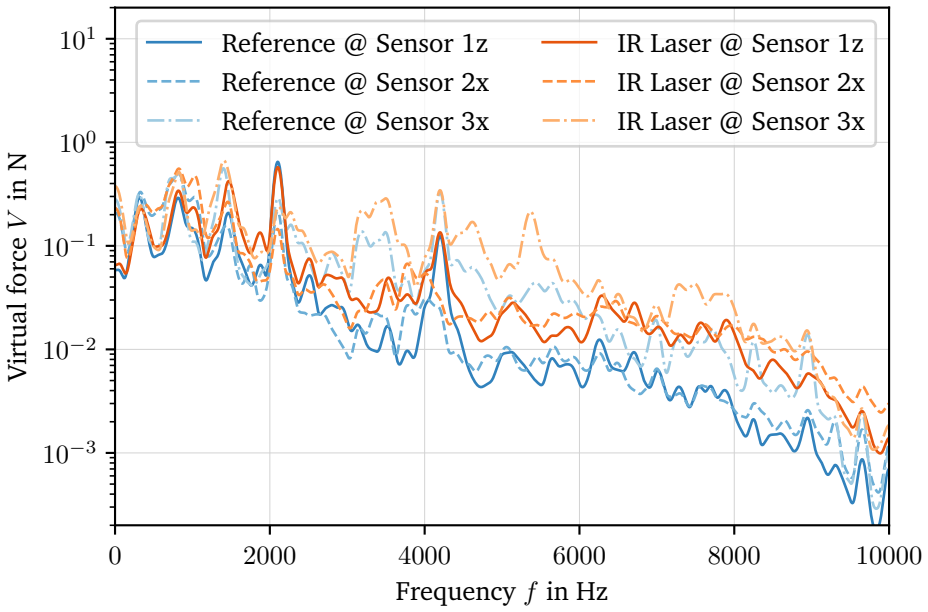

Figure 7.7.: Exemplary virtual force frequency-domain spectra.

If all orange curves are clearly separated from all blue curves in terms of their amplitudes, a well-defined distinction between the two classes is given. In contrast, if the blue and orange curves strongly overlap, this input data limits the ML algorithms' ability to distinguish between the classes. This problem was already illustrated in an analogous way using the time-domain RMS in figure 6.1. Looking at the acceleration spectra in figure 7.6, a lot of overlap is present. In particular, the IR Laser measurement from sensor 1z clearly intersects with the Reference data from sensors 2x and 3x in the high frequency range inbetween 7 and 10 kHz. This overlap is reduced when looking at the virtual force spectra in figure 7.7.
The visual frequency-domain considerations conducted in the present section are merely intended to enable comprehensibility of the virtual force approach. The quantitative evaluation of this new approach takes place in section 8.1. There, the virtual force frequency-domain data is used for feature generation instead of the original acceleration data to evaluate the transferability of the resulting fault diagnosis model. Now, the following section 7.2 introduces an additional approach as an alternative to the virtual force approach.

7.2. Approach 2: Calibration Bearing

In contrast to the hammer-based excitation of Approach 1, Approach 2 aims to use an actual bearing fault to excite the dynamic forces, the vibration responses of which are to be determined. For this purpose, a so-called calibration bearing must be prepared with a well-defined fault. This specifically prepared bearing is used in a separate experimental run to determine the vibration responses measured from the different sensor channels' positions and directions, which were shown in figure 5.6. Although the actual force excitation remains unknown, it shall be evaluated if these additional acceleration measurements can be used to calibrate the previously recorded fault diagnosis data in frequency-domain.

7.2.1. Specification of Fault Geometry

The fault geometry of the calibration bearing has to be well-defined to provide constant properties of the force excitation for a given operating condition. Ideally, the fault geometry is reproducible. The calibration bearing is supposed to create a broadband excitation with a high frequency range. This is intended to be achieved by creating sharp edges at the artificially prepared bearing fault. For the reasons mentioned above, a laser-ablation-based fault is selected again here. To ensure a circulating force excitation, the bearing's inner race is treated. The measured topography resulting from the laser-ablation process to the inner race of the calibration bearing is visualized in figure 7.8.

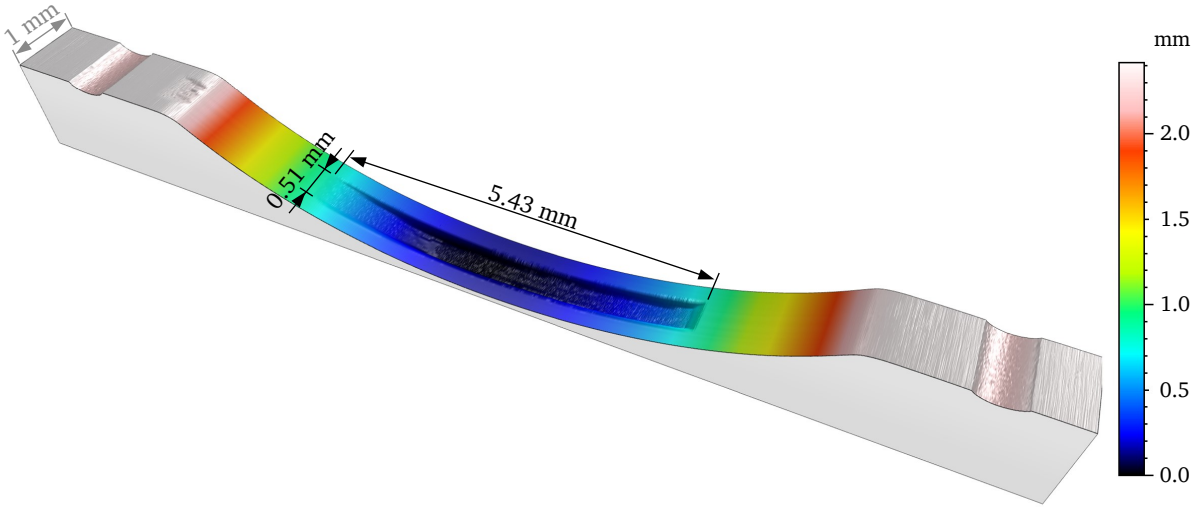

Figure 7.8.: Measured topography of the calibration bearing fault at its inner race.

In comparison to the previously created IR Laser fault, which was visualized in figure 5.9, the present fault of the calibration bearing is considerably larger in its dimensions. Assuming idealized kinematics for a ball passing through this fault inside the bearings load zone, the ball would be subject to a radial movement of up to 7.4 µm.

7.2.2. Calibration of Acceleration Spectra

The main calibration idea of Approach 2 is stated in equation (7.3). In an equivalent way to the virtual force approach (Approach 1), each acceleration measurement is calibrated by a division in frequency-domain. In contrast to equation (7.2), the denominator is given by the frequency-domain acceleration from the calibration bearing experiment A_c instead of the accelerance H. Thus, the calibrated acceleration C is calculated as another basis for feature generation to compare against the original acceleration A and the virtual force V.

$$C(f) = \frac{A(f)}{A_\mathrm{c}(f)} \tag{7.3}$$

To measure the calibration acceleration data a_c, the prepared calibration bearing is installed into the e-machine and run within an experiment in a similar way to the bearing fault experiments presented in section 5.4. However, after 5 hours of run-in at an inner ring speed of 3500 rpm, the speed is reduced for the actual data acquisition. With respect to the rotational speed during the calibration measurement, the following hypothesis is formulated:

> *Hypothesis: Assuming that all measurement data is calibrated using the same rotational speed of the calibration bearing, the proposed calibration approach works independently of this speed's specific value.*

To test this hypothesis within reasonable boundaries, measurements are taken with the calibration bearing running at three rotational speed levels in the following order within a single experimental run:

- $f_\mathrm{i} = 2000$ rpm
- $f_\mathrm{i} = 1500$ rpm
- $f_\mathrm{i} = 1000$ rpm

The specified speeds are approached seamlessly after the run-in phase. Each speed is kept for 10 minutes, with the last 300 seconds being used to acquire the respective calibration data.
To illustrate the effect of the calibration, figure 7.9 shows exemplary calibrated accelerations in a similar manner to the visualizations of the original accelerations and the virtual forces already presented in figures 7.6 and 7.7.

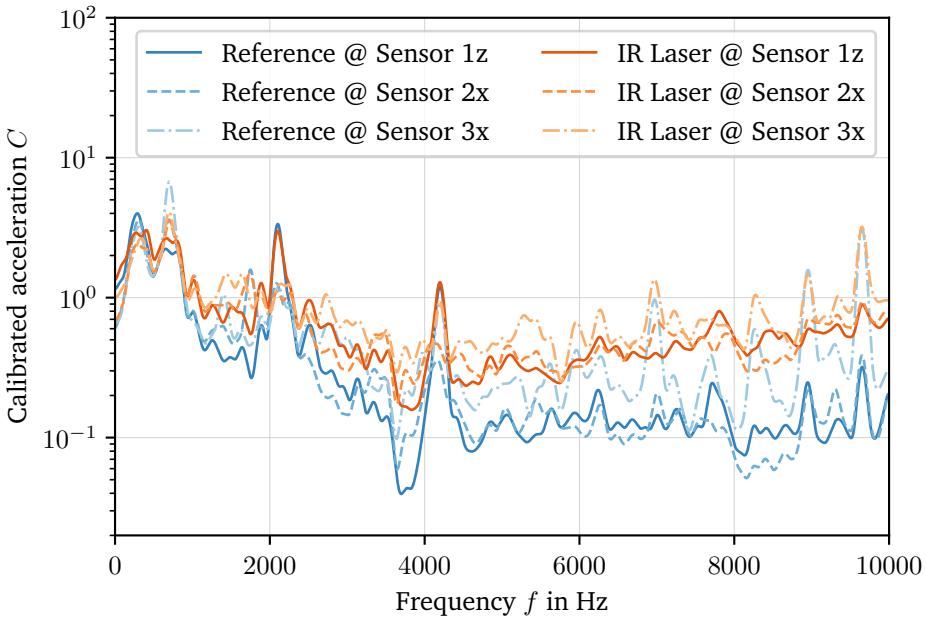

Figure 7.9.: Exemplary calibrated acceleration frequency-domain spectra; with calibration bearing at $f_\mathrm{i} = 2000$ rpm.

As depicted, the dimensionless calibrated acceleration allows the IR Laser fault and Reference bearings to be well separable from each other from a visual point of view. However, it can be observed that there are still some deviations inbetween the different sensor channel measurements. If Approach 2 showed perfect results, the blue lines representing different sensor channels for the Reference bearing would equal each other. In the same way, all orange lines representing the IR Laser fault would match exactly. Since this is not the case, the performance of the given approach is analysed in more

detail in section 8.1. Additionally, the previously proposed hypothesis regarding the influence of the calibration bearing's rotational speed is investigated in section 8.2.
With the two novel approaches for the calibration of acceleration data presented in sections 7.1 and 7.2, Research Question 2 is now addressed. Building upon this, the next chapter 8 evaluates these novel approaches using the 2D transfer scenario.

8. Transferability Evaluation of the Extended Approaches

Based on chapter 6, which analysed the transferability of a fault diagnosis model using acceleration data, two novel approaches were presented in chapter 7 to enhance transferability. Now, with the goal of answering Research Question 3, the present chapter evaluates these two newly proposed approaches in comparison to the current state of research. To enable an objective comparison, the framework depicted in figure 8.1 is utilized.

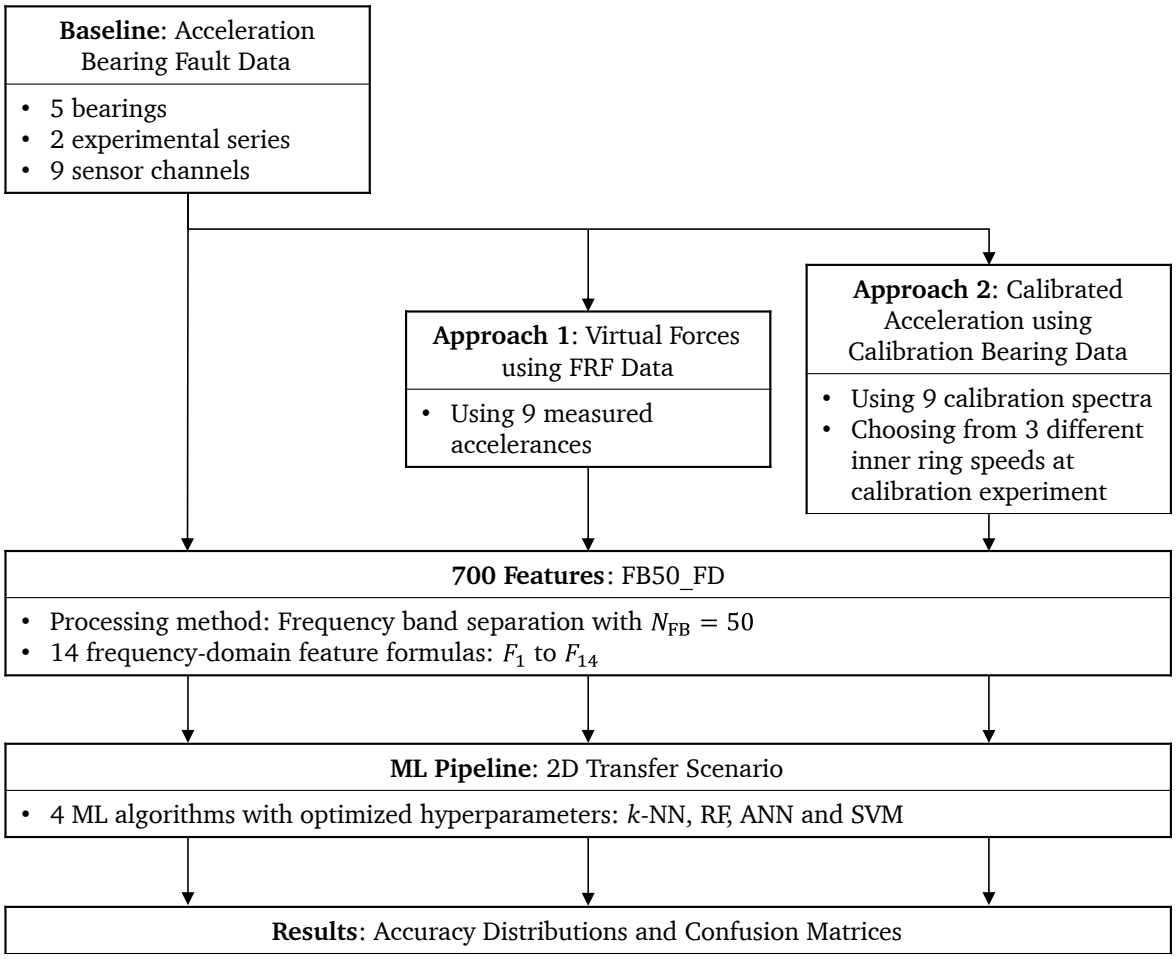

Figure 8.1.: Framework for generation of final results.

In addition to the baseline acceleration data, the processing steps introduced as part of

Approach 1 and Approach 2 are applied to generate the virtual forces and the calibrated accelerations, respectively. Afterwards, feature generation and ML are performed according to the 2D scenario, as already used for the acceleration-based transferability evaluation in section 6.5. The final results are evaluated by making use of the cross-validation-based accuracy distributions and their mean values, as well as confusion matrices.
Next, section 8.1 presents the final results of the two newly proposed approaches in comparison to the baseline acceleration-based approach. Afterwards, the hypothesis regarding the influence of the rotational speed for Approach 2 is addressed in section 8.2.

8.1. Comparison of Results

To enable an objective result comparison, the framework illustrated in figure 8.1 is utilized. The final, comparitive accuracy distributions can be obtained in figure 8.2. For now, Approach 2 is evaluated based on the $f_\mathrm{i} = 2000$ rpm calibration data.

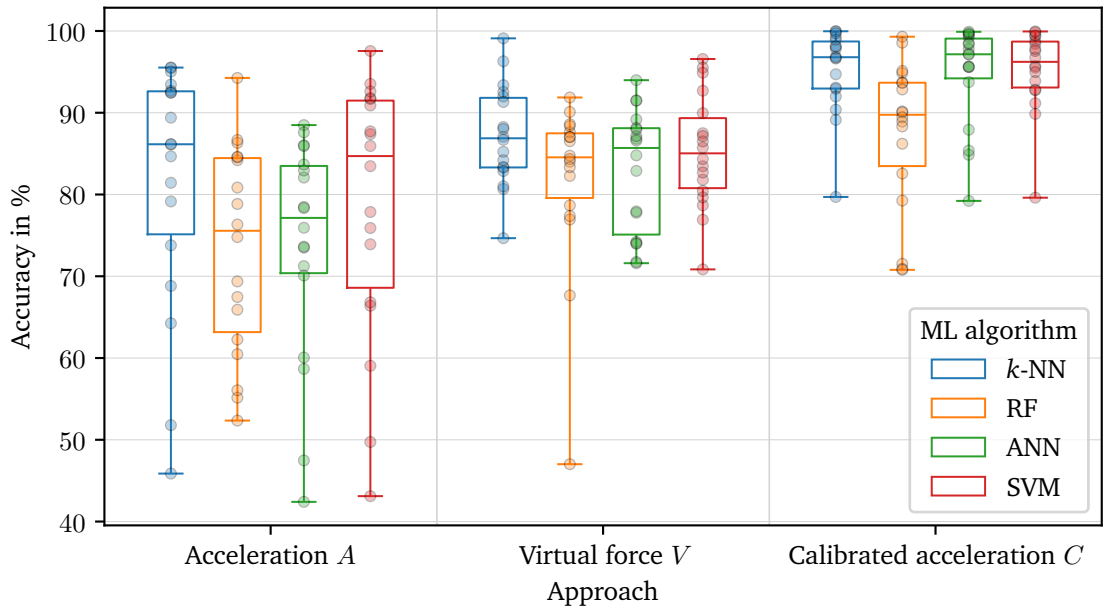

Figure 8.2.: Box plot of predictive accuracies comparing the different approaches using the 2D scenario; with FB50_FD feature set and optimized hyperparameters; with calibrated acceleration C based on the $f_\mathrm{i} = 2000$ rpm calibration data.

Here, the box plot is generated in the same manner as already explained in the context of figure 6.19. In addition to the presented accuracy distributions, table 8.1 provides the corresponding mean accuracy values to facilitate the comparison through the use of single numerical values.

Table 8.1.: Mean accuracy comparison between the different approaches using the 2D scenario; with FB50_FD feature set and optimized hyperparameters; with calibrated acceleration C based on the $f_\mathrm{i} = 2000$ rpm calibration data.

	Mean accuracies		
ML algorithm	Acceleration A	Virtual force V	Calibrated acceleration C
k-NN	81.6 %	87.2 %	95.2 %
RF	73.4 %	81.9 %	87.6 %
ANN	73.7 %	82.9 %	94.7 %
SVM	78.6 %	85.3 %	95.2 %

To enable an indepth analysis of the results, two natural boundaries of expectable accuracy results shall be mentioned briefly. First, the natural upper limit of the accuracy, which only a perfectly predicting model would reach, is 100 %. Second, a natural lower bound for reasonable accuracies is given by the predictive accuracy of a dummy, uninformed model, which has to randomly guess its predictions. For the given case of an evenly balanced 5-class classification, the expected value of the random guess-based accuracy equals 20 %.
With this in mind, figure 8.2 shows that the baseline acceleration-based approach performs with a wide dispersion of accuracies covering a large proportion within the aforementioned boundaries. Accordingly, the individual accuracies are highly dependent on the particular sensor channels used for training within the cross-validation procedure. On average, the mean accuracies, depending on the ML algorithm, are located in the range of 73.4 % to 81.6 %. Thus, 18.4 to 26.6 % of the predictions are wrong in total for the baseline approach.
Looking at the virtual force-based results coming from Approach 1, the mean accuracies are increased. The overall proportion of wrong predictions is reduced to the range of 12.8 to 18.1 %. Furthermore, with the calibration bearing Approach 2, this proportion is reduced even further, reaching 4.8 to 12.4 %. Thus, it can be seen that both of the novel approaches provide improved transferability compared to the current state of research. In particular, Approach 2 performs superior.
Comparing the different ML algorithms, the results deviate slightly from each other. In particular, for the virtual force and calibrated acceleration approaches, the RF shows lower performances. In comparison, overall high accuracies are observed using the k-NN and SVM algorithms.
The now following paragraphs go into more detail to analyze the proportions of incorrectly predicted classes. For this purpose, the confusion matrices of Approaches 1 and 2 are shown in figures 8.3 and 8.4, using the SVM-based results. The corresponding confusion matrix of the baseline acceleration-based results was already presented in figure 6.22 and can be considered as a reference here.

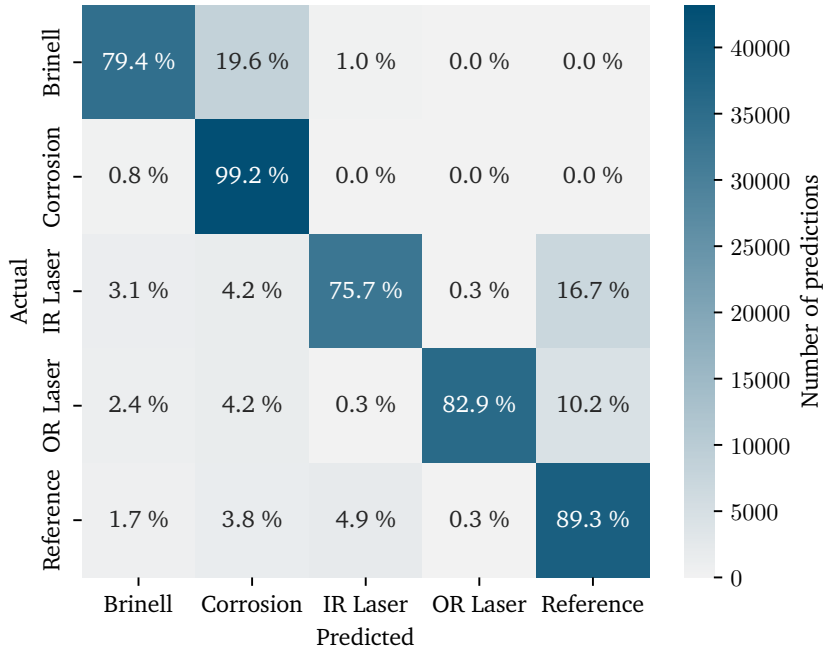

Figure 8.3.: Confusion matrix for the 2D scenario using Approach 1: Virtual forces; with FB50_FD feature set and hyperparameter-optimized SVM classifier.

For each bearing class, 43200 predictions are made on the testing data. Comparing the different bearing classes, the Corrosion fault is detected most accurately. This observation is consistent with the results already observed in figure 6.22 using the baseline acceleration data. Since the prepared Corrosion fault was already analysed in section 6.1 to be a strongly pronounced fault in comparison to the remaining 3 faults, this more reliable identifiability is plausible. For the virtual force approach, the largest proportions of misclassifications are allocated inbetween the Brinell and the Corrosion faults. Additionally, there is an increased amount of confusion among the 3 classes of IR Laser fault, OR Laser fault and Reference bearing.
Moving on to the confusion matrix in figure 8.4 to evaluate Approach 2, the observed missclassification rates are much lower compared to Approach 1. In particular, the Brinell, Corrosion and IR Laser faults are detected very reliably. Only some wrong predictions are made inbetween the OR Laser fault, the IR Laser fault and the Reference bearing. As already shown in section 6.1, both IR Laser and OR Laser faults are only slightly pronounced. Thus, for real-world applications, these misclassifications would be rather acceptable in comparison to misclassifications of the more ponounced Corrosion and Brinell faults.

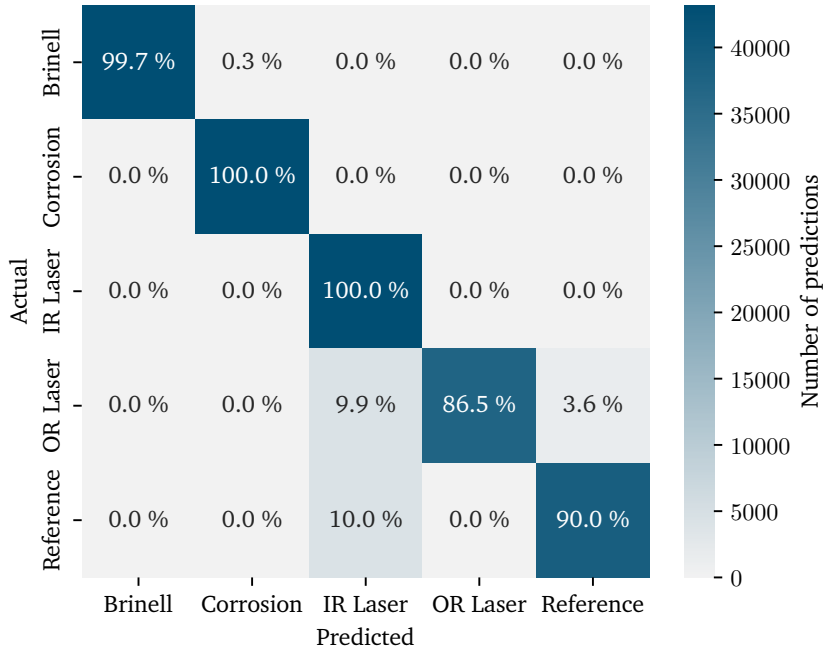

Figure 8.4.: Confusion matrix for the 2D scenario using Approach 2: Calibrated acceleration; based on the $f_\mathrm{i} = 2000$ rpm calibration data; with FB50_FD feature set and hyperparameter-optimized SVM classifier.

The results presented here provide the foundation for answering Research Question 3. However, for an indepth discussion of these results, please refer to chapter 9. Next, section 8.2 addresses the influence of the rotational speed during the calibration experiment.

8.2. Influence Investigation of the Rotational Speed for Approach 2

In section 7.2.2, the hypothesis was proposed that Approach 2 works independently of the inner ring rotational speed f_i during measurement of the calibration data. To test this hypothesis on a limited scale, data was acquired from three different speeds (1000, 1500 and 2000 rpm). It is worth emphasizing that none of these speeds matches the speed of 3500 rpm which was used to generate the bearing fault data in chapter 5.
To check for influence of the different rotational speeds, the framework presented in figure 8.1 is used again. The resulting accuracy distributions for the different inner ring speeds are visualized in figure 8.5.

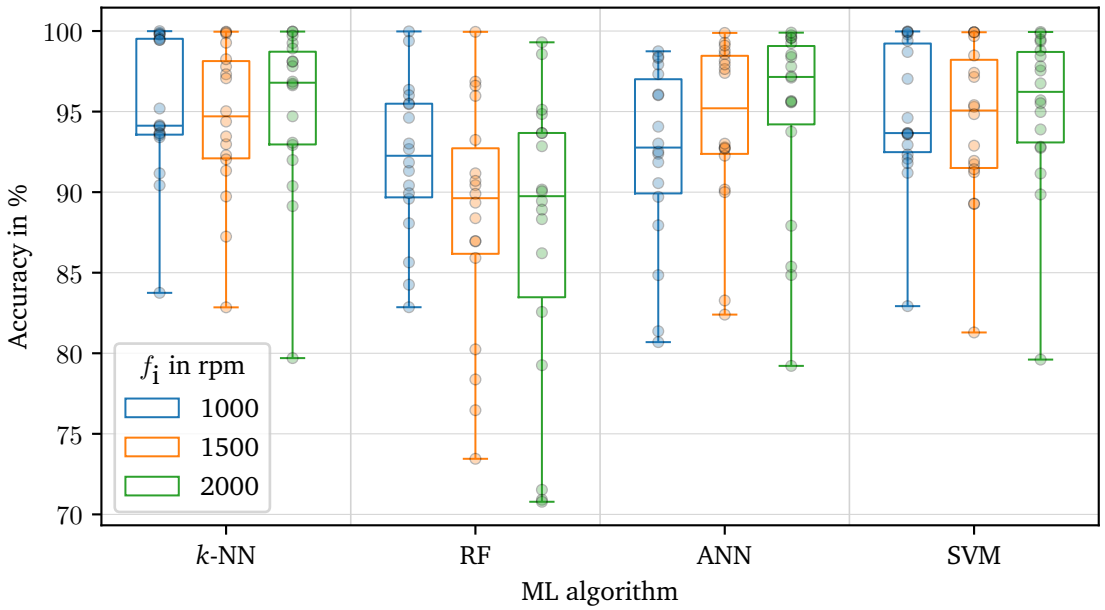

Figure 8.5.: Box plot of predictive accuracies comparing different calibration bearing inner ring speeds using Approach 2 in the 2D scenario; with FB50_FD feature set and optimized hyperparameters.

Slight trends of the accuracy distributions in correlation to the inner ring speed f_i can be discerned. However, the directions of the trends are not uniform when comparing the individual ML algorithms. Reducing the distributions from figure 8.5 to single representative values, table 8.2 presents the corresponding mean values of the predictive accuracies.

Table 8.2.: Mean accuracy comparison between the different calibration bearing inner ring speeds using Approach 2 in the 2D scenario; with FB50_FD feature set and optimized hyperparameters.

	Mean accuracies		
ML algorithm	1000 rpm	1500 rpm	2000 rpm
k-NN	95.3 %	94.5 %	95.2 %
RF	92.1 %	88.4 %	87.6 %
ANN	92.3 %	94.2 %	94.7 %
SVM	94.8 %	94.3 %	95.2 %

The mean values clarify that there is no uniform accuracy-trend depending on the rotational speed. Minor variations of the predictive performance may be attributed to uncertainties inherent in the measurements. One additional reason for the deviations

may be given by non-linear system behavior. When operating the calibration bearing, a higher rotational speed leads to more powerful vibrations. In the presence of non-linear effects, this could cause fluctuations in performance of the calibration approach. However, considering both the accuracy distributions and their mean values, it is concluded that the influence of the rotational speed on the performance of Approach 2 is negligible. Thus, the hypothesis is considered to be verified within the scale of rotational speeds presented here.
Given these results, the next chapter 9 discusses the findings with respect to the initially formulated Research Questions. Furthermore, the viability of the proposed methods in an industrial environment is discussed.

9. Discussion

Based upon the results already presented in chapters 6 to 8, the investigated approaches and their implementations are to be discussed within the present chapter. Firstly, the benchmark acceleration-based approach and its performance is analyzed to compare the different transfer scenarios, which were introduced in the context of figure 6.15:

- 0D scenario: Training and testing on the same experimental series and unchanged sensor channels leads to very high predictive accuracies. For this 0D scenario, figure 6.18 presents mean accuracies of 100 % for almost all feature sets within investigation. This can be attributed to the feature distributions being nearly identical for both training and testing data. However, since both training and testing data are taken from the same experimental runs, these high prediction accuracies cannot be expected to be representative for real industrial applications.

- 1D-E scenario: Training and testing on completely separate experimental series makes the 1D-E scenario represent a more close-to-reality use case. However, it makes predictions more difficult in comparison to the 0D scenario. Apparently, the intermediate disassembly and reassembly of the e-machine in the course of the test bearing replacements cause differences in the measurement data, which the algorithm must be able to handle. Using simple time-domain features and a baseline RF algorithm without its hyperparameters being optimized, a mean accuracy of only 81 % is achieved. By choosing the best-performing feature set (FB50_FD) and by optimizing the hyperparameters of multiple ML algorithms, mean accuracies of around 100 % are reached. However, since the 1D-E scenario is used for feature and hyperparameter selection, it cannot be completely ruled out at this point whether the algorithms are overfitted.

- 2D scenario: In addition to using separate experimental runs, the feature and ML algorithm configurations determined based on the 1D-E scenario are used to perform predictions based on testing data which is recorded from a different sensor channel. Thus, training and testing data correspond to different structural dynamic behaviors. With the acceleration-based approach in the 2D scenario, only 73.4 to 81.6 % mean accuracy is reached, with slight deviations depending on the ML algorithm in use. Accordingly, the mean accuracy is reduced by at least 18.4 % in comparison to the 1D-E scenario. As part of the implemented cross-validation procedures, it is observed that the signal properties and the resulting predictive accuracies are highly dependent on the positioning of the vibration-sensing accelerometers. With respect to the accuracy distributions presented in figure 6.20, it is concluded that the transfer of conventional, acceleration-based

ML models to systems with differing structural dynamics leads to a significant loss in predictive performance and is therefore not recommended for real-world applications. This concludes Research Question 1.

Building on the above mentioned results, Research Question 2 is raised to develop novel conceptual approaches in order to increase the models' transferabilities to systems with differing structural dynamics. This is answered within chapter 7 by introducing two novel approaches, both of which making use of an additionally introduced calibration step. The following key points briefly summarize the two novel approaches and their performances in the 2D scenario from chapter 8:

- Approach 1: Virtual forces: By using measurements of the FRFs in terms of their accelerances, so-called virtual forces are calculated from the original acceleration data. Using the same feature and hyperparameter configurations as resulted from the acceleration-based baseline approach in the 1D-E scenario, the transferability of this new approach is evaluated. With the 2D scenario, in comparison to the baseline acceleration-based approach, a performance improvement is achieved, reaching mean accuracies inbetween 81.9 and 87.2 %.

- Approach 2: Calibration bearing: In contrast to the FRF measurements, Approach 2 uses a dedicated experimental run with a distinctly prepared calibration bearing. Frequency-domain division enables the calculation of calibrated acceleration spectra, which are again used with the same feature and hyperparameter configurations from the previous approaches to allow for an unbiased comparison. Compared to Approach 1, the predictive performance for Approach 2 is even higher and achieves mean accuracies of 87.6 to 95.2 %. In contrast to the previous approaches, the more severe faults (Corrosion and Brinell) are diagnosed almost perfectly here. Only the less pronounced faults (IR Laser and OR Laser) as well as the Reference bearing are confused to a small extend. This confirmes the good performance of Approach 2.

With reference to figure 8.2 and table 8.1, a quantitative answer to Research Question 3 is provided. Besides the differences in predictive performance, both of the newly proposed approaches vary with respect to their practicability. Approach 1, which comes with some disadvantages regarding its implementation, is therefore first discussed in terms of its feasibility:

- The execution of FRF measurements requires special measuring equipment and additional technical knowledge on structural dynamics. This limits the widespread practicability of Approach 1.

- For the present e-machine-based investigations, the severely restricted space at the bearing location prevents the excitation force from being applied in the desired manner. Therefore, a reciprocal measurement is performed by fitting accelerometers inside the bearing. The suitability of this reciprocal measurement for the

given case is based on the assumption of a linear system behavior, which cannot be guaranteed. For machines with smaller bearings, the installation space for sensor placement may be even more limited, which could prevent even the reciprocal measurement technique.

- The reciprocal FRF measurement can only be realized with respect to discrete locations inside the bearing. However, the true excitation is circumferential for inner race, rolling element and cage faults due to their movements during operation, and not localizable in advance for outer ring faults. Randall already described the underlying problem in the following way: "Where the fault is moving, the transfer function of the transmission path varies with respect to the fixed positions of response transducers." [13, p.47]

For the reasons mentioned above, the transmission paths measured in section 7.1 are not expected to exactly equal the transmission paths corresponding to the fault-exited structure-borne sound propagation during e-machine operation. Thus, the mediocre predictive accuracies of Approach 1 in the 2D scenario-based transferability evaluation seem to be reasonable.
Approach 2 avoids the disadvantages coming with the impulse hammer-based FRF measurements by making use of a real bearing fault excitation and the corresponding response measurements. However, the implementation realized here shall also be critically assessed:

- The bearing fault-based, circumferentially distributed force excitation is expected to be more realistic in comparison to the hammer-based FRF measurements. However, the actual level of excitation forces remains unknown. In contrast to the virtual forces, which represent a physical quantity, the calibrated acceleration therefore lacks a directly interpretable meaning.

- For the present case, only one single calibration experiment is performed and used to calibrate all sensor channels. This neglects the additional measurement fluctuations which may occur from intermediate removal of the calibration bearing. A more sophisticated approach would use a single experimental run of the calibration bearing for each individual sensor channel, with removal and installation of the calibration bearing between each experimental run to incorporate uncertainties introduced during e-machine reassembly. This is not implemented in the present work due to the substantial additional effort involved. However, in the case of a model transfer between two machines with differing structural dynamics, these additional experiments would have to be carried out. Thus, the validation of the results presented here is still pending.

Initially, the overarching aim of the present research was stated to advance the transferability of data-driven models for bearing fault diagnosis. Based on the specified research gap, this aim was narrowed to focus on the transferability of vibration-based fault diagnosis models from one system to a system with differing structural dynamics. Based on

experimental data, which was acquired from an e-machine test bench, the transferability of different models for bearing fault diagnosis was evaluated by utilizing measurement data from different sensor positions. Based on the discussion of the results presented within the current chapter, the following, final chapter 10 concludes the contribution of this work to the state of research and, building upon that, identifies opportunities for future research.

10. Conclusion and Outlook

Condition monitoring and fault diagnosis are fundamental to the implementation of condition-based maintenance. By making use of ML algorithms, fault diagnosis can be provided in an automated way. In the automotive industry, rising levels of automated driving and an increasing number of fleet vehicles cause high demands on the safety and reliability of automotive subsystems. To meet these demands, implementing reliable and automatic diagnosis of upcoming faults is a promising solution. However, to enable ML-based fault diagnosis of a particular system, a data-driven model has to be trained on extensive data sets. The acquisition of this data requires a considerable amount of time and expense. By enabling models to be reusable, these hurdles in terms of high expense would be reduced significantly. Thus, the transferability of fault diagnosis models would enable condition-based maintenance to be profitable for many new applications.
Driven by the aforementioned reasons, the present research contributed to the state of research by enhancing the transferability of vibration-based, data-driven models. In particular, this work focused on enabling the models' transferability to technical systems with differing structural dynamic behaviors. Acceleration data was acquired from an e-machine test bench at various positions to verify the proposed methods. Multiple ball bearings with healthy and faulty conditions were prepared to run within several experimental runs. Thus, a classification task was set up to evaluate the transferability of different model generation approaches.
The investigations started by using models trained on acceleration data. It was found that training and testing on completely separate experimental series, which represents a realistic scenario, is a considerably more difficult task for fault diagnosis than training and testing on the same experimental runs, as it is frequently carried out within past literature. Within a comparative analysis of different feature engineering methods, frequency-domain features calculated on a high number of separated frequency bands resulted in the most accurate fault classifications.
In addition to transferring the fault diagnosis models to a different experimental series, a transfer to different sensor positions was introduced. Here, the various sensor positions are accompanied by different vibration transmission paths, representing varying structural dynamic behaviors. It was shown that the transfer to varying structural dynamic behaviors significantly reduced the acceleration-based models' predictive accuracy.
Two novel approaches were proposed to enhance transferability by incorporating domain knowledge on structural dynamics. Both approaches make use of additional measurements of the transmission behavior inbetween the location of force excitation at the bearing and the vibration response at the sensor positions.
On the one hand, Approach 1 uses frequency response measurements to calculate so-called virtual forces. Calculating features based on these virtual forces in an equivalent

way as previously with the original acceleration data, the virtual force-based fault diagnosis models allow for improved predictive accuracies when transferred to a different sensor position. However, due to space constraints, this approach comes with some challenges regarding the implementation of frequency response measurements.
On the other hand, Approach 2 calibrates the acceleration signals by using an additional, specifically prepared bearing fault to measure the sensor positions' differences in acceleration response. This calibration bearing approach can outperform the virtual force approach in terms of its transferability. Accordingly, Approach 2 is considered to be preferable to Approach 1 for industrial applications.
As part of the final performance evaluations using the transfer scenario to different sensor positions, the following predictive performances are achieved with the SVM as a representative ML algorithm: Whereas the baseline acceleration-based approach results in a mean accuracy of only 78.6 %, Approach 1 causes a raise to 85.3 %, and Approach 2 enables mean accuracies of even 95.2 %. Accordingly, the superior performing Approach 2 enables a reduction of the misclassification rate by more than 3/4 for the presented investigations.
In conclusion, Approach 2 is recommended for enhancing the transferability of a given fault diagnosis model to a new technical system with differing structural dynamics. Thus, improved fault diagnosis functionality can be provided without the necessity of additional a priori training data. Although the validation of the presented approaches is still pending, this thesis' contribution to the state of research is expected to improve rapid and cost-effective deployments of automated fault diagnosis for implementing condition-based maintenance on new systems. This can bring benefits not least to e-machine applications for future vehicles.

Within future research, transferable ML approaches for fault diagnosis should be further expanded. In particular, the presented approaches could be validated using the transfer between different machines instead of different sensor positions. To further improve the transferability of fault diagnosis models to systems with differing structural dynamics, additional techniques for implementing the proposed calibration step should be examined. For example, within Approach 1, the FRFs could be determined by simulating the structural dynamics of the system instead of measuring them. Furthermore, non-linear modeling of the frequency response may help to improve the transferability of the fault diagnosis model.
Additionally, since the present work focuses on the impact of differing structural dynamics in an isolated way, the presented approach for handling differences in structural dynamics should be combined with approaches for handling varying operating conditions and measurement chains. Furthermore, the influence of different bearing types and sizes on the measurement data should be investigated and integrated into the modeling. Thus, an overall approach for transfering vibration-based fault diagnosis models to different technical systems in general may be developed.
Within the presented research, the ML modeling was based on explicitly designed feature sets. For future research on larger data sets, this feature generation could be replaced by incorporating Deep Learning techniques such as Deep Convolutional Neural Networks,

which are suitable for processing the raw data directly. Moreover, the classification task used within this work can be extended to diagnose a greater variety of failure modes and their degrees of severity. This can for example be accomplished by utilizing regression models.
The present work deals with the diagnosis of faults in order to enable non-predictive, condition-based maintenance. Building on this, future work could additionally incorporate a model of future degradation. By adding this prognostic step, a transferable model for predictive maintenance planning could be developed.
In addition to monitoring the faults of rolling bearings, future investigations could apply the proposed approaches to different tribological systems such as gears. Since gear faults can also be detected by vibration monitoring, the approaches used for bearing fault diagnosis should be applicable in a similar way.
Furthermore, future research could work on applying the presented transferability approaches to different measurement principles in an analogous way. Thus, instead of using Vibration Monitoring, continuing research could additionally focus on principles such as Acoustic Emission, Electrical Currents, or Electrical Impedances. Overall, the performance of the fault diagnosis and the transferability of models relying on different measurement principles should be assessed comparatively.

A. Convolution Theorem

Proof. In accordance with [13, p.79], it is to be shown that if

$$r(t) = s(t) * u(t) \tag{A.1}$$

that is

$$r(t) = \int_{-\infty}^{\infty} s(\tau)u(t-\tau)\,d\tau \tag{A.2}$$

then

$$R(f) = S(f) \cdot U(f) \tag{A.3}$$

where the upper case signals are the Fourier transforms of the lower case signals.

$$R(f) = \int_{-\infty}^{\infty} r(t)e^{-j2\pi ft}\,dt \tag{A.4}$$

$$S(f) = \int_{-\infty}^{\infty} s(t)e^{-j2\pi ft}\,dt \tag{A.5}$$

$$U(f) = \int_{-\infty}^{\infty} u(t)e^{-j2\pi ft}\,dt \tag{A.6}$$

Substituting (A.2) in (A.4) gives

$$R(f) = \int_{-\infty}^{\infty} \left[\int_{-\infty}^{\infty} s(\tau)u(t-\tau)\,d\tau\right] e^{-j2\pi ft}\,dt \tag{A.7}$$

which by reversing the order of integration yields

$$\begin{aligned} R(f) &= \int_{-\infty}^{\infty} s(\tau)\left[\int_{-\infty}^{\infty} u(t-\tau)e^{-j2\pi ft}\,dt\right] d\tau \\ &= \int_{-\infty}^{\infty} s(\tau)\left[\int_{-\infty}^{\infty} u(z)e^{-j2\pi f(z+\tau)}\,dz\right] d\tau \\ &= \int_{-\infty}^{\infty} s(\tau)\left[\int_{-\infty}^{\infty} u(z)e^{-j2\pi fz}\,dz\right] e^{-j2\pi f\tau}\,d\tau \\ R(f) &= S(f) \cdot U(f). \end{aligned} \tag{A.8}$$

QED

B. Test Bench and Software Specifications

Table B.1.: Technical characteristics of the PMSM; according to [89].

Nominal power	60 kW
Maximum power	90 kW
Nominal torque	95 Nm
Maximum torque	200 Nm
Maximum speed	12800 rpm
Voltage	up to 430 V_{DC}
Shaft	DIN 5480-N 26 × 1.25 × 18 × 9H
Bolt hole diameter	245 mm
Length	239 mm
Weight	30 kg
Protection class	IP67, IP6k9k
Cooling	Water-glycol mixture Si-OAT 50:50, 6-8 l/min
Ambient temperature	-40 … $+85$ °C
CE conformity	Low Voltage Directive 2014/35/EU RoHS 2011/65/EU

Table B.2.: Geometric properties of the type 6207 deep groove ball bearing.

d_B	d_P	N_B	ϕ
11.1 mm	53.5 mm	9	13 °

Table B.3.: Software versions in use for data processing.

Software	Version
ArtemiS SUITE	14.2
Python	3.10.13
numpy	1.23.5
pandas	2.0.0
scipy	1.10.1
matplotlib	3.7.1
scikit-learn	1.2.2
hyperopt	0.2.7

C. Additional Exemplary Data Visualizations

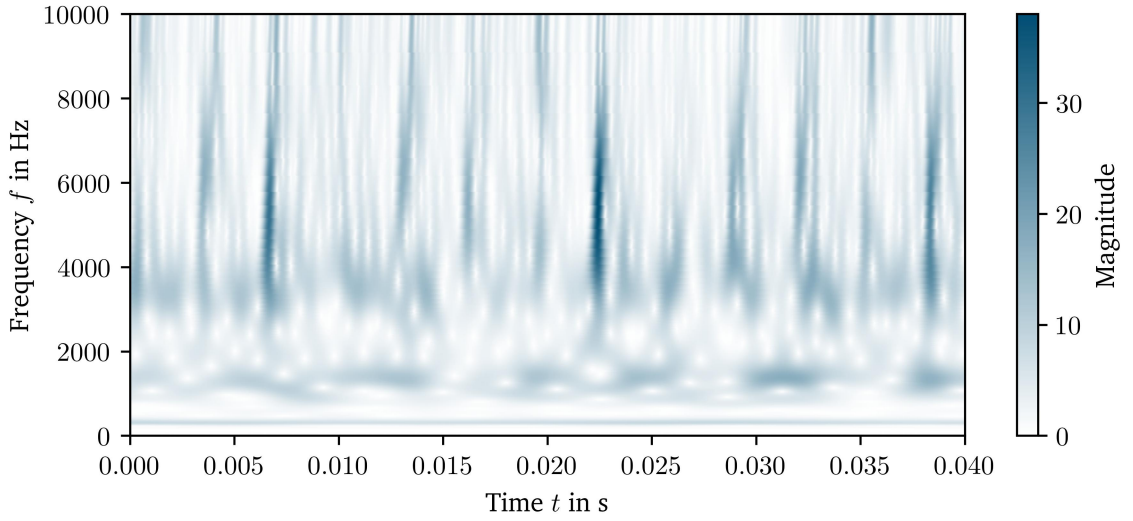

Figure C.1.: CWT for Brinell fault from experimental series A at channel 2x.

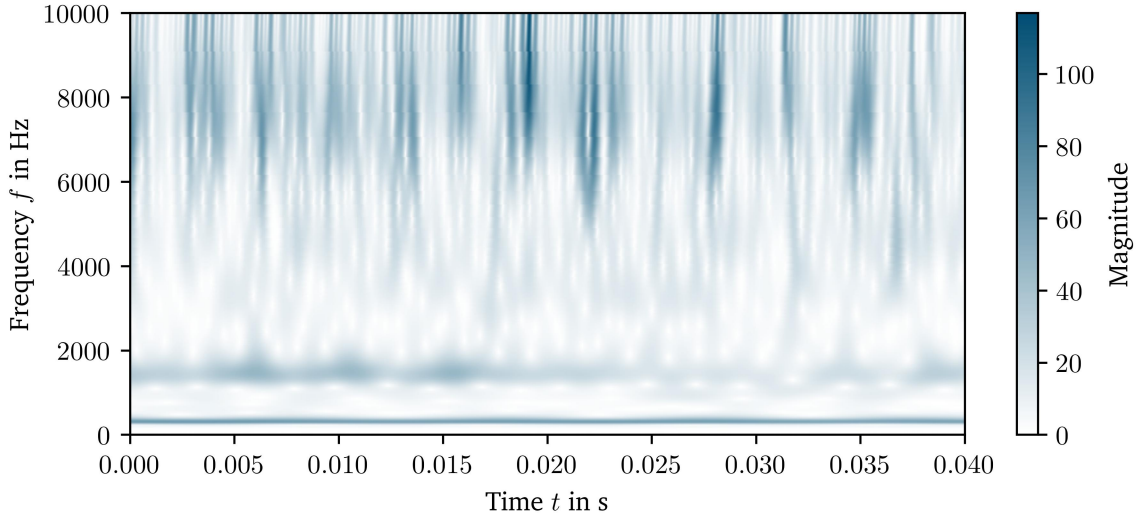

Figure C.2.: CWT for Corrosion fault from experimental series A at channel 2x.

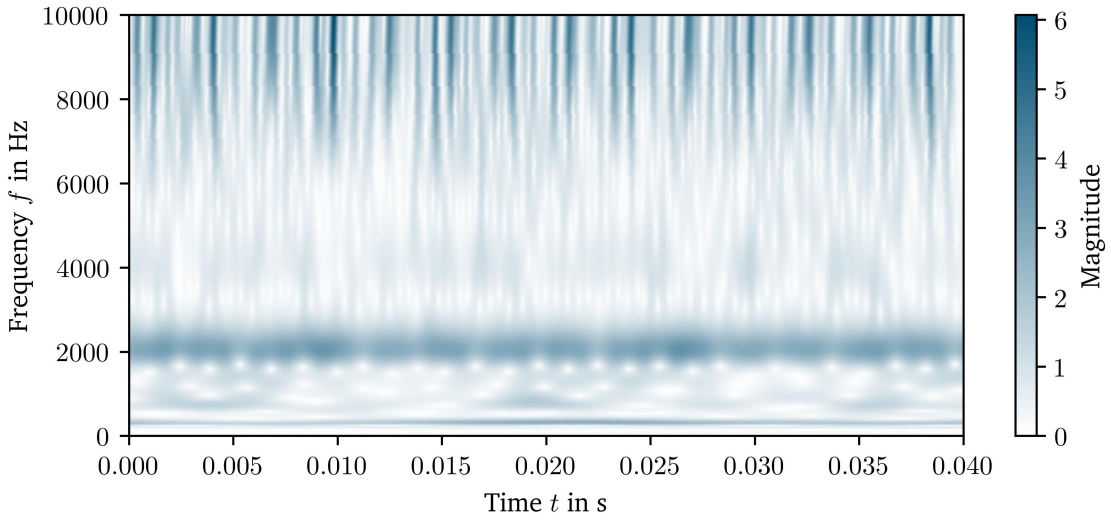

Figure C.3.: CWT for Reference bearing from experimental series A at channel 2x.

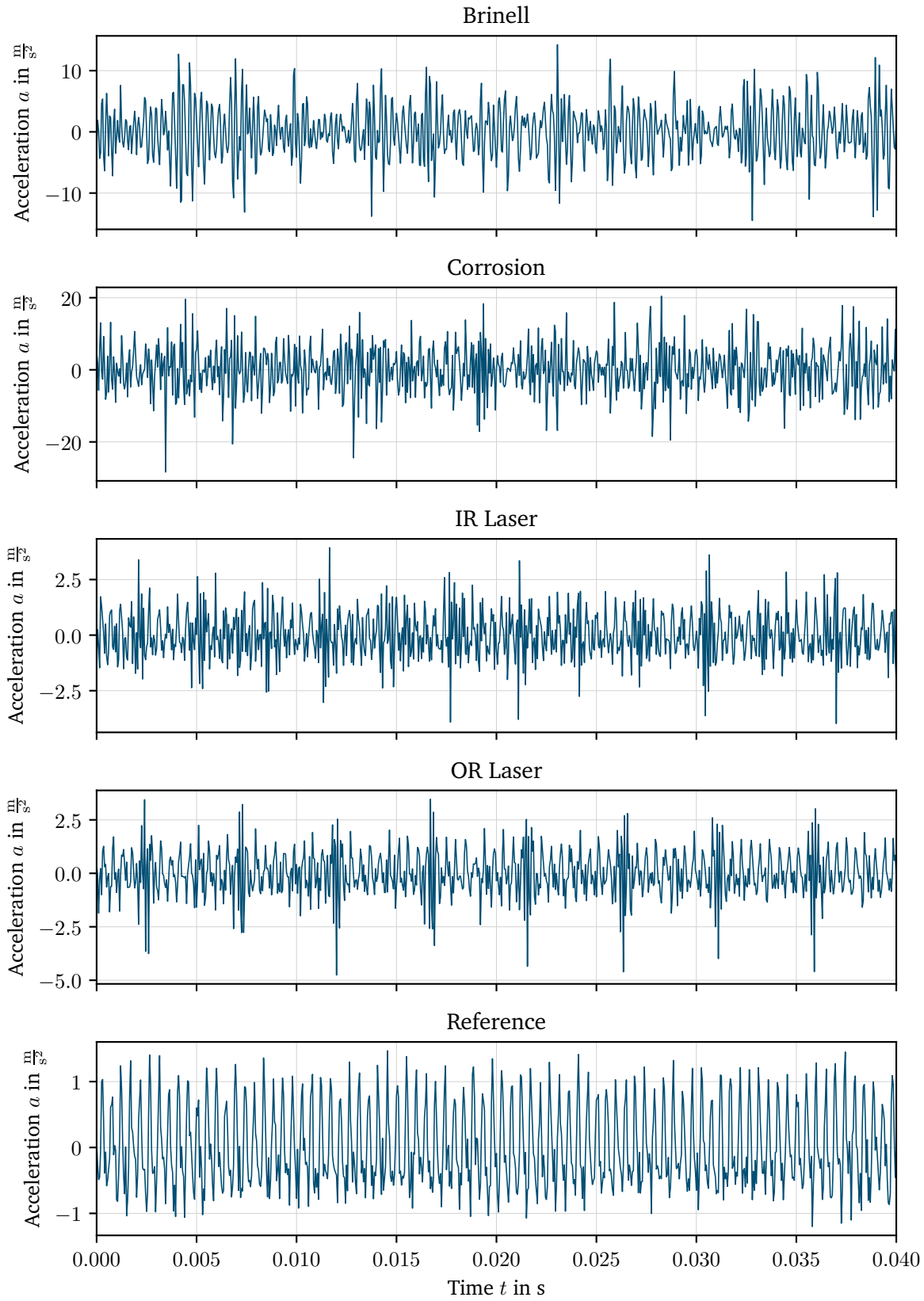

Figure C.4.: Time-domain data from experimental series A at channel 1x.

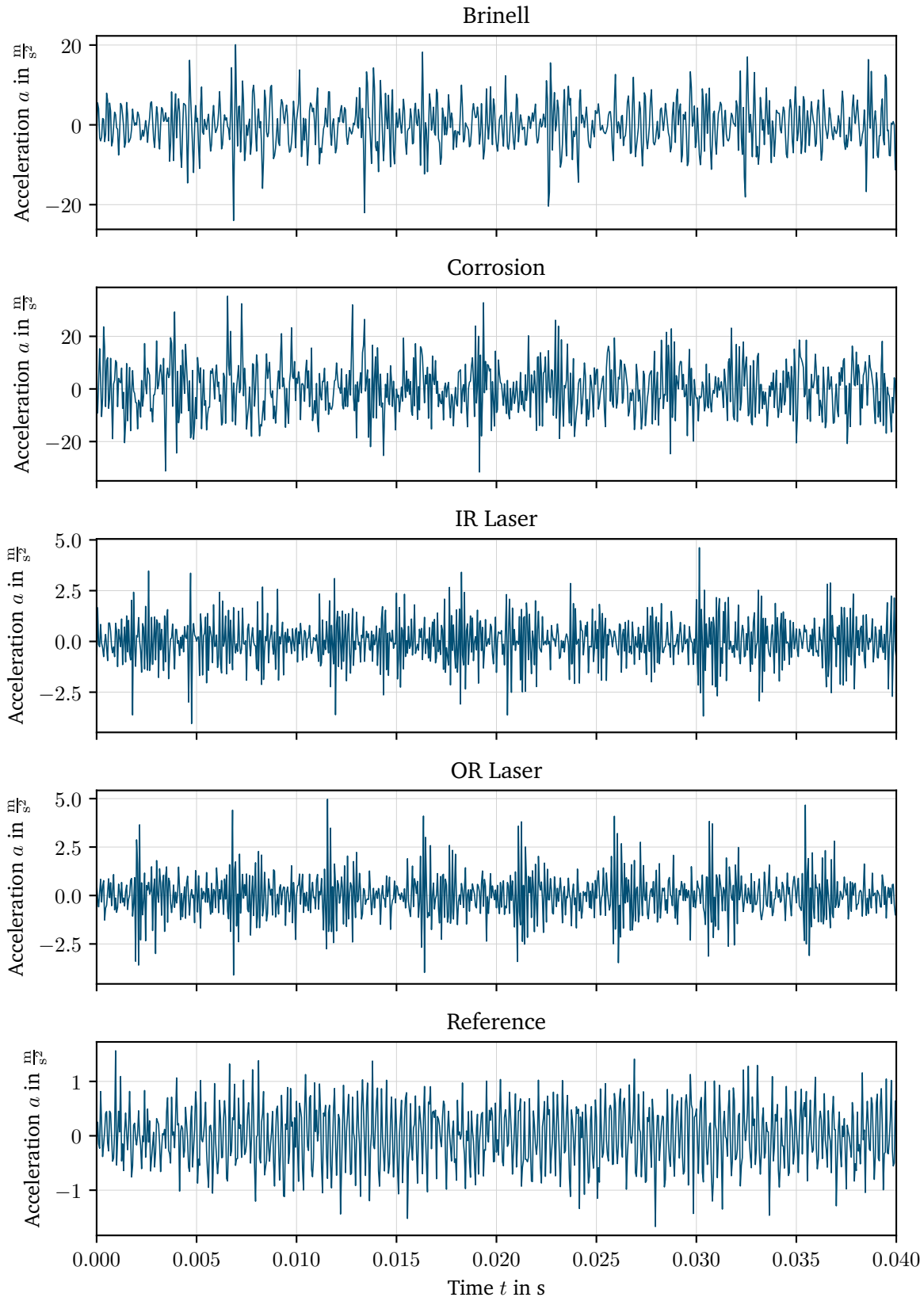

Figure C.5.: Time-domain data from experimental series A at channel 1y.

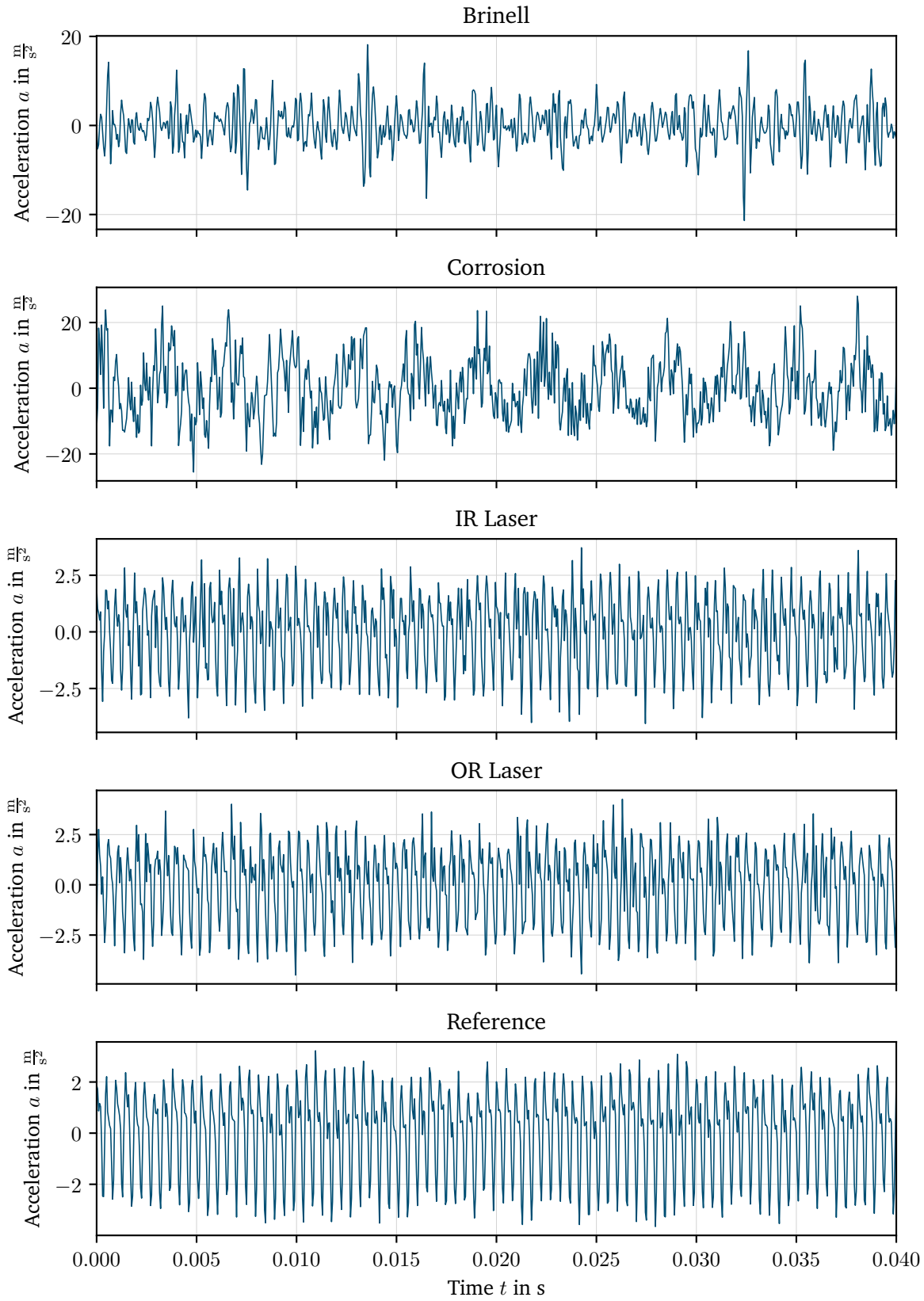

Figure C.6.: Time-domain data from experimental series A at channel 1z.

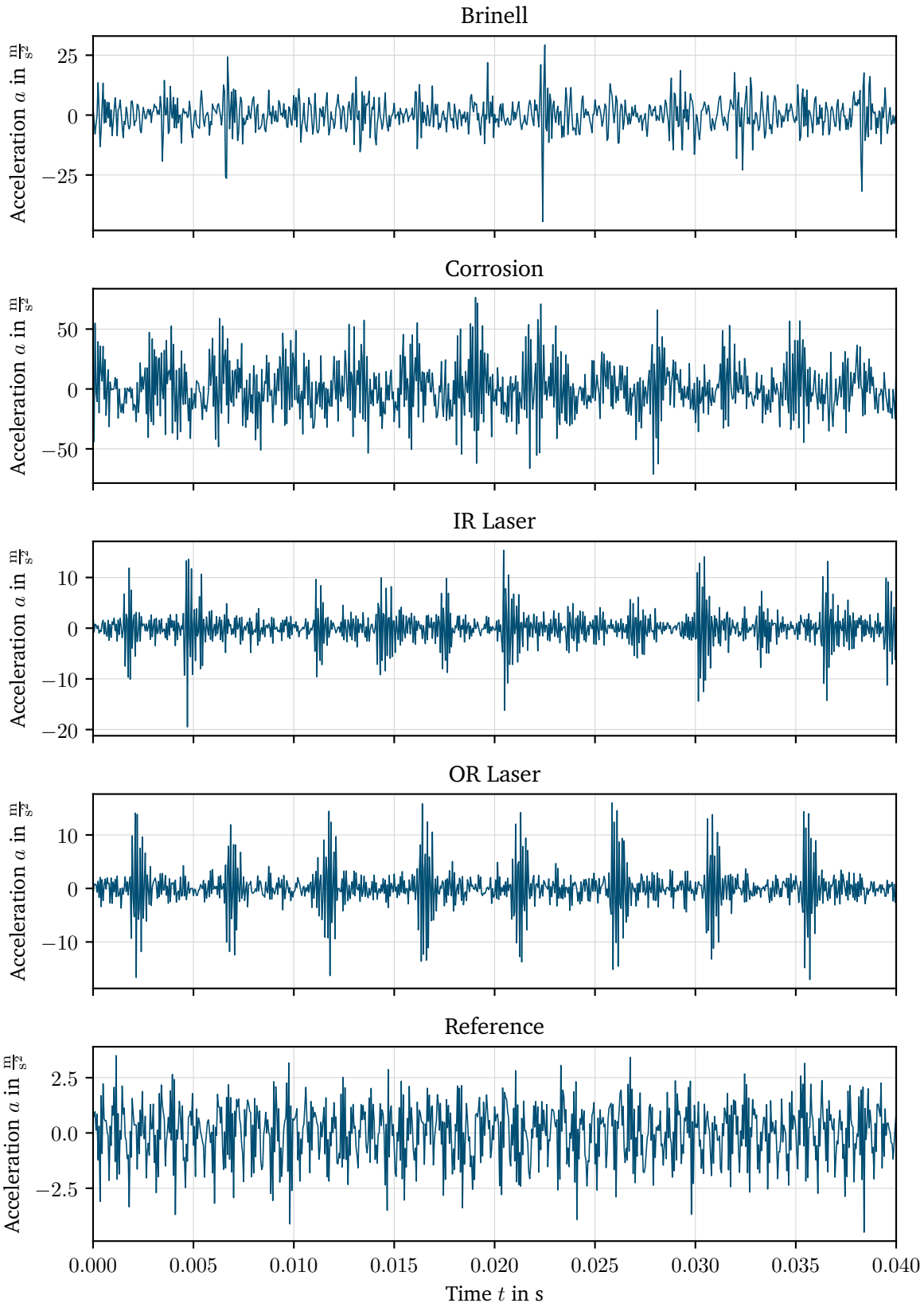

Figure C.7.: Time-domain data from experimental series A at channel 2x.

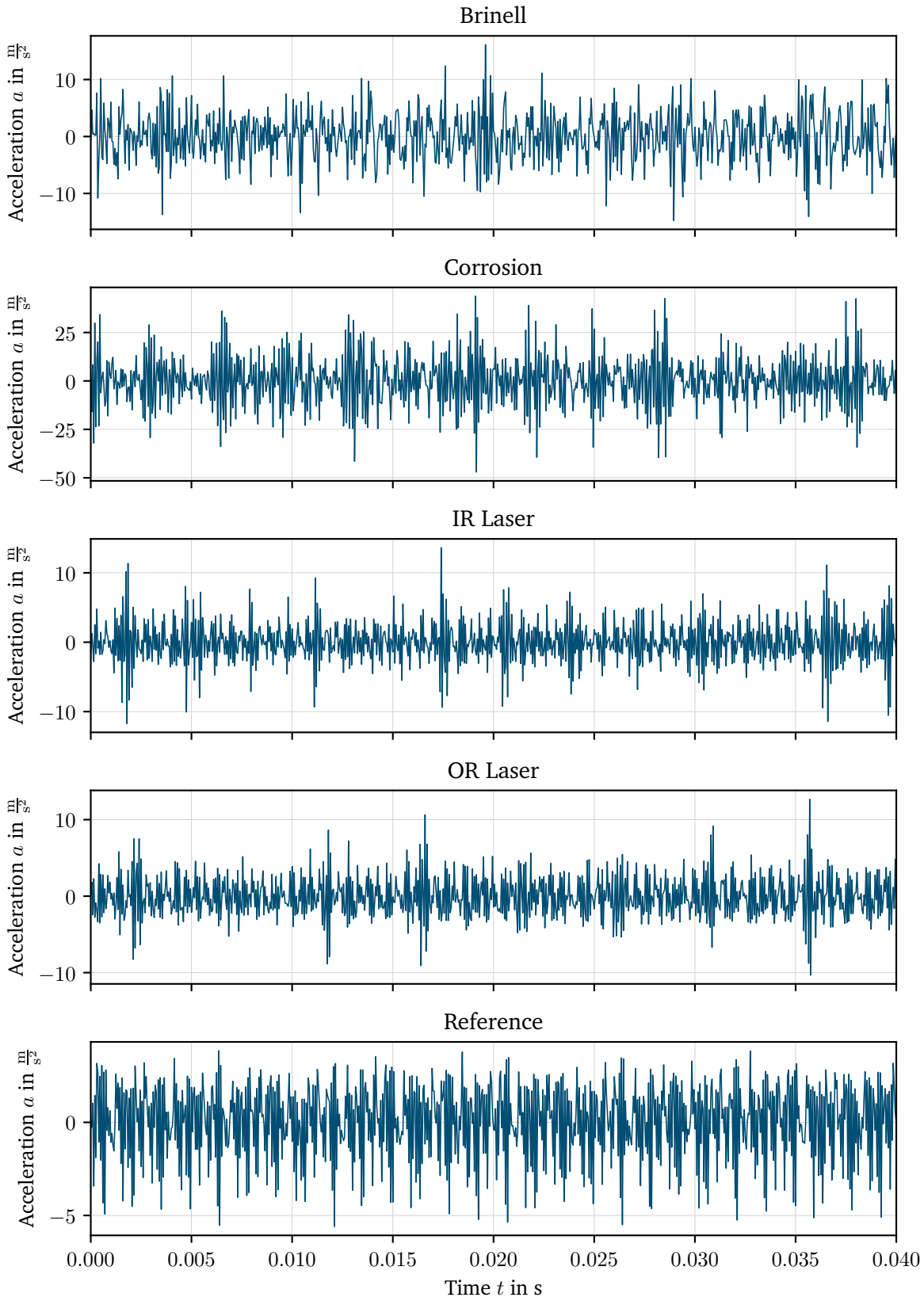

Figure C.8.: Time-domain data from experimental series A at channel 2y.

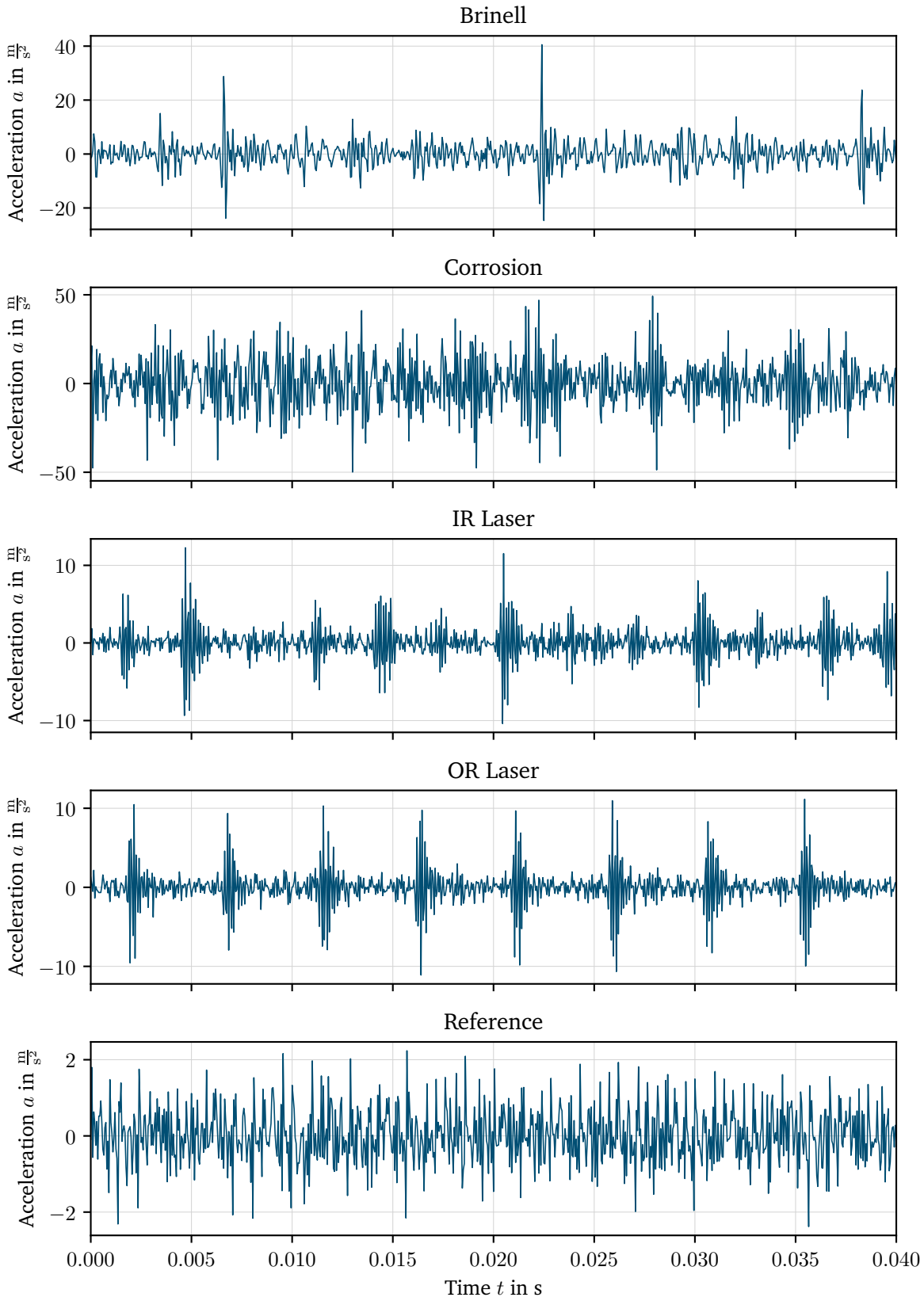

Figure C.9.: Time-domain data from experimental series A at channel 2z.

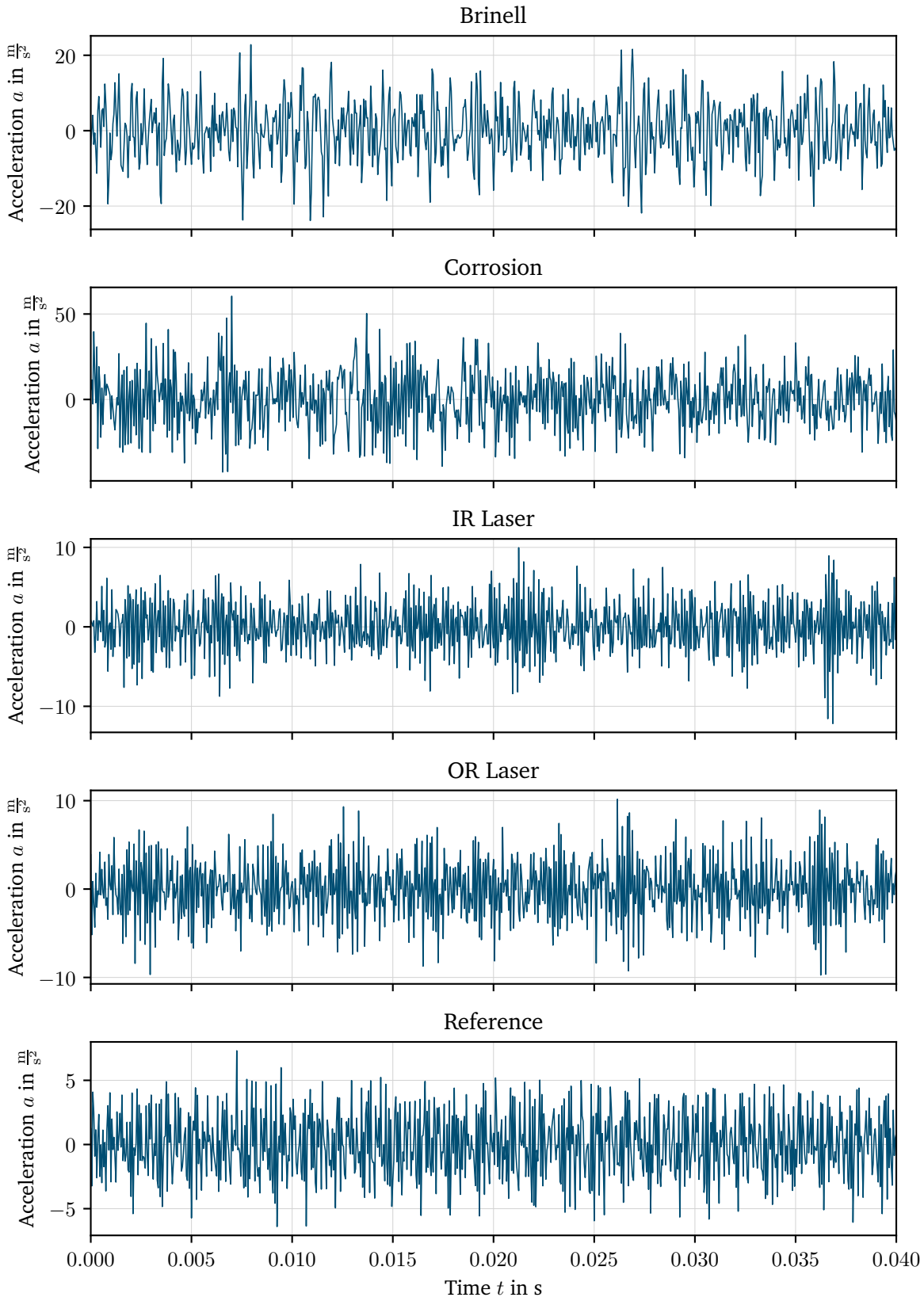

Figure C.10.: Time-domain data from experimental series A at channel 3x.

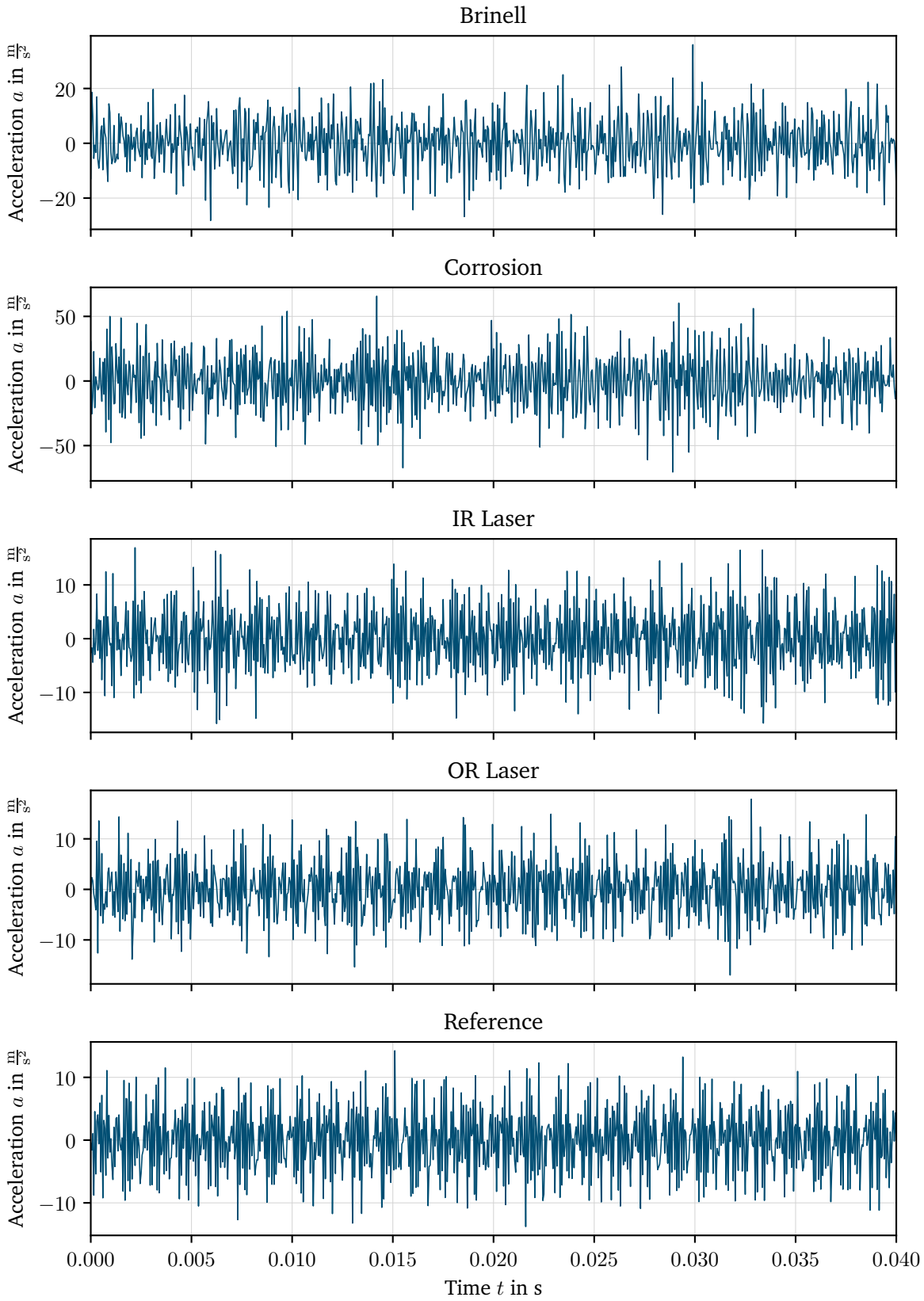

Figure C.11.: Time-domain data from experimental series A at channel 3y.

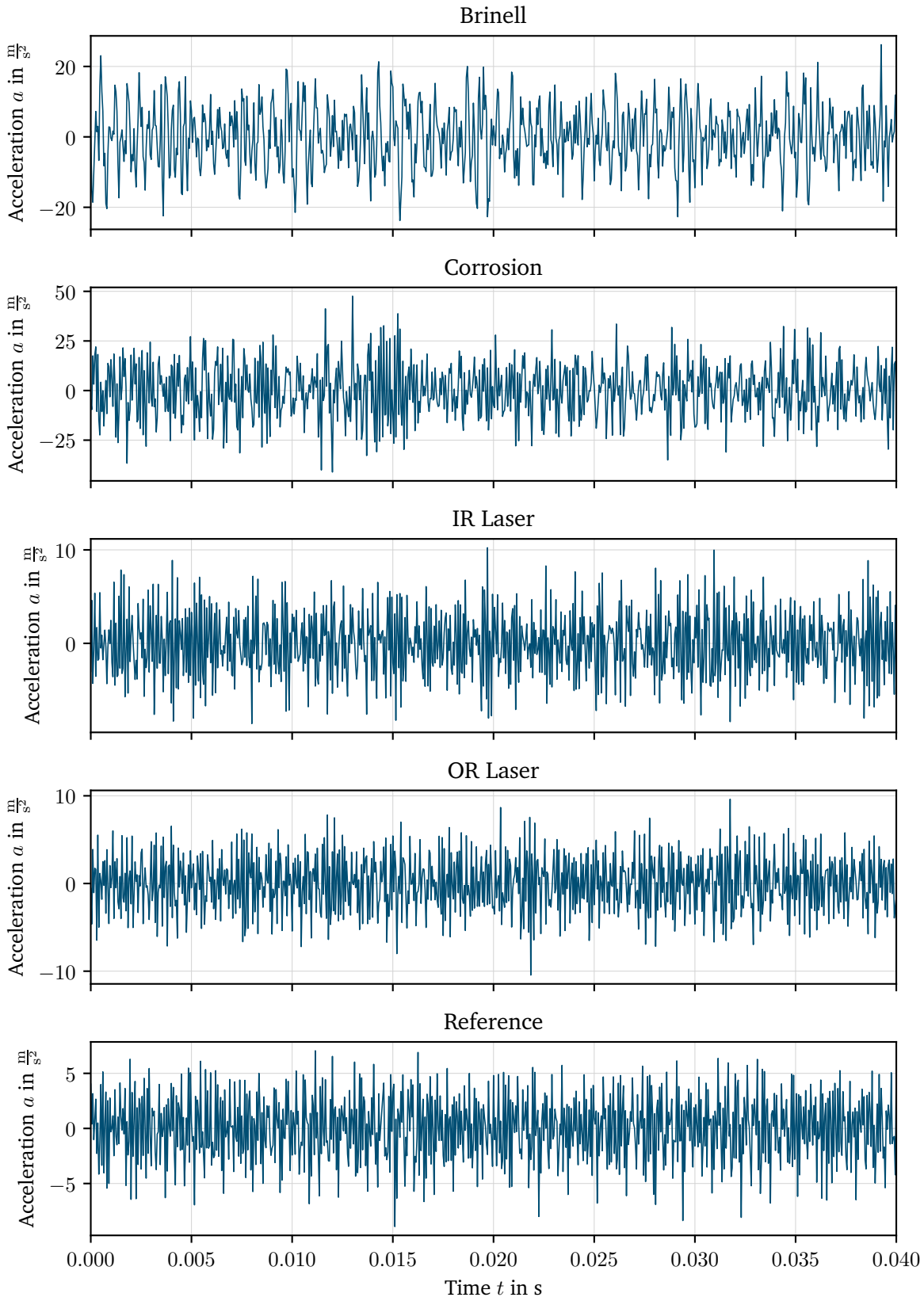

Figure C.12.: Time-domain data from experimental series A at channel 3z.

D. Supplementary ML Results

Table D.1.: Mean accuracy comparison between the different feature sets; with baseline RF.

	Mean accuracies		
Feature set	0D scenario	1D-E scenario	2D scenario
RAW_TD	99.5 %	81.0 %	45.7 %
RAW_FD	100.0 %	89.3 %	57.5 %
RAW_Lei	100.0 %	91.1 %	57.7 %
RAW_all	100.0 %	89.3 %	55.1 %
ENV_Lei	100.0 %	86.2 %	48.9 %
ENV_all	100.0 %	86.9 %	49.0 %
FB4_FD	100.0 %	86.0 %	62.7 %
FB10_FD	100.0 %	88.0 %	61.6 %
FB25_FD	100.0 %	94.6 %	66.4 %
FB50_FD	100.0 %	99.3 %	69.3 %
FB50_FD-mean	100.0 %	80.9 %	58.5 %
FB100_FD-mean	100.0 %	90.8 %	60.7 %
FB250_FD-mean	100.0 %	97.8 %	63.4 %
FB500_FD-mean	100.0 %	97.0 %	64.4 %

Bibliography

[1] H. N. Teixeira, I. Lopes, and A. C. Braga, "Condition-based maintenance implementation: A literature review," *Procedia Manufacturing*, vol. 51, pp. 228–235, 2020, ISSN: 2351-9789. DOI: 10.1016/j.promfg.2020.10.033.

[2] J. Kolerus and E. Becker, *Condition Monitoring und Instandhaltungsmanagement*. Tübingen: expert, 2022, ISBN: 978-3-8169-3489-9.

[3] A. K. Nandi and H. Ahmed, *Condition monitoring with vibration signals: Compressive sampling and learning algorithms for rotating machines*. Hoboken, NJ, USA: Wiley-IEEE Press, 2019, ISBN: 978-1-119-54462-3.

[4] Society of Automotive Engineers, "Taxonomy and definitions for terms related to driving automation systems for on-road motor vehicles," Tech. Rep. SAE J3016_20 2104, 2021.

[5] R. Vosooghi, J. Kamel, J. Puchinger, V. Leblond, and M. Jankovic, "Robo-taxi service fleet sizing: Assessing the impact of user trust and willingness-to-use," *Transportation*, vol. 46, no. 6, pp. 1997–2015, Dec. 2019, ISSN: 1572-9435. DOI: 10.1007/s11116-019-10013-x.

[6] K. Gorelik, A. Kilic, and R. Obermaisser, "Range prediction and extension for automated electric vehicles with fail-operational powertrain: Optimal and safety based torque distribution for multiple traction motors," in *2018 Annual IEEE International Systems Conference (SysCon)*, Vancouver, BC: IEEE, Apr. 2018, pp. 1–7, ISBN: 978-1-5386-3664-0. DOI: 10.1109/SYSCON.2018.8369519.

[7] A. Kilic, J. Faßnacht, T. Shen, and C. Thulfaut, "Fail-operational powertrain for future mobility," in *Der Antrieb von morgen 2019*, J. Liebl, Ed., Wiesbaden: Springer Fachmedien Wiesbaden, 2019, pp. 221–236, ISBN: 978-3-658-26056-9. DOI: 10.1007/978-3-658-26056-9_14.

[8] T. Shen, *Diagnosis of the powertrain systems for autonomous electric vehicles*, ser. Wissenschaftliche Reihe Fahrzeugtechnik Universität Stuttgart. Wiesbaden: Springer Fachmedien Wiesbaden, 2022, ISBN: 978-3-658-36992-7. DOI: 10.1007/978-3-658-36992-7.

[9] A. Bonnett and C. Yung, "Increased efficiency versus increased reliability," *IEEE Industry Applications Magazine*, vol. 14, no. 1, pp. 29–36, Jan. 2008, ISSN: 1077-2618. DOI: 10.1109/MIA.2007.909802.

[10] L. Szabo, D. Fodorean, and A. Vasilache, "Bearing fault detection of electrical machines used in automotive applications," in *2016 XXII International Conference on Electrical Machines (ICEM)*, Lausanne, Switzerland: IEEE, Sep. 2016, pp. 2184–2190, ISBN: 978-1-5090-2538-1. DOI: 10.1109/ICELMACH.2016.7732825.

[11] International Organization for Standardization, *ISO 281: Rolling bearings – Dynamic load ratings and rating life*, Feb. 2007.

[12] D. Franke, *Wälzlagerdiagnose an Maschinensätzen: Diagnose und Überwachung von Wälzlagerfehlern und -schäden*. Berlin, Heidelberg: Springer Berlin Heidelberg, 2022, ISBN: 978-3-662-62620-7. DOI: 10.1007/978-3-662-62620-7.

[13] R. B. Randall, *Vibration-based condition monitoring: Industrial, aerospace, and automotive applications*. Chichester, West Sussex, U.K. ; Hoboken, N.J: Wiley, 2011, ISBN: 978-0-470-74785-8.

[14] Y. Lei, N. Li, and X. Li, *Big Data-driven intelligent fault diagnosis and prognosis for mechanical systems*. Singapore: Springer Nature Singapore, 2023, ISBN: 9789811691300. DOI: 10.1007/978-981-16-9131-7.

[15] German Institute for Standardisation Registered Association, *DIN EN 13306: Instandhaltung – Begriffe der Instandhaltung*, Feb. 2018.

[16] J. Endrenyi, S. Aboresheid, R. Allan, G. Anders, S. Asgarpoor, R. Billinton, N. Chowdhury, E. Dialynas, M. Fipper, R. Fletcher, C. Grigg, J. McCalley, S. Meliopoulos, T. Mielnik, P. Nitu, N. Rau, N. Reppen, L. Salvaderi, A. Schneider, and C. Singh, "The present status of maintenance strategies and the impact of maintenance on reliability," *IEEE Transactions on Power Systems*, vol. 16, no. 4, pp. 638–646, Nov. 2001, ISSN: 0885-8950. DOI: 10.1109/59.962408.

[17] M. Schenk, Ed., *Instandhaltung technischer Systeme: Methoden und Werkzeuge zur Gewährleistung eines sicheren und wirtschaftlichen Anlagenbetriebs*. Berlin, Heidelberg: Springer Berlin Heidelberg, 2010, ISBN: 978-3-642-03949-2. DOI: 10.1007/978-3-642-03949-2.

[18] N.-H. Kim, D. An, and J.-H. Choi, *Prognostics and health management of engineering systems*. Cham: Springer International Publishing, 2017, ISBN: 978-3-319-44742-1. DOI: 10.1007/978-3-319-44742-1.

[19] T. Zonta, C. A. da Costa, R. da Rosa Righi, M. J. de Lima, E. S. da Trindade, and G. P. Li, "Predictive maintenance in the Industry 4.0: A systematic literature review," *Computers & Industrial Engineering*, vol. 150, p. 106 889, Dec. 2020, ISSN: 0360-8352. DOI: 10.1016/j.cie.2020.106889.

[20] P. Albrecht, J. Appiarius, R. McCoy, E. Owen, and D. Sharma, "Assessment of the reliability of motors in utility applications - updated," *IEEE Transactions on Energy Conversion*, vol. EC-1, no. 1, pp. 39–46, Mar. 1986, ISSN: 0885-8969. DOI: 10.1109/TEC.1986.4765668.

[21] P. Tchakoua, R. Wamkeue, M. Ouhrouche, F. Slaoui-Hasnaoui, T. Tameghe, and G. Ekemb, "Wind turbine condition monitoring: State-of-the-art review, new trends, and future challenges," *Energies*, vol. 7, no. 4, pp. 2595–2630, Apr. 2014, ISSN: 1996-1073. DOI: 10.3390/en7042595.

[22] F. P. García Márquez, A. M. Tobias, J. M. Pinar Pérez, and M. Papaelias, "Condition monitoring of wind turbines: Techniques and methods," *Renewable Energy*, vol. 46, pp. 169–178, Oct. 2012, ISSN: 0960-1481. DOI: 10.1016/j.renene.2012.03.003.

[23] D. Goyal and B. S. Pabla, "The vibration monitoring methods and signal processing techniques for structural health monitoring: A review," *Archives of Computational Methods in Engineering*, vol. 23, no. 4, pp. 585–594, Dec. 2016, ISSN: 1886-1784. DOI: 10.1007/s11831-015-9145-0.

[24] M. Andrejašic, "Mems accelerometers," in *University of Ljubljana. Faculty for mathematics and physics, Department of physics, Seminar*, vol. 49, Mar. 2008.

[25] F. König, J. Marheineke, G. Jacobs, C. Sous, M. J. Zuo, and Z. Tian, "Data-driven wear monitoring for sliding bearings using acoustic emission signals and long short-term memory neural networks," *Wear*, vol. 476, p. 203 616, Jul. 2021, ISSN: 0043-1648. DOI: 10.1016/j.wear.2021.203616.

[26] D. Cornel, F. Gutiérrez Guzmán, G. Jacobs, and S. Neumann, "Condition monitoring of roller bearings using acoustic emission," *Wind Energy Science*, vol. 6, no. 2, pp. 367–376, Mar. 2021, ISSN: 2366-7451. DOI: 10.5194/wes-6-367-2021.

[27] T. Wagner, "A framework for current signal based bearing fault detection of permanent magnet synchronous motors," Dissertation, Fulda University of Applied Sciences, Fulda, 2023.

[28] H. D. M. de Azevedo, A. M. Araújo, and N. Bouchonneau, "A review of wind turbine bearing condition monitoring: State of the art and challenges," *Renewable and Sustainable Energy Reviews*, vol. 56, pp. 368–379, Apr. 2016, ISSN: 1364-0321. DOI: 10.1016/j.rser.2015.11.032.

[29] G. Martin, "Die Wälzlagerimpedanz als Werkzeug zur Untersuchung von Oberflächenabweichungen in Wälzlagern," Dissertation, TU Darmstadt, Darmstadt, 2021.

[30] G. Martin, F. M. Becker, and E. Kirchner, "A novel method for diagnosing rolling bearing surface damage by electric impedance analysis," *Tribology International*, vol. 170, p. 107 503, Jun. 2022, ISSN: 0301-679X. DOI: 10.1016/j.triboint.2022.107503.

[31] International Organization for Standardization, *ISO 15243: Rolling bearings – Damage and failures – Terms, characteristics and causes*, Mar. 2017.

[32] A. Kapoor, I. Salehi, and A. M. S. Asih, "Rolling contact fatigue (RCF)," in *Encyclopedia of Tribology*, Q. J. Wang and Y.-W. Chung, Eds., Boston, MA: Springer US, 2013, pp. 2904–2910, ISBN: 978-0-387-92897-5. DOI: 10.1007/978-0-387-92897-5_287.

[33] H. Jünemann, M. Laible, E. M. Laukotka, K. Michaelis, and H. Weber, *Tribometrie: Prüf- und Meßtechnik für Reibungs-, Verschleiß- und Schmierungsvorgänge*, ser. Kontakt & Studium. Renningen-Malmsheim: Expert-Verlag, 1997, ISBN: 978-3-8169-1445-7.

[34] V. Schneider, C. Behrendt, P. Höltje, D. Cornel, F. M. Becker-Dombrowsky, S. Puchtler, F. Gutiérrez Guzmán, B. Ponick, G. Jacobs, and E. Kirchner, "Electrical bearing damage, a problem in the nano- and macro-range," *Lubricants*, vol. 10, no. 8, p. 194, Aug. 2022, ISSN: 2075-4442. DOI: 10.3390/lubricants10080194.

[35] T. A. Harris, *Rolling bearing analysis*, 4th ed. New York: Wiley, 2001, ISBN: 978-0-471-35457-4.

[36] H. Czichos and K.-H. Habig, Eds., *Tribologie-Handbuch: Tribometrie, Tribomaterialien, Tribotechnik*. Wiesbaden: Springer Fachmedien Wiesbaden, 2020, ISBN: 978-3-658-29484-7. DOI: 10.1007/978-3-658-29484-7.

[37] Association of German Engineers, *VDI 3832: Measurement of structure-borne sound of rolling element bearings in machines and plants for evaluation of condition*, Düsseldorf, Apr. 2013.

[38] J. I. Taylor, *The vibration analysis handbook*, 1st ed. Tampa, FL: Vibration Consultants, 1994, ISBN: 978-0-9640517-0-6.

[39] R. B. Randall and J. Antoni, "Rolling element bearing diagnostics—A tutorial," *Mechanical Systems and Signal Processing*, vol. 25, no. 2, pp. 485–520, Feb. 2011, ISSN: 0888-3270. DOI: 10.1016/j.ymssp.2010.07.017.

[40] International Organization for Standardization, *ISO 20816-1: Mechanical vibration – Measurement and evaluation of machine vibration – Part 1: General guidelines*, Nov. 2016.

[41] S. Schwendemann, Z. Amjad, and A. Sikora, "A survey of machine-learning techniques for condition monitoring and predictive maintenance of bearings in grinding machines," *Computers in Industry*, vol. 125, p. 103 380, Feb. 2021, ISSN: 0166-3615. DOI: 10.1016/j.compind.2020.103380.

[42] M. Hakim, A. A. B. Omran, A. N. Ahmed, M. Al-Waily, and A. Abdellatif, "A systematic review of rolling bearing fault diagnoses based on deep learning and transfer learning: Taxonomy, overview, application, open challenges, weaknesses and recommendations," *Ain Shams Engineering Journal*, p. 101 945, Sep. 2022, ISSN: 2090-4479. DOI: 10.1016/j.asej.2022.101945.

[43] H. Qiu, J. Lee, J. Lin, and G. Yu, "Wavelet filter-based weak signature detection method and its application on rolling element bearing prognostics," *Journal of Sound and Vibration*, vol. 289, no. 4-5, pp. 1066–1090, Feb. 2006, ISSN: 0022-460X. DOI: 10.1016/j.jsv.2005.03.007.

[44] P. Nectoux, R. Gouriveau, K. Medjaher, E. Ramasso, B. Chebel-Morello, N. Zerhouni, and C. Varnier, "PRONOSTIA: An experimental platform for bearings accelerated degradation tests," in *Conference on Prognostics and Health Management.*, Jun. 2012, pp. 1–8.

[45] B. Wang, Y. Lei, N. Li, and N. Li, "A hybrid prognostics approach for estimating remaining useful life of rolling element bearings," *IEEE Transactions on Reliability*, vol. 69, no. 1, pp. 401–412, Mar. 2020, ISSN: 0018-9529, 1558-1721. DOI: 10.1109/TR.2018.2882682.

[46] Case Western Reserve University, *CWRU Bearing Data Center*, URL: https://engineering.case.edu/bearingdatacenter/, accessed on 3 Jul. 2023.

[47] E. Bechhoefer, *MFPT Fault Data Sets*, URL: https://www.mfpt.org/fault-data-sets/, accessed on 13 Dec. 2023.

[48] C. Lessmeier, J. Kimotho, D. Zimmer, and W. Sextro, "Condition monitoring of bearing damage in electromechanical drive systems by using motor current signals of electric motors: A benchmark data set for data-driven classification," Data available at URL: https://mb.uni-paderborn.de/kat/forschung/kat-datacenter/bearing-datacenter/, accessed on 13 Dec. 2023, Jul. 2016.

[49] D. Sacerdoti, M. Strozzi, and C. Secchi, "A comparison of signal analysis techniques for the diagnostics of the IMS rolling element bearing dataset," *Applied Sciences*, vol. 13, no. 10, p. 5977, May 2023, ISSN: 2076-3417. DOI: 10.3390/app13105977.

[50] W. A. Smith and R. B. Randall, "Rolling element bearing diagnostics using the Case Western Reserve University data: A benchmark study," *Mechanical Systems and Signal Processing*, vol. 64-65, pp. 100–131, Dec. 2015, ISSN: 0888-3270. DOI: 10.1016/j.ymssp.2015.04.021.

[51] D. Neupane and J. Seok, "Bearing fault detection and diagnosis using case western reserve university dataset with deep learning approaches: A review," *IEEE Access*, vol. 8, pp. 93 155–93 178, 2020, ISSN: 2169-3536. DOI: 10.1109/ACCESS.2020.2990528.

[52] G. Rebala, A. Ravi, and S. Churiwala, *An introduction to machine learning*. Cham: Springer International Publishing, 2019, ISBN: 978-3-030-15729-6. DOI: 10.1007/978-3-030-15729-6.

[53] B. Mahesh, "Machine learning algorithms—A review," *International Journal of Science and Research*, vol. 9, no. 1, pp. 381–386, Jan. 2019, ISSN: 2319-7064. DOI: 10.21275/ART20203995.

[54] S. Matzka, *Künstliche Intelligenz in den Ingenieurwissenschaften: Maschinelles Lernen verstehen und bewerten*. Wiesbaden: Springer Fachmedien Wiesbaden, 2021, ISBN: 978-3-658-34641-6. DOI: 10.1007/978-3-658-34641-6.

[55] N. M. Nawi, W. H. Atomi, and M. Rehman, "The effect of data pre-processing on optimized training of artificial neural networks," *Procedia Technology*, vol. 11, pp. 32–39, 2013, ISSN: 2212-0173. DOI: 10.1016/j.protcy.2013.12.159.

[56] M. Kubat, *An introduction to machine learning*, 3rd ed. Springer Nature Switzerland, 2021, OCLC: 1269481499, ISBN: 978-3-030-81935-4.

[57] I. Goodfellow, Y. Bengio, and A. Courville, *Deep learning*, ser. Adaptive computation and machine learning series. MIT Press, 2016, ISBN: 978-0-262-33737-3.

[58] Z. An, S. Li, J. Wang, Y. Xin, and K. Xu, "Generalization of deep neural network for bearing fault diagnosis under different working conditions using multiple kernel method," *Neurocomputing*, vol. 352, pp. 42–53, Aug. 2019, ISSN: 0925-2312. DOI: 10.1016/j.neucom.2019.04.010.

[59] B. Yang, Y. Lei, F. Jia, and S. Xing, "An intelligent fault diagnosis approach based on transfer learning from laboratory bearings to locomotive bearings," *Mechanical Systems and Signal Processing*, vol. 122, pp. 692–706, May 2019, ISSN: 0888-3270. DOI: 10.1016/j.ymssp.2018.12.051.

[60] S. J. Pan and Q. Yang, "A survey on transfer learning," *IEEE Transactions on Knowledge and Data Engineering*, vol. 22, no. 10, pp. 1345–1359, Oct. 2010, ISSN: 1041-4347. DOI: 10.1109/TKDE.2009.191.

[61] S. Mehringskötter, "Verschleiß- und Lebensdauerprognose unter Berücksichtigung variabler zukünftiger Betriebszustände," Dissertation, TU Darmstadt, Darmstadt, 2022.

[62] H. Hanselka, J. Bös, and T. Nestorović, "Maschinenakustik," in *Dubbel*, K.-H. Grote, B. Bender, and D. Göhlich, Eds., Berlin, Heidelberg: Springer Berlin Heidelberg, 2018, pp. 1043–1056, ISBN: 978-3-662-54805-9. DOI: 10.1007/978-3-662-54805-9_95.

[63] R. Allemang and P. Avitabile, Eds., *Handbook of experimental structural dynamics*. New York, NY: Springer New York, 2022, ISBN: 978-1-4614-4547-0. DOI: 10.1007/978-1-4614-4547-0.

[64] C. M. Bishop, *Pattern recognition and machine learning*, ser. Information science and statistics. New York: Springer, 2006, ISBN: 978-0-387-31073-2.

[65] A. Géron, *Hands-on machine learning with scikit-learn, keras, and tensorflow*. Sebastopol, CA: O'Reilly Media, Inc., 2019, OCLC: 1153040518, ISBN: 978-1-4920-3263-2.

[66] L. Yang and A. Shami, "On hyperparameter optimization of machine learning algorithms: Theory and practice," *Neurocomputing*, vol. 415, pp. 295–316, Nov. 2020, ISSN: 0925-2312. DOI: 10.1016/j.neucom.2020.07.061.

[67] P. Probst, A.-L. Boulesteix, and B. Bischl, "Tunability: Importance of hyperparameters of machine learning algorithms," *Journal of Machine Learning Research*, vol. 20, 53:1–53:32, 2018.

[68] J. Snoek, H. Larochelle, and R. P. Adams, "Practical bayesian optimization of machine learning algorithms," in *Advances in Neural Information Processing Systems*, F. Pereira, C. J. Burges, L. Bottou, and K. Q. Weinberger, Eds., vol. 25, Curran Associates, Inc., 2012.

[69] J. Bergstra, R. Bardenet, Y. Bengio, and B. Kégl, "Algorithms for hyper-parameter optimization," in *Advances in Neural Information Processing Systems*, J. Shawe-Taylor, R. Zemel, P. Bartlett, F. Pereira, and K. Q. Weinberger, Eds., vol. 24, Curran Associates, Inc., 2011.

[70] Y. Lei, Z. He, and Y. Zi, "A new approach to intelligent fault diagnosis of rotating machinery," *Expert Systems with Applications*, vol. 35, no. 4, pp. 1593–1600, Nov. 2008, ISSN: 0957-4174. DOI: 10.1016/j.eswa.2007.08.072.

[71] Y. Lei, *Intelligent fault diagnosis and remaining useful life prediction of rotating machinery*. Oxford, United Kingdom: Butterworth-Heinemann Ltd, : Xi'an Jiaotong University Press, 2017, OCLC: ocn952647304, ISBN: 978-0-12-811534-3.

[72] C. Bienefeld, F. M. Becker-Dombrowsky, E. Shatri, and E. Kirchner, "Investigation of feature engineering methods for domain-knowledge-assisted bearing fault diagnosis," *Entropy*, vol. 25, no. 9, p. 1278, Aug. 2023, ISSN: 1099-4300. DOI: 10.3390/e25091278.

[73] X. Wang, Y. Zheng, Z. Zhao, and J. Wang, "Bearing fault diagnosis based on statistical locally linear embedding," *Sensors*, vol. 15, no. 7, pp. 16 225–16 247, Jul. 2015, ISSN: 1424-8220. DOI: 10.3390/s150716225.

[74] K. F. Tom, "A primer on vibrational ball bearing feature generation for prognostics and diagnostics algorithms," *Sensors and Electron Devices, ARL*, Mar. 2015.

[75] V. K. Golbaghi, M. Shahbazian, B. Moslemi, and G. Rashed, "Rolling element bearing condition monitoring based on vibration analysis using statistical parameters of discrete wavelet coefficients and neural networks," *International Journal of Automation and Smart Technology*, vol. 7, no. 2, pp. 61–69, 2017. DOI: 10.5875/ausmt.v7i2.1201.

[76] C. Grover and N. Turk, "Optimal statistical feature subset selection for bearing fault detection and severity estimation," *Shock and Vibration*, vol. 2020, pp. 1–18, Aug. 2020, ISSN: 1875-9203. DOI: 10.1155/2020/5742053.

[77] P. H. Jain and S. P. Bhosle, "Study of effects of radial load on vibration of bearing using time-domain statistical parameters," *IOP Conference Series: Materials Science and Engineering*, vol. 1070, no. 1, p. 012 130, Feb. 2021, ISSN: 1757-899X. DOI: 10.1088/1757-899X/1070/1/012130.

[78] J.-J. Saucedo-Dorantes, I. Zamudio-Ramirez, J. Cureno-Osornio, R. A. Osornio-Rios, and J. A. Antonino-Daviu, "Condition monitoring method for the detection of fault graduality in outer race bearing based on vibration-current fusion, statistical features and neural network," *Applied Sciences*, vol. 11, no. 17, p. 8033, Aug. 2021, ISSN: 2076-3417. DOI: 10.3390/app11178033.

[79] A. Brandt, *Noise and vibration analysis: Signal analysis and experimental procedures*, 1st ed. Wiley, Feb. 2011, ISBN: 978-0-470-74644-8.

[80] J. G. Proakis and D. G. Manolakis, *Digital signal processing: principles, algorithms, and applications*, 3rd ed. Upper Saddle River, N.J: Prentice Hall, 1996, ISBN: 978-0-13-373762-2.

[81] C. Bienefeld, A. Vogt, M. Kacmar, and E. Kirchner, "Feature-Engineering für die Zustandsüberwachung von Wälzlagern mittels maschinellen Lernens," *Tribologie und Schmierungstechnik*, vol. 68, no. 6, pp. 5–11, Dec. 2021, ISSN: 0724-3472. DOI: 10.24053/TuS-2021-0032.

[82] C. Bienefeld, E. Kirchner, A. Vogt, and M. Kacmar, "On the importance of temporal information for remaining useful life prediction of rolling bearings using a random forest regressor," *Lubricants*, vol. 10, no. 4, p. 67, Apr. 2022, ISSN: 2075-4442. DOI: 10.3390/lubricants10040067.

[83] S. W. Smith, *The scientist and engineer's guide to digital signal processing*, 2nd edition. San Diego (Calif.): California Technical Pub., 1999, OCLC: 493473234, ISBN: 978-0-9660176-7-0.

[84] A. Mertins, *Signaltheorie*. Wiesbaden: Vieweg+Teubner, 2010, ISBN: 978-3-8348-9381-9. DOI: 10.1007/978-3-8348-9381-9.

[85] J. Morlet, "Sampling theory and wave propagation," in *Issues in acoustic signal — image processing and recognition*, C. H. Chen, Ed., Berlin, Heidelberg: Springer Berlin Heidelberg, 1983, pp. 233–261, ISBN: 978-3-642-82002-1. DOI: 10.1007/978-3-642-82002-1_12.

[86] L. Cremer, M. Heckl, and B. Petersson, *Structure-borne sound*. Berlin, Heidelberg: Springer Berlin Heidelberg, 2005, ISBN: 978-3-540-26514-6. DOI: 10.1007/b137728.

[87] P. Zeller, Ed., *Handbuch Fahrzeugakustik*. Wiesbaden: Vieweg+Teubner Verlag, 2012, ISBN: 978-3-8348-8657-6. DOI: 10.1007/978-3-8348-8657-6.

[88] PCB Piezotronics, *Accelerometer, ICP, Triaxial, Model 356A15*, URL: https://www.pcb.com/products?m=356a15, accessed on 22 Sep. 2023.

[89] Bosch Mobility, *Separate motor-generator for off-highway applications*, URL: https://www.bosch-mobility.com/en/solutions/electric-motors/separate-motor-generator-ohw/, accessed on 12 Sep. 2023.

[90] Bosch Mobility, *Power electronics INVCON 3.3 for off-highway applications*, URL: https://www.bosch-mobility.com/en/solutions/power-electronics/power-electronics-invcon3-3-ohw/, accessed on 19 Sep. 2023.

[91] H. Luke, "The origins of the sampling theorem," *IEEE Communications Magazine*, vol. 37, no. 4, pp. 106–108, Apr. 1999, ISSN: 0163-6804. DOI: 10.1109/35.755459.

[92] J. Grus, *Data science from scratch: first principles with Python*, First edition. Sebastopol, CA: O'Reilly, 2015, OCLC: ocn898161437, ISBN: 978-1-4919-0142-7.

[93] German Institute for Standardisation Registered Association, *DIN 323-1: Preferred Numbers of Series of Preferred Numbers; Basic Values, Calculated Values, Rounded Values*, Aug. 1974.

[94] L. Breiman, "Random forests," *Machine Learning*, vol. 45, pp. 5–32, Oct. 2001. DOI: 10.1023/A:1010933404324.

[95] J. Bergstra, D. Yamins, and D. Cox, "Making a science of model search: Hyperparameter optimization in hundreds of dimensions for vision architectures," in *Proceedings of the 30th International Conference on Machine Learning*, S. Dasgupta and D. McAllester, Eds., ser. Proceedings of machine learning research, vol. 28, Atlanta, Georgia, USA: PMLR, Jun. 2013, pp. 115–123.

[96] F. J. Fahy, "Some applications of the reciprocity principle in experimental vibroacoustics," *Acoustical Physics*, vol. 49, no. 2, pp. 217–229, Mar. 2003, ISSN: 1562-6865. DOI: 10.1134/1.1560385.

Acronyms

AE	Acoustic Emission
AI	Artificial Intelligence
ANN	Artificial Neural Network
BO	Bayesian Optimization
BO-TPE	BO using TPE as surrogate
CAN	Controller Area Network
CWRU	Case Western Reserve University
CWT	Continuous Wavelet Transform
DC	Direct Current
DFT	Discrete Fourier Transform
DL	Deep Learning
DT	Decision Tree
e-machine	electric machine
ENV	Envelope signal (processing method)
FB	Frequency Band (processing method)
FB50_FD	FB processing with 50 frequency bands and FD features
FD	frequency-domain
FD-mean	mean value in frequency-domain
FFT	Fast Fourier Transform
FRF	Frequency Response Function
FT	Fourier Transform
HT	Hilbert Transform

IoT . . . . . Internet of Things

IR . . . . . Inner Race

k-NN . . . . . k-Nearest Neighbors

MEMS . . . . . micro-electromechanical systems

ML . . . . . Machine Learning

OR . . . . . Outer Race

PC . . . . . Personal Computer

PHM . . . . . Prognostics and Health Management

PMSM . . . . . Permanent-Magnet Synchronous Motor

RAW . . . . . Raw signal (processing method)

RF . . . . . Random Forest

RMS . . . . . Root Mean Square

RUL . . . . . Remaining Useful Life

STFT . . . . . Short-Time Fourier Transform

SVM . . . . . Support Vector Machine

TD . . . . . time-domain

TPE . . . . . Tree-structured Parzen Estimator

WT . . . . . Wavelet Transform

Symbols

Symbol	Unit	Description
a	$\mathrm{m/s^2}$	Acceleration in time-domain
A	$\mathrm{m/s^2}$	Acceleration in frequency-domain
a_c	$\mathrm{m/s^2}$	Acceleration from calibration bearing experiment in time-domain
A_c	$\mathrm{m/s^2}$	Acceleration from calibration bearing experiment in frequency-domain
a_h	$\mathrm{m/s^2}$	Hammer-based acceleration response in time-domain
A_h	$\mathrm{m/s^2}$	Hammer-based acceleration response in frequency-domain
b_1	–	Wavelet dilation factor
b_2	s	Wavelet time shifting parameter
c	–	Calibrated acceleration in time-domain
C	–	Calibrated acceleration in frequency-domain
$\mathrm{C_0}$	N	Basic static load rating
D	–	Data set
d_B	m	Ball diameter
d_P	m	Pitch diameter
$\mathcal{D}^\mathrm{A}$	–	Domain A
$\mathcal{D}^s$	–	Source Domain

Symbol	Unit	Description
$\mathcal{D}^t$	–	Target Domain
e	N	Excitation force in time-domain
E	N	Excitation force in frequency-domain
e_h	N	Hammer-based excitation force in time-domain
E_h	N	Hammer-based excitation force in frequency-domain
f	Hz	Frequency
f_0	Hz	Center frequency of Morlet wavelet
$\hat{f}$	–	Estimation function
$\hat{F}$	–	Mapping function
f_i	Hz	Inner ring rotational frequency
F_i	–	Frequency-domain features
f_o	Hz	Outer ring rotational frequency
g	–	Gaussian kernel function
h	$\mathrm{m}/(\mathrm{s}^2 \cdot \mathrm{N})$	Accelerance in time-domain
H	$\mathrm{m}/(\mathrm{s}^2 \cdot \mathrm{N})$	Accelerance in frequency-domain
j	–	Imaginary unit
k	–	Number of neighbors of the k-NN algorithm
L	–	Loss function
M	–	Length of a discrete frequency-domain signal
N	–	Length of a discrete time-domain signal
N_B	–	Number of balls

Symbol	Unit	Description
N_{C}	–	Number of different bearings for classification
N_{D}	–	Number of data samples
N_{FB}	–	Number of frequency bands
N_{S}	–	Number of sensor channels
P	–	Marginal distribution
q_{w}	–	Amplitude correction factor for windowing
r	varies	Time-domain signal
R	varies	Frequency-domain signal
s	varies	Time-domain signal
$\tilde{s}$	varies	Smoothed time-domain signal
S	varies	Frequency-domain signal
S_{ds}	varies	Double-sided spectrum of a signal
s_{H}	varies	Hilbert transformed time-domain signal
t	s	Time
T_i	–	Time-domain features
u	varies	Time-domain signal
U	varies	Frequency-domain signal
v	N	Virtual force in time-domain
V	N	Virtual force in frequency-domain
w	–	Windowing function
W	–	Wavelet transformed signal

Symbol	Unit	Description
x	–	Feature
$\tilde{x}$	–	Standardized feature
$\mathbf{x}$	–	Feature vector
X	–	Feature set
X^s	–	Feature set on source domain
X^t	–	Feature set on target domain
$\mathcal{X}$	–	Feature space
y	–	Label
y_{pred}	–	Predicted label
Y	–	Label set
$\mathcal{Y}$	–	Label space
$\mathcal{Y}^s$	–	Label space on source domain
$\mathcal{Y}^t$	–	Label space on target domain
z	varies	Hilbert analytic signal in time-domain
z_{a}	varies	Hilbert-based instantaneous amplitude in time-domain
Z_{a}	varies	Hilbert-based instantaneous amplitude in frequency-domain
$BPFI$	Hz	Ball pass frequency, inner race
$BPFO$	Hz	Ball pass frequency, outer race
BSF	Hz	Ball (roller) spin frequency
FTF	Hz	Fundamental train (cage) frequency

Symbol	Unit	Description
θ	–	Hyperparameter configuration
$\theta^\star$	–	Optimal hyperparameter configuration
Θ	–	Hyperparameter space
μ	varies	Mean
σ	varies	Standard deviation
τ	s	Temporal delta
ϕ	$^\circ$	Contact angle
ψ	–	Mother wavelet
ψ^*	–	Complex conjugate of the mother wavelet

Supervised Theses

The author supervised the following theses at Bosch Research in Renningen. This dissertation would not have been possible without the support provided by the mentioned students.

- **Feature Engineering zur Zustandsüberwachung von Wälzlagern**
  Feature engineering for condition monitoring of rolling bearings
  Shatri, Etnik (Technical University of Darmstadt, 2022)
  [Master Thesis]

- **NVH-basierte Merkmalskonstruktion für die Zustandsüberwachung von Wälzlagern mittels maschinellen Lernens**
  NVH driven feature engineering for condition monitoring of rolling bearings using machine learning
  Thün, Hannah (RWTH Aachen University, 2022)
  [Master Thesis]

- **Funktionsnachweis eines E-Maschinen-Prüfstands für die Zustandsüberwachung von Wälzlagern**
  Functional verification of an e-machine test rig for condition monitoring of rolling bearings
  Turkan, Eslem (Pforzheim University, 2023)
  [Bachelor Thesis]

Publications

- **Physics-Based Feature Engineering for Predicting the Remaining Useful Life of Ball Bearings**
  Bienefeld, Christoph; Vogt, Andreas; Kacmar, Marian; Kirchner, Eckhard (2021); 62. Tribologie-Fachtagung, Göttingen, Sep. 27-29, 2021; Reibung, Schmierung und Verschleiß, pp. 97-101, ISBN: 978-3-9817451-6-0.
  [Conference Publication]

- **Feature-Engineering für die Zustandsüberwachung von Wälzlagern mittels maschinellen Lernens**
  Bienefeld, Christoph; Vogt, Andreas; Kacmar, Marian; Kirchner, Eckhard (2021); In: Tribologie und Schmierungstechnik, vol. 68, no. 6, pp. 5–11, Dec. 2021, ISSN: 0724-3472. DOI: 10.24053/TuS-2021-0032.
  [Journal Article]

- **Predicting the Electrical Impedance of Rolling Bearings Using Machine Learning Methods**
  Kirchner, Eckhard; Bienefeld, Christoph; Schirra, Tobias; Moltschanov, Alexander (2022);
  In: Machines, vol. 10, no. 2, p. 156, Feb. 2022, ISSN: 2075-1702. DOI: 10.3390/machines10020156.
  [Journal Article]

- **On the Importance of Temporal Information for Remaining Useful Life Prediction of Rolling Bearings Using a Random Forest Regressor**
  Bienefeld, Christoph; Kirchner, Eckhard; Vogt, Andreas; Kacmar, Marian (2022); In: Lubricants, vol. 10, no. 4, p. 67, Apr. 2022, ISSN: 2075-4442. DOI: 10.3390/lubricants10040067.
  [Journal Article]

- **Verfahren zur Bereitstellung von Merkmalen für einen Algorithmus des maschinellen Lernens**
  Bienefeld, Christoph; Kacmar, Marian; Vogt, Andreas (2022);
  Published Patent: Disclosure document of the German Patent and Trade Mark Office (DPMA) dated Oct. 12, 2023;
  Number: DE 10 2022 203 552 A1.
  [Patent]

- **Introducing an Open-Source Simulation Model for Track Rollers Considering Friction**
  Wenzel, Jan; Bienefeld, Christoph; Kretschmer, Alexander; Kirchner, Eckhard (2022);
  In: Applied Mechanics, vol. 3, no. 2, pp. 692–705, Jun. 2022, ISSN: 2673-3161. DOI: 10.3390/applmech3020041.
  [Journal Article]

- **Verfahren und Vorrichtung zur Zustandsermittlung einer zu überwachenden Komponente in einer Maschine mit einem rotierenden Maschinenelement**
  Bienefeld, Christoph; Kacmar, Marian; Vogt, Andreas; Gross, Volker; Elter, Alexander (2022);
  Filed Patent: German patent application filed on Dec. 6, 2022;
  Application number: 10 2022 213 123.1.
  [Patent]

- **Investigation of Feature Engineering Methods for Domain-Knowledge-Assisted Bearing Fault Diagnosis**
  Bienefeld, Christoph; Becker-Dombrowsky, Florian Michael; Shatri, Etnik; Kirchner, Eckhard (2023);
  In: Entropy, vol. 25, no. 9, p. 1278, Aug. 2023, ISSN: 1099-4300. DOI: 10.3390/e25091278.
  [Journal Article]

- **A Hybrid Modeling Approach for Transferring Machine Learning Assisted Condition Monitoring of Rolling Bearings to Differing Machine Types**
  Bienefeld, Christoph (2023);
  77th STLE Annual Meeting & Exhibition, May 21-25, 2023, Long Beach Convention Center, Long Beach, CA, USA, May 21-25, 2023.
  [Conference Publication]

- **Verfahren zur Bereitstellung eines Klassifikators oder Regressors zur Diagnose einer Maschine**
  Bienefeld, Christoph (2023);
  Filed Patent: German patent application filed on Dec. 21, 2023;
  Application number: 10 2023 213 129.3.
  [Patent]